



ACOUSTIC EMISSION AS A TOOL FOR THE IMAGING AND FORECASTING OF DAMAGE EVOLUTION IN ROCK DEFORMATION LABORATORY EXPERIMENTS

PhD Candidate: Thomas King¹

Supervisor: Sergio Vinciguerra¹

Co-Supervisors: Luca De Siena^{2,3} and Phil Benson⁴

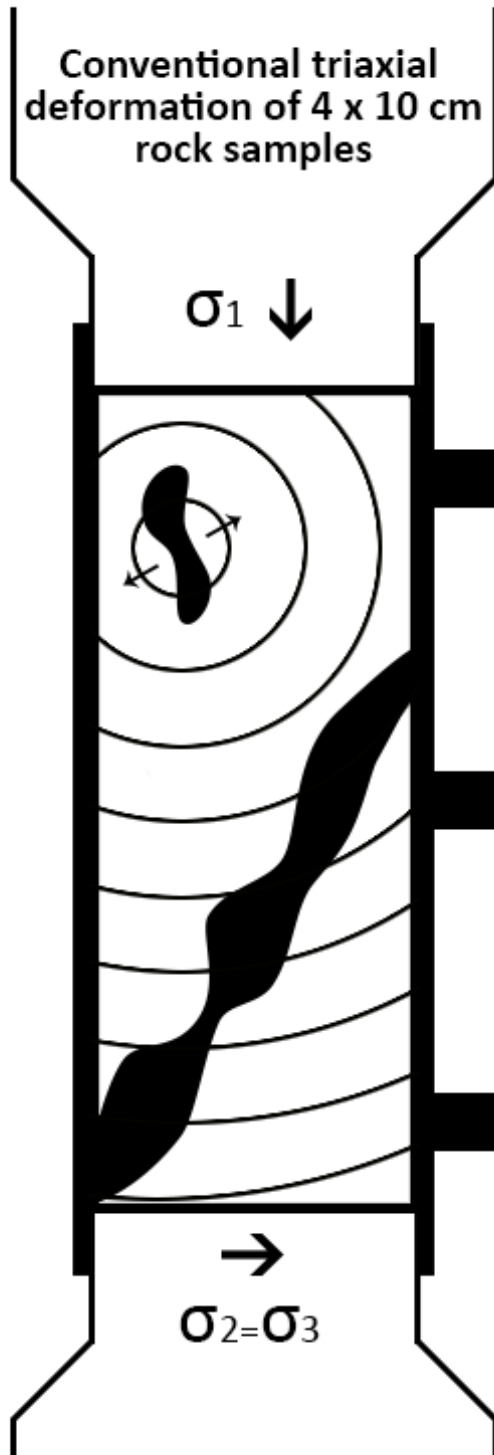
¹ Department of Earth Sciences, University of Turin, Via Tommaso Valperga Caluso, 35, 10125 Turin, Italy;

² Institute of Geosciences, Johannes Gutenberg University, Mainz, Germany;

³ Department of Geology and Petroleum Geology, School of Geosciences, University of Aberdeen, King's College, Aberdeen AB24 3FX, UK;

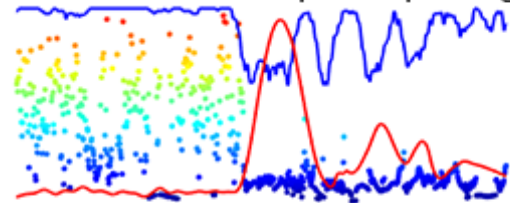
⁴ Rock Mechanics Laboratory, School of Earth and Environmental Sciences, University of Portsmouth, Burnaby Building, Portsmouth PO1 3QL, UK;

GRAPHICAL ABSTRACT



High-resolution analysis of Acoustic Emission waveform characteristics

Machine learned phase picking



Source mechanism classification

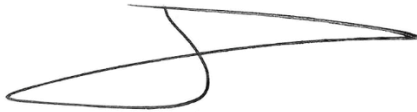


Forward scattering of energy



DECLARATION

Whilst registered as a PhD candidate at the University of Turin, Italy, I have not been registered for any other research award. The results and conclusions presented in this thesis are the work of the named candidate and have not been submitted for any other academic award.

A handwritten signature in black ink, consisting of a large, stylized 'T' followed by a horizontal line that loops back under the 'T' and ends in a small hook.

Thomas King

ACKNOWLEDGMENTS

I think the first person to thank here is Dr. Luca De Siena. Who, at the beginning of my master's project, told me that it probably wouldn't work but we should try anyway. When he forwarded me the call for this PhD, he continued that pessimistic optimism by pushing me to me apply at a time when I couldn't feel any lower. Luca, I will always be grateful for the opportunity that you gave me here, you truly helped me turn my life around.

Through this project I was introduced to its lead supervisor, Dr. Sergio Vinciguerra. An incredibly kind and considerate man, he has sat with me from day 1 of this project helping me to develop my skills and ideas. All the while, sharing my work with others so that future employers already know my name before I know theirs. I was also introduced to the final supervisor of this project, Dr. Philip Benson. His no-nonsense approach to manuscript corrections giving the kind of feedback that encourages me to improve my work.

I must thank the colleagues and friends I met at the Universities of Aberdeen and Portsmouth during my visits to the UK. In particular, David, Ricardo and Peter, you really helped me develop my ideas for the focal mechanism work whilst we were in Potsdam. Special thanks to Marco Fazio and Alexandre Schubnel for reviewing this thesis and for providing thorough feedback on how to improve it. And thankyou to Cesare Comina and Anna Ferrero for being part of the committee during the interview and defence. To the friends I have made whilst in Turin, I cannot give enough thanks. Stephan, Christophe, Antoine and Lukardis, you showed me the Alps and taught me to ski. Something that will forever keep my money low but my spirits high. And to my long-suffering half-wife, Neha, whose path I somehow stumbled into in Turin. Thank you for waiting darling, you are my biggest inspiration in how to be strong.

And finally, to my friends and family in the UK. Who have supported me mentally and financially throughout this long and seemingly endless academic path. One day I will leave school, I can't make any promises though.

This thesis is dedicated to my grandmother, who sadly passed away from a ridiculous disease during my PhD. Were it not for our 'granny days' I would not be where I am today, thank you.

ABSTRACT

Acoustic Emission (AE) refer to the release of energy that occurs due to inelastic deformation of media at the laboratory scale. Analogous to seismic data, they provide a crucial window into the analyses of energy propagation at a scale that is relatively easy to handle. In this thesis, the fracturing processes in the lead up to dynamic failure of rock samples are analysed in terms of the microfracturing source and the effects of a developing fault zone on the propagation of energy.

Two families of rock samples were selected: (1) granites, represented by Alzo Granite and Westerly Granite, and (2) sandstones, represented by Darley Dale Sandstone. The former was selected as a relatively flaw free environment in which to study the nucleation of fractures with minimal biases. Meanwhile the latter, was selected to study these processes in an environment which already had a pre-existing network of damage/porosity. In both cases, the rock types were selected for their generally homogeneous properties, further minimising any influence from bedding or foliation on deformation structure. Samples were deformed under conventional triaxial deformation conditions until dynamic failure under a range of confining pressures. During experimentation, AE were detected by an array of Piezo-Electric Transducers (PZT), recording fracturing events as discrete variations in voltage. It is from this data that the following analyses are derived.

A Distributed Time Delay Neural Network is trained under semi-supervised conditions to recognise the onset of a signal in Acoustic Emission (AE) data obtained during the laboratory deformation experiments. Time series of instantaneous frequency, permutation entropy and seismic envelope are separated into simple classifications of noise and signal. The model is trained in sequential batches, allowing for an automated process that steadily improves as new data are added. To validate the approach, real AE data from a triaxial deformation experiment of Darley Dale Sandstone (fully drained conditions and a confining pressure of 20 MPa) are used to train a model of 300 waveforms that is subsequently applied to pick the onsets of the remaining data. When compared with a simple amplitude-threshold picking methodology, results demonstrate significant improvement in the number and quality of event source locations that may be used in later analyses.

Source mechanism were solved using a least squares minimisation of the 3D first-motion polarity focal sphere to characterise AE as tensile (T-type), shearing (S-type) and compaction/collapsing (C-type). Samples of Alzo Granite and Darley Dale Sandstone were systematically deformed until dynamic failure at confining pressures of 5, 10, 20 and 40 MPa. Periods of fracture nucleation and growth, crack coalescence, and dynamic failure are identified from relative percentages of fracture mechanisms. Spatio-temporal trends further reveal a dependency of fault zone formation on the competition between tensile and compaction type mechanisms, with a surprisingly small amount of shearing. Finally, the occurrence of a family of low amplitude tensile events prior to sample failure point towards predictable and deterministic behaviour in the development of fault zone highlighting the potential for the forecasting of fracture coalescence.

The delay in the maximum amplitude arrival of seismic energy (peak delay) is an important attribute to map complex geology, fluid reservoirs, and faulting in the lithosphere. The parameter was measured and mapped in the frequency range 50 to 800 KHz using Acoustic Emission data recorded during triaxial deformation experiments of Westerly Granite and Darley Dale Sandstone. The highest peak delay consistently appears when energy propagates perpendicular to an acoustic impedance surface such as the deformation-induced shear zone. Measurements confirm the dominance of forward scattering and anisotropy processes, with results that are strongly influenced by the distribution of time-dependent heterogeneity and stiffness.

TABLE OF CONTENTS

DECLARATION	I
ACKNOWLEDGMENTS	II
ABSTRACT	IV
LIST OF FIGURES	IX
LIST OF TABLES	XIV
1 INTRODUCTION.....	1
1.1 ACOUSTIC EMISSION	1
1.2 ROCK DEFORMATION EXPERIMENTS	4
1.3 ‘CLASSICAL’ AE ANALYSIS	12
1.4 ADVANCEMENTS PROVIDED BY THIS THESIS.....	14
2 DATA ACQUISITION AND DEFORMATION RESULTS.....	16
2.1 SAMPLE DESCRIPTIONS.....	16
2.1.1 Alzo Granite	16
2.1.2 Darley Dale Sandstone.....	16
2.1.3 Westerly Granite.....	16
2.2 LABORATORY EQUIPMENT.....	17
2.2.1 Conventional Triaxial Deformation.....	17
2.2.2 Strain Corrections.....	18
2.2.3 Piezo-Electric Transducers	20
2.3 DEFORMATION RESULTS.....	21
2.3.1 Alzo Granite	21
2.3.2 Darley Dale Sandstone.....	22
2.3.3 Westerly Granite.....	25
3 WAVEFORM PICKING AND SOURCE LOCATION.....	26
3.1 INTRODUCTION.....	26
3.1.1 Hilbert-Huang Transform	27
3.1.2 Permutation Entropy.....	27
3.1.3 Time Delay Neural Networks	28
3.2 THEORY AND METHODS	28
3.2.1 Hilbert-Huang Transform	28
3.2.2 Seismic Envelope and Permutation Entropy.....	30

3.2.3	Distributed Time Delay Neural Network	32
3.2.4	Source Location	34
3.3	RESULTS AND DISCUSSION	34
3.3.1	All Parameter Model Validation	34
3.3.2	Single Parameter Model Validation	36
3.3.3	Full-Dataset Validation	39
3.4	CONCLUSIONS.....	41
4	FOCAL MECHANISMS AND SOURCE EFFECTS	43
4.1	INTRODUCTION	43
4.2	METHODOLOGY	44
4.2.1	Mechanism Orientations and Divergence Maps	46
4.3	RESULTS.....	46
4.3.1	Fracture Nucleation and Growth.....	49
4.3.2	Crack Coalescence and Dynamic failure.....	52
4.3.3	Mechanism Orientations.....	Error! Bookmark not defined.
4.4	DISCUSSION.....	59
4.4.1	Cohesive vs. Granular Driven Failure.....	59
4.4.2	Forecasting Dynamic Failure.....	61
4.4.3	Failure Patterns	62
4.5	CONCLUSIONS.....	64
5	PEAK DELAY AND PATH EFFECTS.....	65
5.1	INTRODUCTION	65
5.2	DATA AND METHOD	67
5.2.1	Peak Delay	67
5.2.2	Source Locations and Peak Delay Mapping.....	69
5.2.3	2D Modelling of Anisotropy Variations.....	70
5.3	RESULTS.....	71
5.3.1	Time Dependencies of Peak Delay	71
5.3.2	Hypocentre Dependent Variations	75
5.3.3	Mapping Peak Delay	77
5.3.4	2D Modelling of anisotropy Variations.....	78
5.4	DISCUSSION.....	82
5.5	CONCLUSIONS.....	83

6	CONCLUDING REMARKS	85
7	APPENDIX: MATLAB CODE	87
7.1	WAVEFORM PICKING AND LOCATION.....	87
7.1.1	Train Picking Model.....	87
7.1.2	Generate Velocity Model.....	94
7.1.3	AE Source Location.....	101
7.1.4	Automated Waveform Picking (IFcontent).....	108
7.2	FOCAL MECHANISMS.....	110
7.2.1	Focal Mechanism Solutions.....	110
7.2.2	Mechanism Probability Density Plots	117
7.2.3	Mechanism Inversion.....	122
7.2.4	Mechanism Orientations and Divergence Plots	124
7.3	PEAK DELAY.....	135
7.3.1	Peak Delay Measurement	135
7.3.2	Peak Delay Plotting	138
8	REFERENCES.....	146

LIST OF FIGURES

Figure 1.1: Acoustic emission waveform.....	1
Figure 1.2: Seismic diffusion coefficient tomography from King et al. (2017) highlights a distinct anomaly at Mount St. Helens Volcano, USA.....	2
Figure 1.3: Example of the Kaiser effect occurred in a cyclically loaded concrete. Thick black lines represent the AE activity, thin lines the load and the dashed lines indicate the Kaiser effect (Grosse and Ohtsu, 2008).	3
Figure 1.4: From L’Hermite (1960). Wave velocity and Poisson’s ratio are seen to decrease and increase, respectively, as axial displacement increases.	4
Figure 1.5: Schematic representation of the elements of a conventional triaxial compression testing machine, including option arrangements for pore fluid pressure (Faulkner, 2006). 5	
Figure 1.6: Stress ellipsoid describes the state of stress at a point in a rock (Pramoda Raj, N.D).....	7
Figure 1.7: Non-linear dependence of differential stress at failure in compression on confining pressure for granite from Byerlee (1967).	8
Figure 1.8: Typical stress-strain curve from deformation experiments with major stress thresholds indicated.....	11
Figure 1.9: a) Damage quantification with a combination of Calm and Load ratio. b) Crack type classification with a combination of average frequency and RA values. From Grosse and Ohtsu (2008).....	14
Figure 2.1: Triaxial deformation cell (left) and schematic (right). The sample is positioned inside a rubber jacket located in the centre of the apparatus (brown). AE are recorded by an array of PZT sensors (black squares) positioned along the walls of the jacket. Axial stress and confining pressure are controlled by pore fluid pumps.	17
Figure 2.2: Stress-strain curve for theoretical (black) and measured (grey) values of an aluminium-alloy cylinder from Fazio (2017).	18
Figure 2.3: Piezo-Electric Transducers (diamonds) are evenly distributed around the sample.....	20
Figure 2.4: Acoustic Emission counts (black bars, 0.01% strain bins) and stress-strain curves (black line) for Alzo Granite.....	21
Figure 2.5: Post-experimentation imaging of Alzo Granite. Shear zone structure is highlighted in red.	22
Figure 2.6: Acoustic Emission counts (black bars, 0.01% strain bins) and stress-strain curves (black line) for Darley Dale Sandstone.	23
Figure 2.7: Post-experimentation imaging of Darley Dale Sandstone. Shear zone structure is highlighted in red.....	23
Figure 2.8: Acoustic Emission counts (black bars, 0.01% strain bins) and stress-strain curves (black line) for Darley Dale Sandstone (left) and Westerly Granite (right).....	24
Figure 2.9: Selected CT images of the samples used in chapter 5. Deformation structure within the Darley Dale Sandstone sample is revealed to be relatively simple, whilst Westerly granite highlights diffuse and complex fracture structure.....	24

Figure 3.1: Dominant frequency content of the AE waveform. Red and blue indicates high and low frequency content respectively. Pre-signal noise is characterised by high frequency and the signal itself with low values.	30
Figure 3.2: Example Root Mean Square envelope (red) and calculated entropy series (blue). Pre-signal noise is characterised by low seismic envelope values and high values of entropy and vice-versa for the signal.	31
Figure 3.3: Model Output (red) provides a simpler time series from which to automatically identify the signal onset (blue). Portions of the waveform confidently classified as signal are represented by a 1, whilst pre-signal noise is classified as -1.	33
Figure 3.4: a) A model is sequentially trained in batches of 10 waveforms and then validated with the remaining data. Dark lines indicate the average value of performance indices and the lighter region indicates the 95% confidence interval. b) Here the model is validated on its own training data after each batch of 10 waveforms.	35
Figure 3.5: Amplitude distribution of data used in training the neural network model (left) and associated picking errors (black circles) with 95% confidence interval plotted as error bars (right).	36
Figure 3.6: Validation of model trained only on instantaneous frequency content. Dark lines indicate the average value of performance indices and the lighter region indicates the 95% confidence interval.	37
Figure 3.7: Validation of model trained only on seismic envelope. Dark lines indicate the average value of performance indices and the lighter region indicates the 95% confidence interval.	37
Figure 3.8: Validation of model trained only on entropy. Dark lines indicate the average value of performance indices and the lighter region indicates the 95% confidence interval.	38
Figure 3.9: Associated picking errors in amplitude windows for the single parameter analysis.	38
Figure 3.10: Example AE with their recorded waveforms picked (red dots). Note in the second AE (right) the picking of a P-wave arrival for the bottom two waveforms.	40
Figure 3.11: Source locations plotted as density plots. Data are plotted in 1200 event bins. a) Data picked with a threshold method. b) Data picked with the Neural Network results in a higher density of source locations and cleared fault zone structure.	40
Figure 3.12: Picking errors are compared for both methodologies. The threshold method has very high location residual errors compared to the neural network for low signal to noise ratios.	41
Figure 4.1: a) Absolute polarity of idealised focal mechanisms of C-type (left), S-type (middle) and T-type (right) fracturing. b) Deviatoric amplitude distribution of the same mechanisms.	44
Figure 4.2: a) Post-failure imagery and fault plane in red (top left) for Alzo Granite at 5 MPa. Focal mechanism probabilities (top right) show T-type (yellow), S-type (green) and C-type (blue) events separated by amplitude (lighter for high, darker for low) as strain increases. Fracture mechanism plane distributions (bottom) show the spatial distribution and orientations of events. b) Divergence maps of mechanism slip vectors. Red regions indicate dilatational regions where vector directions are diverging. Blue indicates	

compactant regions where vector directions are converging. Data are windowed into phases of 1) Fracture Nucleation and Growth, 2) Crack Coalescence and 3) Dynamic Failure. ...47

Figure 4.3: a) Post-failure imagery and fault plane in red (top left) for Alzo Granite at 10 MPa. Focal mechanism probabilities (top right) show T-type (yellow), S-type (green) and C-type (blue) events separated by amplitude (lighter for high, darker for low) as strain increases. Fracture mechanism plane distributions (bottom) show the spatial distribution and orientations of events. b) Divergence maps of mechanism slip vectors. Red regions indicate dilatational regions where vector directions are diverging. Blue indicates compactant regions where vector directions are converging. Data are windowed into phases of 1) Fracture Nucleation and Growth, 2) Crack Coalescence and 3) Dynamic Failure. ...48

Figure 4.4: a) Post-failure imagery and fault plane in red (top left) for Alzo Granite at 20 MPa. Focal mechanism probabilities (top right) show T-type (yellow), S-type (green) and C-type (blue) events separated by amplitude (lighter for high, darker for low) as strain increases. Fracture mechanism plane distributions (bottom) show the spatial distribution and orientations of events. b) Divergence maps of mechanism slip vectors. Red regions indicate dilatational regions where vector directions are diverging. Blue indicates compactant regions where vector directions are converging. Data are windowed into phases of 1) Fracture Nucleation and Growth, 2) Crack Coalescence and 3) Dynamic Failure. ...50

Figure 4.5: a) Post-failure imagery and fault plane in red (top left) for Alzo Granite at 40 MPa. Focal mechanism probabilities (top right) show T-type (yellow), S-type (green) and C-type (blue) events separated by amplitude (lighter for high, darker for low) as strain increases. Fracture mechanism plane distributions (bottom) show the spatial distribution and orientations of events. b) Divergence maps of mechanism slip vectors. Red regions indicate dilatational regions where vector directions are diverging. Blue indicates compactant regions where vector directions are converging. Data are windowed into phases of 1) Fracture Nucleation and Growth, 2) Crack Coalescence and 3) Dynamic Failure. ...51

Figure 4.6: The strain difference between $\varepsilon_{critical}$ and ultimate compressive strength follows a log-linear relationship with confining pressure.52

Figure 4.7: a) Post-failure imagery and fault plane in red (top left) for Darley Dale Sandstone at 5 MPa. Focal mechanism probabilities (top right) show T-type (yellow), S-type (green) and C-type (blue) events separated by amplitude (lighter for high, darker for low) as strain increases. Fracture mechanism plane distributions (bottom) show the spatial distribution and orientations of events. b) Divergence maps of mechanism slip vectors. Red regions indicate dilatational regions where vector directions are diverging. Blue indicates compactant regions where vector directions are converging. Data are windowed into phases of 1) Fracture Nucleation and Growth, 2) Crack Coalescence and 3) Dynamic Failure. ...53

Figure 4.8: a) Post-failure imagery and fault plane in red (top left) for Darley Dale Sandstone at 10 MPa. Focal mechanism probabilities (top right) show T-type (yellow), S-type (green) and C-type (blue) events separated by amplitude (lighter for high, darker for low) as strain increases. Fracture mechanism plane distributions (bottom) show the spatial distribution and orientations of events. b) Divergence maps of mechanism slip vectors. Red regions indicate dilatational regions where vector directions are diverging. Blue indicates compactant regions where vector directions are converging. Data are windowed into phases of 1) Fracture Nucleation and Growth, 2) Crack Coalescence and 3) Dynamic Failure. ...54

Figure 4.10: a) Post-failure imagery and fault plane in red (top left) for Darley Dale Sandstone at 20 MPa. Focal mechanism probabilities (top right) show T-type (yellow), S-type (green) and C-type (blue) events separated by amplitude (lighter for high, darker for

low) as strain increases. Fracture mechanism plane distributions (bottom) show the spatial distribution and orientations of events. b) Divergence maps of mechanism slip vectors. Red regions indicate dilatational regions where vector directions are diverging. Blue indicates compactant regions where vector directions are converging. Data are windowed into phases of 1) Fracture Nucleation and Growth, 2) Crack Coalescence and 3) Dynamic Failure... 56

Figure 4.11: a) Post-failure imagery and fault plane in red (top left) for Darley Dale Sandstone at 40 MPa. Focal mechanism probabilities (top right) show T-type (yellow), S-type (green) and C-type (blue) events separated by amplitude (lighter for high, darker for low) as strain increases. Fracture mechanism plane distributions (bottom) show the spatial distribution and orientations of events. b) Divergence maps of mechanism slip vectors. Red regions indicate dilatational regions where vector directions are diverging. Blue indicates compactant regions where vector directions are converging. Data are windowed into phases of 1) Fracture Nucleation and Growth, 2) Crack Coalescence and 3) Dynamic Failure... 57

Figure 4.9: Average mechanism orientations are plotted against confining pressure for events dipping parallel or perpendicular to the sample failure plane. Error bars are defined as the standard error and represent the range of data from which the average is calculated. 59

Figure 4.12: Simplified brittle failure patterns. Dilatant regions (black) highlight the changing distribution of deformation structure as confining pressure increases for the different deformation stages. A transitionary phase between axial splitting is identified where zones of deformation form into planar structure during crack coalescence. 63

Figure 5.1: Peak Delay is defined as the time between the onset of energy and the maximum energy arrival. The raw AE waveform (above) is filtered within a specified frequency bands and the maximum is identified from the RMS envelope calculated. As there is significant overlap of energy (e.g. direct, transmitted and reflected arrivals), the maximum is selected between the onset, T, and $3 \cdot T$. The range of time for the signal to be above 90% of the signal maximum is defined as the error (red line). 68

Figure 5.2: Source locations (black dots), PZT receivers (diamonds) and grey lines (raypaths) used in the Peak Delay tomography analysis. 69

Figure 5.3: Source and receiver array (both represented as diamonds) used in the numerical modelling. Grey lines indicate raypaths. 70

Figure 5.4: Average values of Peak Delay are plotted with their standard error (shaded region) in a moving window of 1500 measurements for each of the analysed frequency bands. Comparison with differential stress highlights a marked increase in the average delay following dynamic failure of the samples. 72

Figure 5.5: Selected waveforms from the sandstone highlight the changing frequency content for before and after sample failure. As with Figure 5.4, a marked increase in Peak Delay values occur following shear zone coalescence. This trend does not occur at 600 KHz where Peak Delay remains relatively constant. 73

Figure 5.6: Peak amplitude to pre-signal noise ratios are calculated for each Peak Delay measurement to investigate differences in waveform attenuation for before and after failure. Although the effect is minor, attenuation does play a role where counts of low and high amplitude ratios increase and decrease respectively. 74

Figure 5.7: $\log(t_p)$ is compared with hypocentral distance R. The black line indicates the regression fit proposed by Takahashi, et al. (2007), however, as the data spread is very high at the higher frequencies and the dependency on R is low, this study calculates the deviation

- around the average value. A family of anomalously high measurements further suggest the presence of resonant scattering in the data.76
- Figure 5.8: Simplified CT image of internal fracture network (left) and spatial distribution of $\Delta \log t_p$ values. Logarithmic Peak Delay variations are shown in the lower colour bar while diamonds show the PZT positions. Only regions crossed by a minimum of 5 rays are displayed. Azimuthal coverage of model blocks (and so confidence) is reduced towards the edges and outside the region delineated by the receivers. Diamonds indicate receivers used in mapping. The bounding boxes indicate the dimensions of the sample.77
- Figure 5.9: Synthetic circular pore Peak Delay modelling. To simulate coalescence conditions, pore structure becomes increasingly sparse. Modelling identifies clear structure dependent amplitude variations of $\Delta \log t_p$. Sparsely distributed structure more strongly influences lower frequencies with a high Peak Delay anomaly shifting to higher frequencies as coalescence increases. Once fully formed, the circular pore demonstrates very high Peak Delay anomalies for all frequency bands.79
- Figure 5.10: Synthetic fracture width Peak Delay modelling. To simulate the effects of fracture width, the aspect ratio of an equant pore is increased in steps of 0.1. When the aspect ratio is beyond 0.5 (left-hand side) the Peak Delay anomaly remains largely unchanged. Near-field radiation is present along the medium edges, particularly at 100-200KHz, although the effect is limited to within a few mm. Peak Delay anomalies begin to significantly vary when the aspect ratio is below 0.5 (right-hand side). As with Figure 5.9 these variations are attributed to interference between direct and transmitted waves.80
- Figure 5.11: Synthetic waveforms reveal the occurrence of two separate wave fronts in the form of direct and transmitted arrivals. These occur when energy propagates along the length of a narrow inclusion.81
- Figure 5.12: a) Angle of Incidence θ_i vs. Peak Delay for synthetic narrow fracture modelling. Below 30° and above 60° Peak Delays are reflective of the travel time through the fracture medium (solid line). Anomalously low values (dashed line) are present between 30° and 60° when energy that travels around the fracture arrives just before the transmitted wave. b) This strongly affects tomography results where the Peak Delay anomaly is observed to rapidly invert as frequency increases. As it is difficult to separate the direct from the transmitted wave at these small hypocentral distances, it is suggested that this behaviour be used as an indicator for narrow or sparse structure.81

LIST OF TABLES

Table 3.1: The ordinal patterns of order $d = 2$ from Unakafova and Keller (2013).....	31
Table 4.1: Counts of mechanism orientations.....	58

1 INTRODUCTION

1.1 ACOUSTIC EMISSION

When a medium undergoes a sudden redistribution of stress, typically due to external forces, energy is released in the form of transient elastic waves (**Figure 1.1**). Within the dynamic processes of the earth, this release of energy is recorded as earthquakes and provides a wealth of information on the mechanisms of the source. Furthermore, and possibly more importantly, the nature of the medium between the origin and the recording device is revealed as the waveform becomes increasingly modified as it propagates. The difficulty lies in separating out the effects of the source and interpreting each subtle modification formed along the propagation path. Thus, providing the focus of this thesis.

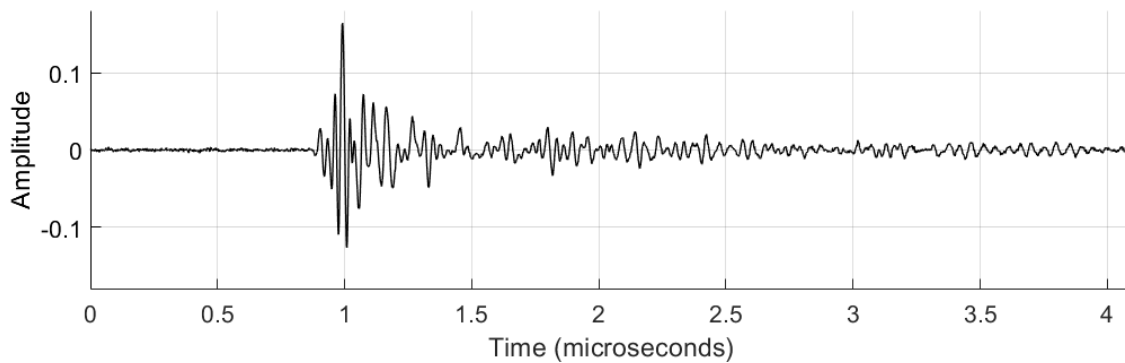


Figure 1.1: Acoustic emission waveform.

As an interdisciplinary science, Seismology, the study of transient elastic waves, is not new. Much of the theory required to interpret seismic records was provided prior to 1922 (Ben-Menahem and Gibson, 1995). Through the efforts of mathematicians and physicists of the last 400 years, many achievements were made in continuum mechanics, applied mathematics and general wave theory. Although, it was not until the 1880s, with the advent of the teleseismic seismogram, did seismology become a globally recognised science. With every major earthquake new milestones in the documentation of surface faulting (Mikumo and Ando, 1976), the observation of a P,S, and R waves (Oldham, 1899), Reid's elastic rebound theory (Reid, 1910), earthquake engineering (Green and Watson, 1989) and the experimental verification of the propagating rupture of faults (Kanamori and Cipar, 1974) has since allowed the science to flourish. With the introduction of digital computation in the 1950s, the ability to perform the required calculations increased tenfold.

Suddenly, huge amounts of data could be processed easily, allowing for the rapid and efficient evaluation of tectonically active regions (e.g. **Figure 1.2**).

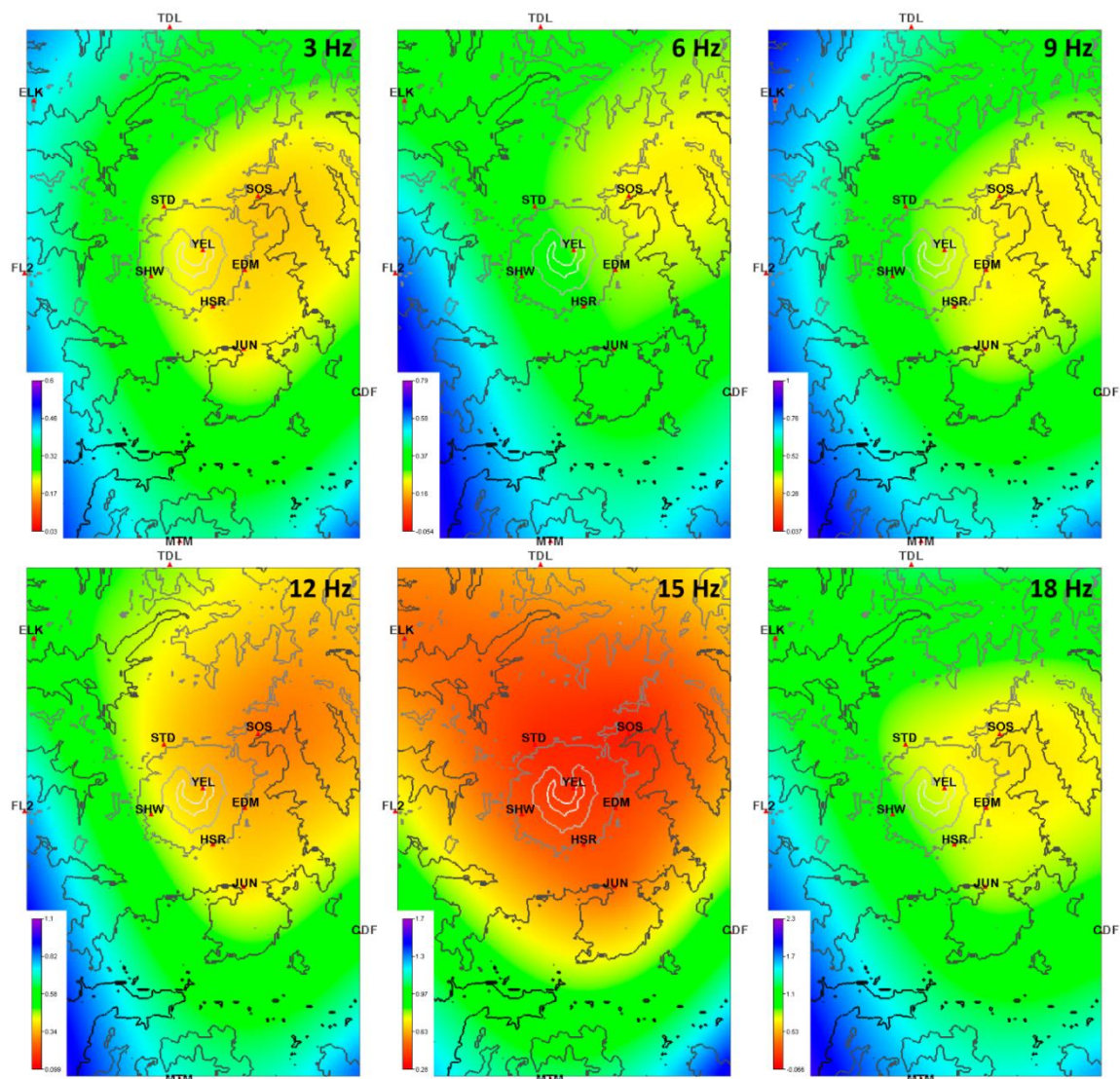


Figure 1.2: Seismic diffusion coefficient tomography from King et al. (2017) highlights a distinct anomaly at Mount St. Helens Volcano, USA.

In the late 20th century (although recorded as early as 6,500 BC!, Grosse and Ohtsu, 2008) scientists began to investigate the release of energy in materials such as tin and zinc, as well as various alloys; Czochralski (1916) noted a relationship between tin and zinc cry and twinning, whilst French scientists (Portevin and Le Chatelier, 1923) later identified the release of energy in stressed Aluminium-Copper-Manganese alloy. Over the next 20 years, scientists such as Robert Anderson, Erich Scheil and Friedrich Forster provided further verification of these observations (Anderson and Baird, 1924; Förster and Scheil, 1936). Finally culminating in the subject defining PhD thesis of Joseph Kaiser in 1950 (Kaiser,

1950), the relationship between applied stress and the release of energy was established, bringing with it the birth of modern-day Acoustic Emission testing in 1958 (Schofield et al., 1958).

Acoustic Emissions (AE) drew a great deal of attention for their ability to passively record the presence of damage without the need of invasive and destructive methodologies. Although this could be considered counter intuitive as the formation of damage is necessary for testing, signals are recorded passively during loading, therefore monitoring the evolution of a defect as it forms without the need to disturb the specimen. The advantage of this is that AE can be used to detect fracturing at a very early stage, long before the sample fails. Beginning in the 1960s, studies on noise produced when compressive load was applied to concrete (e.g. Ruesch, 1959) observed the Kaiser effect (e.g. **Figure 1.3**) to approximately 75% of failure load, further noting that the generation of AE was closely related to volumetric change and the absorption of ultrasonic waves. A reduction in ultrasonic velocity and an increase in Poisson's ratio are further summarised in **Figure 1.4** by L'Hermite (1960). By the 1970s it was demonstrated that AE waveforms are highly sensitive to variations in deformation structure, particularly P-wave and S-wave elastic velocity and velocity anisotropy as the density of fractures increases (Bonner, 1974; Hadley, 1976; Lockner et al., 1977; Nur, 1971).

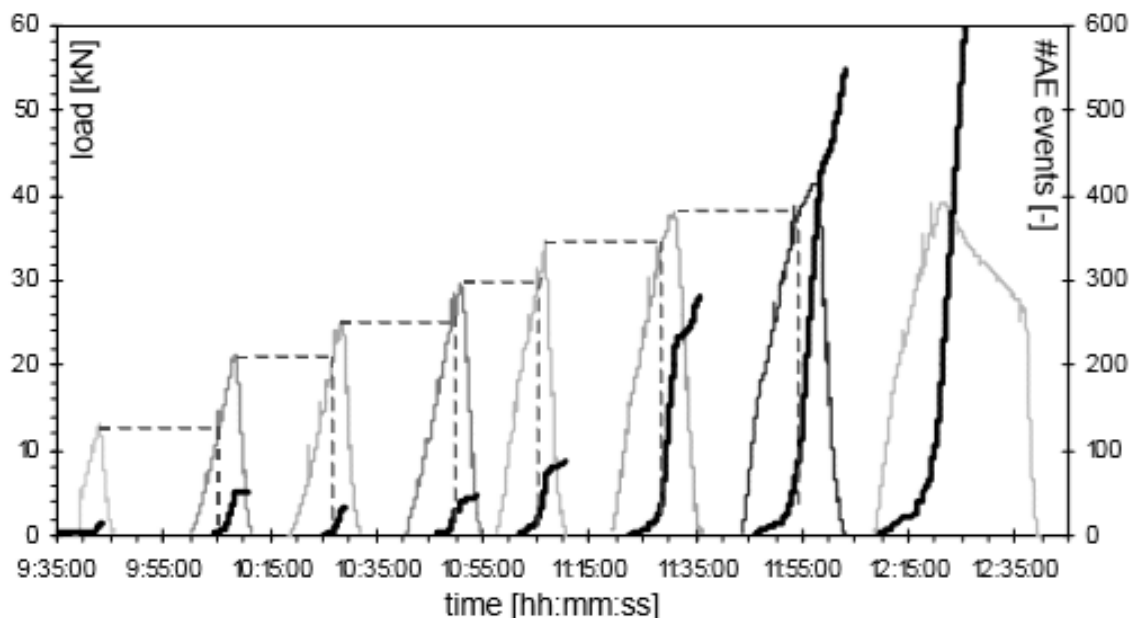


Figure 1.3: Example of the Kaiser effect occurred in a cyclically loaded concrete. Thick black lines represent the AE activity, thin lines the load and the dashed lines indicate the Kaiser effect (Grosse and Ohtsu, 2008).

From the 1980s AE methodologies began to be applied to a wide range of engineering industries (Scruby and Wadley, 1983; Spanner, 1981). During hydrostatic proof tests of pressure vessels, AE were used as an ‘add on’ technique for monitoring purposes. Both the nuclear and petrochemical industries found use in the ability of AE to detect and locate incipient defects in pressurised components (Sadri and Ying, 2019). As the field developed, additional problems brought on by background or environmental noises were eliminated as instrumentation and measuring systems improved. Owing to these advances, modern commercial systems now record elastic waves produced by the release of stored strain energy as cracks nucleate and propagate. These are then detected at the surface of the medium by AE sensors that convert the displacement caused by elastic energy into electrical signals. Although fully digitised, the sensors are effectively an analogue system. As a result, AE consist of a P-wave (longitudinal or volumetric waves), an S-wave (transverse or shear waves), surface waves (Rayleigh wave and Love waves), diffracted waves and guided waves (e.g. Lamb waves). Due to limitations in the acquisition setup, additional waves are induced by resonance of the sensors. Therefore, much like field-scale earthquake data, AE waveforms are the result of the source, heterogeneity along the propagation path and the detection system used in acquisition.

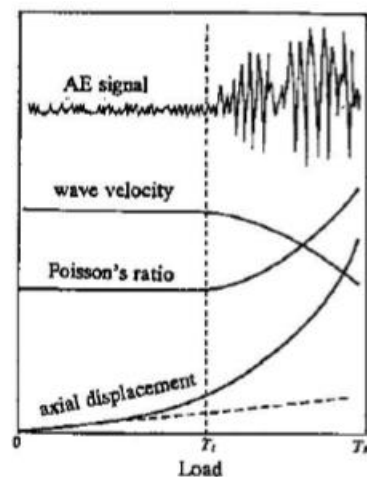


Figure 1.4: From L’Hermite (1960). Wave velocity and Poisson’s ratio are seen to decrease and increase, respectively, as axial displacement increases.

1.2 ROCK DEFORMATION EXPERIMENTS

Developed concurrently but independently, triaxial deformation apparatus sought to investigate the mechanical properties of various media whilst under different pressure, saturation and temperature conditions. Originally pioneered by Von Kármán (1911), the

essential elements are detailed in **Figure 1.5**. A cylindrical sample is surrounded by a fluid, commonly oil in present applications (Gehne, 2018), which is raised to a high pressure to provide *confining pressure*. A rubber jacket acts to separate the sample from the oil. A piston is then used to apply *axial pressure* along the length of the specimen. Some arrangements optionally include *pore-fluid pressure* for more complex analyses.

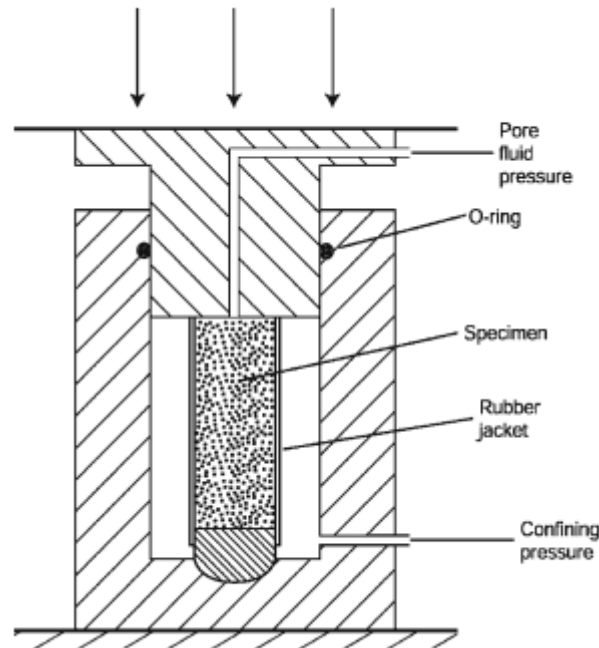


Figure 1.5: Schematic representation of the elements of a conventional triaxial compression testing machine, including option arrangements for pore fluid pressure (Faulkner, 2006).

Building on this design, Griggs (1936) later introduced an additional piston so as to induce identical movements from both ends of the sample, although it should be noted that only one piston was used to apply force. The second acted to compensate the other by maintaining constant volume between the two pistons and avoiding change in confining pressure due to piston movement. Furthermore, it greatly reduced the net axial force needed from the external loading device at high confining pressures by providing a counter balance. An alternative setup connects the confining fluid to the annular area of a stepped single piston to achieve the same effect (Murrell and Ismail, 1976; Paterson, 1990; Tullis and Tullis, 1986).

In the Earth Sciences, the brittle behaviour of different rock types is of interest for use in understanding faulting and the mechanics of earthquakes. During rock mechanics testing, samples are typically deformed at confining pressures in the range of 1 to 200 MPa, although some apparatuses go as high as 2200 MPa when testing metals (Schock et al.,

1973). Structural features such as fractures and pore space play a fundamental role in determining the bulk strength of the rock mass (Bubeck et al., 2017). When pressure is applied, these features often form nucleation sites and encourage the propagation of damage, eventually leading to sample failure (Sibson, 1985). Although the effects of scale play an important role in brittle behaviour, the environment under which force is applied, such as saturation or temperature conditions, will modify how damage develops (Benson et al., 2007).

Conventionally there are two principal modes of brittle fracture: extension fracture where there is a separation of bonds normal to the failure surface and shear fracture when this separation has an associated displacement (Griggs and Handin, 1960). In either case, the brittle fracture of a rock is a discrete event that occurs when stress exceeds a threshold that is determined by the local environmental conditions. In triaxial compression tests, shear fracture is the dominant mechanism of failure and generally occurs between 20 and 30 degrees to the maximum principal stress (e.g. Paterson, 1958). Whilst better known in uniaxial tension tests, the extension fracture occurs normal to the direction of minimum stress. However, they can also occur under compressive conditions in the form of axial splitting parallel to the compression axis, due to local tensile stresses around pre-existing defects at a microscopic scale (Scholz et al., 1986), although this is strongly dependent on the strength of confining pressure (e.g. Griggs, 1936).

Due to the complex interaction between the different stresses, that is further influenced by the mode of fracturing and environmental conditions, there is no simple universal law that governs when a given rock will fail (Mehranpour and Kulatilake, 2016). The conditions for when failure will occur is generally represented as:

$$\sigma_1 = f(\sigma_2, \sigma_3), \quad (1.1)$$

where σ_1 , σ_2 and σ_3 represent the three principal stresses acting upon the medium (**Figure 1.6**). Known as the criterion of failure, the function f often takes many forms which are characteristic of the media under study. Broadly speaking, the compressive stresses required for failure are centred on the uniaxial strength of a sample and the confining pressure (Colmenares and Zoback, 2002). At room temperature, these conditions can be loosely summarised as (Faulkner, 2006):

1. **Igneous and high-grade metamorphic rocks:** At a confining pressure of 100 MPa, compressive strengths are typically in the range of 100-200 MPa, although sometimes higher for fine-grained rocks. At the point of failure, differential stresses ($\sigma_1 - \sigma_3$) are often around 500-800 MPa, which increases to 1000-2000 MPa at very high confining pressures (e.g. 200 MPa).
2. **Low-porosity sedimentary and low-to-medium grade metamorphic rocks (i.e. calcite limestones and marbles):** Uniaxial compressive strengths are typically between 50 and 100 MPa, with failure occurring at a differential stress of 200-300 MPa at a confining pressure of 100 MPa.
3. **High-porosity and some low-grade metamorphic rocks:** Relatively very weak with uniaxial compressive strengths of 10-50 MPa.
4. **Low-porosity dolomites and quartzites:** Some of the strongest rocks that are studied, compressive strengths can exceed 300 MPa at 100 MPa confining pressure.

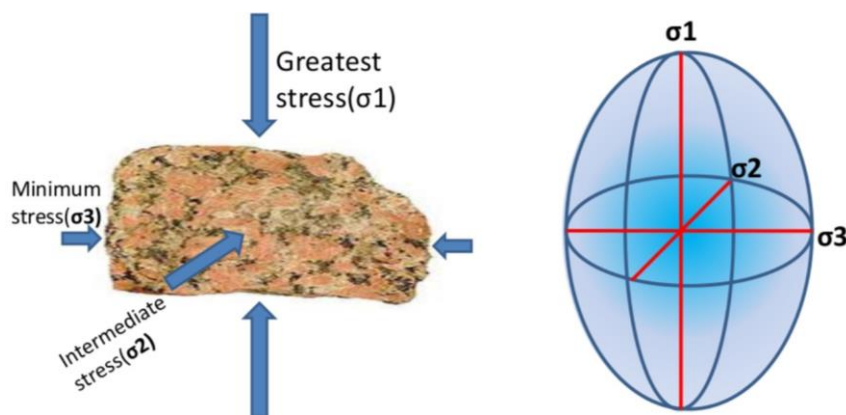


Figure 1.6: Stress ellipsoid describes the state of stress at a point in a rock (Pramoda Raj, N.D).

The role of pore fluid in fracture development is important for its ability to hold open asperities and reduce friction (Beeler et al., 2000). Moreover, fluid chemistry and suspended particles also present further complexities. Water, for example, acts to reduce the strength of rocks through stress corrosion (Amitrano and Helmstetter, 2006; Benson et al., 2010). As the majority of rocks are porous to some degree, under natural conditions they are likely to contain a fluid phase. The pore structure itself is often distinguished as a bimodal distribution: pores which are of equant shape and cracks which are non-equant (Walsh and Brace, 1966). When occurring together, it is termed as double-porosity (Berryman and Wang, 1995). The connectivity of these structures, as well as a third class known as channels, is of utmost importance as they control permeability and the flow of fluids through the rock mass. During triaxial deformation tests the force created by pore-

fluid pressure acting against axial and compressive stresses has brought about the notion of effective stress theory (Terzaghi, 1936). Defined as the total macroscopic stress minus the pore pressure (Skempton, 1961), effective stress is a general approach to describe the gross mechanical behaviour of a porous solid under saturated conditions.

Some additional factors that play a role in the strength of a rock are mineral composition (He et al., 2019), alteration due to burial or weathering effects (Crisci, 2019), prior deformation/temperature history (Liu et al., 2020) and the speed at which a sample is deformed (Cen et al., 2020).

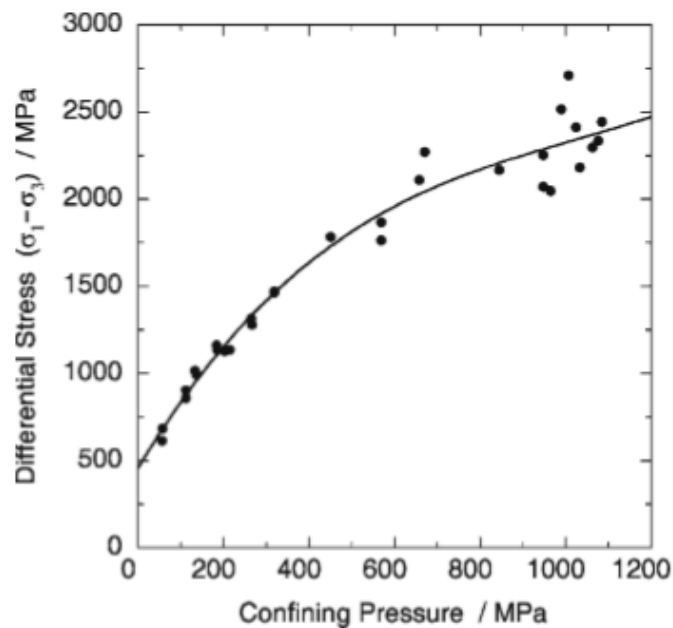


Figure 1.7: Non-linear dependence of differential stress at failure in compression on confining pressure for granite from Byerlee (1967).

However, first and foremost it is predominantly confining pressure that plays the largest role in determining when a rock will fail under compressive conditions. The most commonly accepted relationship is known as the Mohr-Coulomb criterion (Hackston and Rutter, 2016; Mohr, 1900). Here, only the principal stresses are considered. It is frequently observed that the maximum differential stress prior to brittle failure depends markedly on the confining pressure. It is represented by the following linear equation:

$$|\tau| = \tau_0 + \sigma \tan \varphi, \quad (1.2)$$

where τ and σ represent the maximum shear stress and the normal stress acting upon a plane inclined at an angle $\theta = \pi/4 \pm \varphi/2$ to the specimen axis. There are many situations where

this relationship is non-linear (**Figure 1.7**). However, due to the mathematical simplicity of the Coulomb relation, it is often valid and in other cases where it is less so, it can be used as a first approximation.

Until this point, the focus of research has been on developing empirical models that attempt to identify criteria of failure that are consistent with the observed failure conditions under a particular set of conditions (Mehranpour and Kulatilake, 2016). Although these criteria may be summarised as physical conditions, i.e. strain percent, they say very little about the mechanisms of failure. Although a degree of empiricism is still involved, the *Griffith theory* of brittle fracture instead attempts to create a model that represents the actual physical mechanisms behind the propagation of damage. Originally proposed in 1920 (Griffith, 1920), the theory states that the tensile strength of brittle materials is governed by the initial presence of small cracks. Here, the criterion of failure is based on the principle that the potential energy of a system will tend towards a minimum. In a population of randomly orientated cracks, only those that are the most vulnerably orientated towards the direction of stress will extend and thus facilitate the reduction of potential energy. In doing so, the sum of the following three terms will therefore be zero or negative:

1. The surface energy of the new crack surface created
2. The change in the elastic strain energy of the body
3. The change in the potential energy of the loading system

In the absence of any other changes, this is sometimes referred to as the thermodynamic criterion of failure (Murrell, 1964; Murrell and Digby, 1972).

Nevertheless, this approach is not without its own weaknesses. Initial assumptions regarding the shape of the open crack (ellipsoidal) and the existence of infinite values of stress at the crack tip has led to several modifications of the theory (Rice, 1972). Difficulties further arise when considering compressive conditions and the closure of fractures. As confining pressure increases, it is likely many fractures will close and introduce frictional effects (van der Baan et al., 2016). Indeed, studies have shown a reduction in the attenuation of sound waves (Birch and Bancroft, 1938) and an increase in seismic velocity (Birch, 1961, 1960) as pressure increases, suggesting the closure of open structure. This led to the creation of the *modified Griffith theory* (McClintock and Walsh, 1962). In both biaxial and triaxial stress conditions, cracks are now assumed to close when the macroscopic normal

stress perpendicular to the fracture is under a certain value of confining pressure. The initiation of tensile failure is governed by the modified criterion:

$$\tau = \frac{\alpha'}{2} T_0 \sqrt{1 + \frac{\sigma_c}{T_0} + \mu(\sigma_n - \sigma_c)}. \quad (1.3)$$

As with the Coulomb criterion, σ_1 and σ_3 are the principal maximum and minimum stresses. In addition, there are a frictional coefficient μ , confining pressure σ_c and an α term which considers the elastic properties and the axial ratios of the fracture. Further extensions to this theory also consider the initiation of shear and compressive modes of failure (e.g. Ramsey and Chester, 2004).

Although the Griffith theory and its modifications represent a first step towards physically realistic models of fracture propagation, it is still unable to predict accurate values of the strength of the rock. Several authors have suggested that as the strength observation refers to the final macroscopic failure and the Griffith theories only focus on the initiation of damage, they should be considered as separate processes (Bieniawski, 1968; Brace, 1960; Brace and Bombolakis, 1963; Hoek and Bieniawski, 1965). It is therefore essential to consider the evolution of deformation structure through time as a series of discrete fracturing processes that are dependent on the prior state rather than only considering the initial conditions of the rock.

During rock deformation experiments, inelastic damage (fracturing) represents the bulk density change of a sample and therefore reflects changes in the microstructure of the rock. As previously discussed, this is then highlighted as changes in seismic velocity, attenuation parameters and the mechanical measurements taken during testing. Mechanical data are typically represented as the individual stress measurements and relative deformation, recorded as strain percent. **Figure 1.8** is a common output. The stress-strain curve demonstrates the behaviour of a material as it passes through various stages when it is subjected to load, i.e. tensile or compressive.

The Elastic Limit is the maximum value of stress up to which the material is perfectly elastic. Prior to this point, the material will return to its original position. Ultimate stress is the maximum strength of a material prior to Dynamic Failure, corresponding to the peak point of the stress-strain curve. Post-failure phases of Dynamic Failure and Shearing typically involve the development of the shear zone. Several stress thresholds have been

further identified and are used to characterise the evolution of cracking or damage. The crack closure threshold, σ_{CT} , refers to the point when all pre-existing microcracks have closed due to compression of the sample. After closure, a material will behave elastically until the onset of fracturing at crack initiation, σ_{CI} . The deformation during this phase is considered to be stable as it requires an increase in load to induce further damage. The point at which damage propagation becomes unstable is known as the crack damage threshold, σ_{CD} (Bieniawski, 1967).

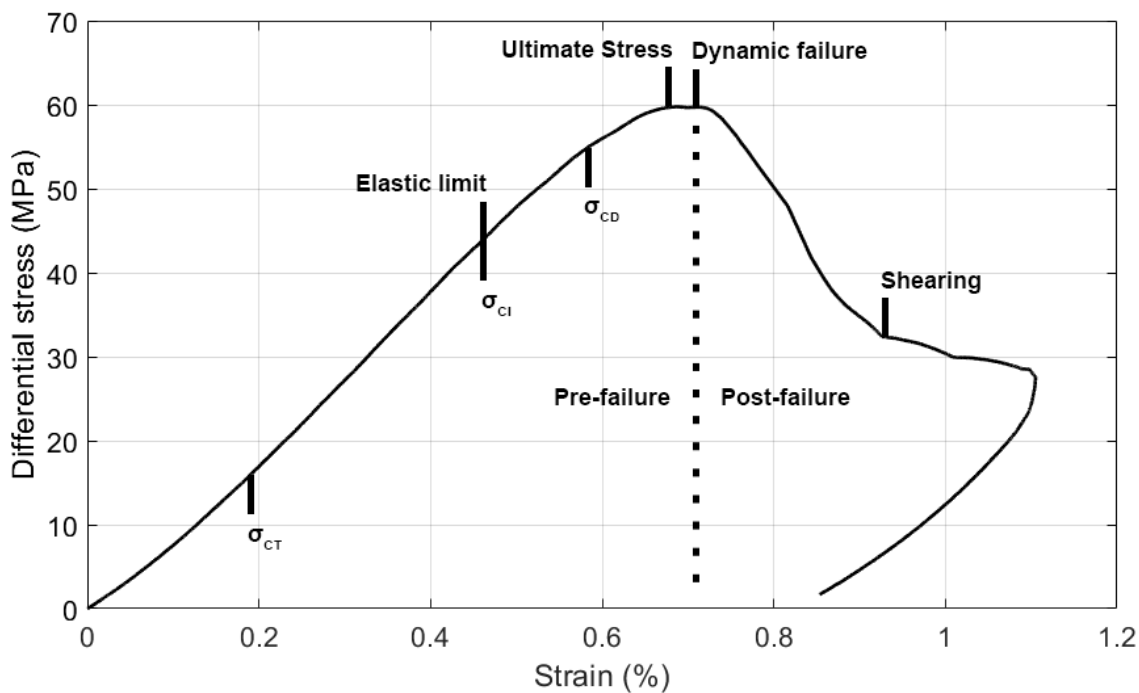


Figure 1.8: Typical stress-strain curve from deformation experiments with major stress thresholds indicated.

Deformation experiments provide a unique environment in the laboratory from which the material properties of different rocks can be determined. Tests can be performed under a range of pressure, saturation and temperature conditions allowing for the simulation of conditions found in the sub-surface. Schubnel et al. (2013) for example, modelled the generation of deep earthquakes. Fazio et al. (2019) simulated the occurrence of *Tornillo* seismic events as a marker of gas content in magma. The mechanical properties of rocks further depend on many variables due to inherent inhomogeneity in mineral composition and grain size. Such factors play a significant role in determining the overall strength of a sample.

The International Society for Rock Mechanics (ISRM) suggest standardised procedures for rock characterisation, testing and monitoring (Ulusay, 2014). The studies presented here are exclusively undertaken using experiments performed using a conventional triaxial deformation cell. In these tests, all stresses are compressive with one stress greater than the other two (which are equal in conventional testing to simplify the engineering requirements):

$$\sigma_1 > \sigma_2 = \sigma_3 > 0. \quad (1.4)$$

Although having $\sigma_2 = \sigma_3$, referred to as confining pressure, could be considered a limitation of the experimental setup, it is broadly representative of the majority of sub-surface conditions (Kovári and Tisa, 1975).

1.3 ‘CLASSICAL’ AE ANALYSIS

Recent AE systems are so powerful that the AE signal waveform can be recorded in real-time allowing for parametric characterisation of the damage during the different stages. In the literature several “classical” parameters are used to characterise AE and infer fracture or other physical phenomena. As the final goal of AE studies is to provide information to ultimately prevent sample failure, these parameters are often correlated with mechanical data (e.g. differential stress) and growing fracture structure. Standard definitions (Shiotani, 2008) used in this thesis are as follows:

1. **Threshold:** The minimum amplitude at which a signal will be detected by a sensor.
2. **Hit:** A point at which a waveform exceeds the threshold and causes a system channel to accumulate data.
3. **Trigger Time:** The time at which the signal exceeds the threshold.
4. **Peak Amplitude:** Peak voltage of the signal waveform.
5. **Duration:** Time interval between “Trigger Time” and the time of signal drops below the threshold.
6. **Rise Time:** Time interval between the “Trigger Time” and the time of “Peak Amplitude”.
7. **Energy:** Measured area under the rectified signal envelope.
8. **Average Frequency:** The mean frequency of energy over one AE event.
9. **Dominant Frequency:** The frequency where the majority of energy is stored.
10. **RA Value:** “Rise Time” divided by the “Peak Amplitude”.

Several statistical ratios have been defined that relate to the onset or rate of AE hit activity. The Kaiser effect (Kaiser, 1950) is a well-known phenomenon for quantitative assessment of damage. Where once stress has been applied and removed, AE activity will only resume once that prior level of stress is reached once more (**Figure 1.3**). As this effect begins to break down as damage propagation becomes less stable, Fowier (1986) proposed the Felicity ratio. Defined as:

$$\text{Felicity ratio} = \frac{P_{AE}}{P_{1st}}, \quad (1.5)$$

where P_{AE} is the stress at AE onset on cycle $n+1$ and P_{1st} is the maximum stress recorded at cycle n . When the Felicity ratio is larger or equal to one, the sample is considered stable and intact, whilst below this it is in a damaged condition. An expansion of this is to consider the ratios of any AE parameter between the onset and maximum stress. As the level of maximum stress is difficult to measure in-situ, the RTRI ratio (Luo et al., 2002) is sometimes applied. Rather than considering the whole test, the study can be broken up into inspection periods to identify multiple P_{AE} and P_{1st} .

Further analyses seek to quantify the level of damage from the above AE parameters. Typically, extension or shearing, mode 1 and mode 2 fracture respectively, are known to occur at different stages during deformation of concrete structures (Bažant and Pfeiffer, 1986). Mode 1 tensile fracturing is the primary means of damage nucleation as mode 2 requires enough force or weakness of the medium to generate sliding. By considering the ratios of AE hit rate between loading and unloading, **Figure 1.9a** highlights how Load (also known as the Felicity ratio, see above) and Calm (ratio of total cumulative AE activity during the unloading phase to total cumulative AE activity during the entire loading cycle) ratios can be used to assess the amount of damage between cycles (Luo et al., 2004; Ohtsu et al., 2002).

The frequency distribution of peak AE amplitudes is often modelled with the Gutenberg-Richter law. Larger values of the so-called b -value (Mogi, 1962; Scholz, 1968), defined as the slope of the amplitude distribution, indicate a larger number of small events, whilst small values suggest a relative increase in the number of high magnitude events. Although originally intended for field-scale applications, an improved b -value (Ib -value) was proposed by Shiotani (1994) for use in the laboratory. Two methods have been identified to classify the number of peak amplitudes: a) accumulated peak AE hits from the

beginning of the test; and b) the rate per unit time. The latter, however, creates unrealistic values in the lead up to dynamic failure. Further difficulties occur due to the various methods of monitoring. Different calibrations of sensor equipment, propagation medium and even factors as simply as where the AE occurs in the sample can easily modify the final value. As a result, the b -value is often considered qualitatively and is determined from the statistical mean.

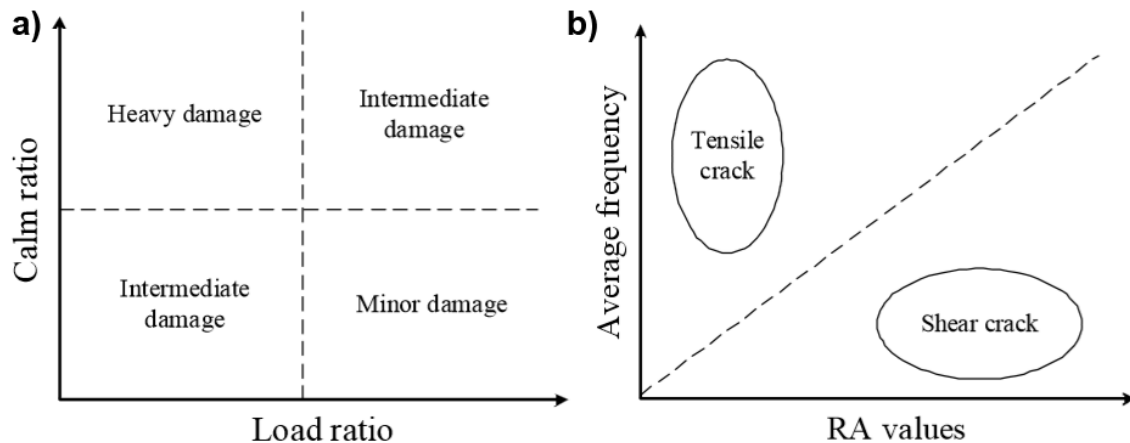


Figure 1.9: a) Damage quantification with a combination of Calm and Load ratio. b) Crack type classification with a combination of average frequency and RA values. From Grosse and Ohtsu (2008)

When considering the properties of individual AE, parameters such as average frequency and the RA value go a step further to directly classify fracturing (**Figure 1.9b**, JCMS-IIIB5706, 2003). Zhang (2018) highlighted that the dominant frequency of a fracturing event can also be related to its size and scale (e.g. Benson et al., 2010). However, the author further went on to state that these “classical” parameters are very limited in their ability to characterise AE. Rather, parameterisation should be based on waveform analysis techniques that consider the time-variant properties of the signal and relates them to the current deformation conditions.

1.4 ADVANCEMENTS PROVIDED BY THIS THESIS

Three different methodologies are proposed in this thesis. Whilst none are inherently new in the fields of rock mechanics and seismology, all the techniques presented are new to Acoustic Emission studies. The first focuses on arguably one of the most important aspects of waveform analysis, the identification or ‘picking’ of the onset of energy using cutting edge machine learning techniques. The second study seeks to characterise fracturing source mechanisms as opening, closing or shearing using a new

inversion approach that better considers the 3D geometry of the source. A third study then investigates the effect deformation structure has on a propagating waveform through qualitative analysis of forward scattering mechanisms, something which no other study has successfully applied in this context.

Accurate waveform picking is notoriously difficult as each recording is effectively unique. Varying source mechanisms, background noise and attenuation conditions result in a dataset, often >50'000 in number, that requires standardised methodologies that can account for this uniqueness. As all subsequent analyses depend on the pick time, any errors obtained at this stage will be propagated forward, potentially distorting results. To address this, a neural network is trained to recognise the onset of energy through characterisation of amplitude, frequency and noise content in **chapter 3 (page 26)**. The method is developed in such a way that a unique model can be created for individual experiments reducing the need for calibration and threshold balancing that many other picking methodologies require. Results show that it is surprisingly accurate in onset determination, greatly improving the quality and the amount of data that can be subsequently analysed.

To understand the development of a shear zone, the nucleation and propagation of fractures are characterised by the relative contributions of different source mechanisms as a sample is deformed in **chapter 4 (page 43)**. Mechanisms of tensile, compaction and shear type events are solved through least squares minimisation of the misfit between idealised focal mechanism solutions and first-motion polarity picking of AE data. Systematic testing of Alzo Granite and Darley Dale Sandstone highlight distinctive trends in the fracturing process that are dependent on the material under study and the environmental conditions.

The effects of this developing structure on a propagating waveform are studied by measuring the 'Peak Delay' of arriving energy in **chapter 5 (page 65)**. Considered the result of the forward scattering of energy by heterogeneities, Peak Delay has been analysed at the field scale to map the distribution of complex geological structure (Takahashi et al., 2009, 2007), however, there are little-to-no studies performed at the laboratory scale. Samples of Westerly Granite and Darley Dale Sandstone are deformed under conventional triaxial deformation conditions and the resultant AE analysed. Using a combined approach of quantitative analysis, tomographic mapping and synthetic modelling, this study investigates the various properties of fracture structure, i.e. length, orientation and width, on the forward scattering of a propagating wave.

2 Data Acquisition and Deformation Results

2.1 SAMPLE DESCRIPTIONS

Cylindrical rock samples are cored perpendicular to bedding (when present) with a 40 mm diameter core barrel and then cut to 100 mm length with a diamond saw. End faces are accurately ground using a lathe fitted with a cross-cutting diamond grinding disk with surfaces flat and parallel to within 0.01 mm. At 40 x 100 mm, a ratio of 2:5 agrees with IRSM recommendations and current best practices in triaxial deformation research (Benson et al., 2010, 2007). The samples, described below, were specifically selected for their homogenous properties and lack of pre-existing damage or weathering.

2.1.1 ALZO GRANITE

The mineralogical properties of Alzo Granite are typical of the white granites found in North Italy: medium grained plutonic rocks of quartz and feldspar with a high biotite content (Cavallo et al., 2004). Crystal sizes range between 2.5-6 mm for the biotite and 4-9 mm for the quartz and feldspars. Fluid porosity values are characteristically low at 0.72% \pm 0.1% (Bugini et al., 2000). Cavallo et al. (2004) report an unconfined compressive strength of 229 MPa. Four samples were selected for analysis in **chapter 4** (deformed at confining pressures of 5, 10, 20 and 40 MPa).

2.1.2 DARLEY DALE SANDSTONE

Darley Dale Sandstone is a brown-yellow, feldspathic sandstone with a modal composition of quartz (69%), feldspars (26%), clay (3%) and mica (2%). Previous studies report a connected porosity of 13.3% \pm 0.8% with grain sizes varying from 100-800 μ m (Heap et al., 2009; Zhu and Wong, 1997). The unconfined compressive strength is 160 MPa (Baud and Meredith, 1997). At the scale analysed here, no distinct layering or laminations were present. One sample, presented in **chapter 5** (deformed at a confining pressure of 24 MPa), has a small shale inclusion on the surface. Four additional samples were also prepared for **chapter 4** (deformed at confining pressures of 5, 10, 20 and 40 MPa).

2.1.3 WESTERLY GRANITE

Westerly Granite is a light-grey, near-isotropic microgranite consisting of feldspars (67%), quartz (24%), biotite (5%) and hornblende (1%) (Tullis and Tullis, 1986; T. Wong, 1982). Haimson and Chang (2000) identify an unconfined compressive strength of 201

MPa. Only a single sample of this granite is studied here in **chapter 5** (deformed at a confining pressure of 5 MPa).

2.2 LABORATORY EQUIPMENT

2.2.1 CONVENTIONAL TRIAXIAL DEFORMATION

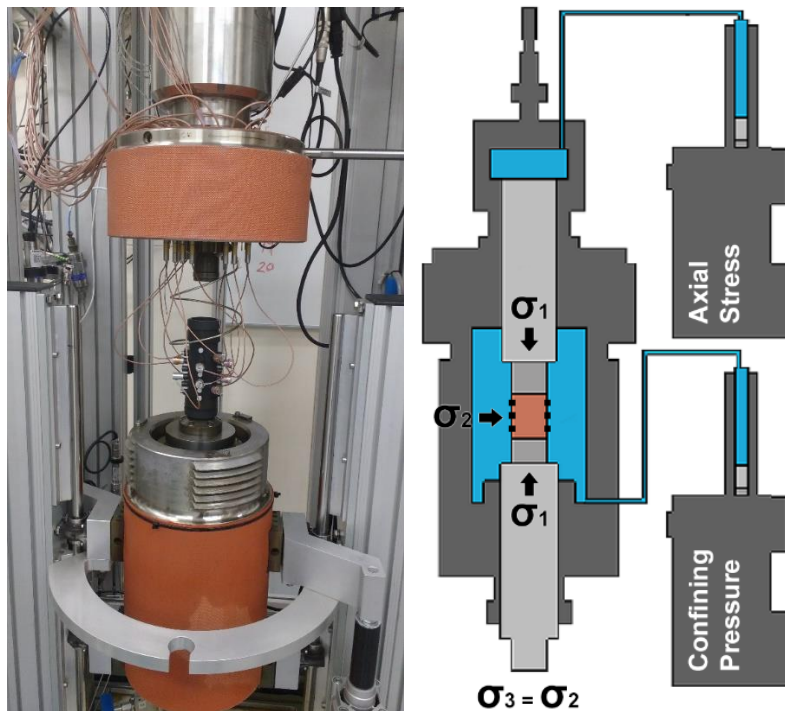


Figure 2.1: Triaxial deformation cell (left) and schematic (right). The sample is positioned inside a rubber jacket located in the centre of the apparatus (brown). AE are recorded by an array of PZT sensors (black squares) positioned along the walls of the jacket. Axial stress and confining pressure are controlled by pore fluid pumps.

Experiments were undertaken using an externally heated, servo-controlled triaxial apparatus custom-built by Sanchez Technologies (Figure 1.9). Installed at the University of Portsmouth, UK, it is designed to test 40 x 100 mm specimens at confining pressures of up to 100 MPa and temperatures of 200°C (Fazio, 2017). Composed of heating pads bonded to the vessel outer walls, temperature is applied via an external furnace and is insulated by an external jacket wrapped around the vessel to minimise heat loss. A high flash-point oil (270°C) is used as a confining medium and provides confining pressure (σ_2 , σ_3) via 100 MPa precision piston pumps. Whilst confining pressure is measured using the pump pressure directly, axial stress (σ_1) is applied via a hydraulic piston of 70 mm diameter.

This is connected to smaller piston of 40 mm diameter that directly applies stress to the study material up to a maximum of 680 MPa.

Axial displacement, or strain, is measured with an Eddy Displacement System (EDS) equipped to the apparatus. Consisting of three contactless Linear Variable Displacement Transducers (LDVTs), these devices are mounted to a ring fixed to the top driving piston. The transducers generate a magnetic field and record axial displacement by measuring the response from a target steel plate which varies with distance. Capable of sub-micron accuracy, the three readings are averaged and used to calculate strain according to the sample length. Strain rate is controlled via feedback from the three LDVTs that measure the changing length of the sample. Compared to more traditional approaches that use AE feedback to control strain rate (e.g. Lockner et al., 1991), this acquisition setup ensures that the process of fault growth is at a constant strain rate that is a better approximation of conditions found in the Earth (Lei et al., 2000).

2.2.2 STRAIN CORRECTIONS

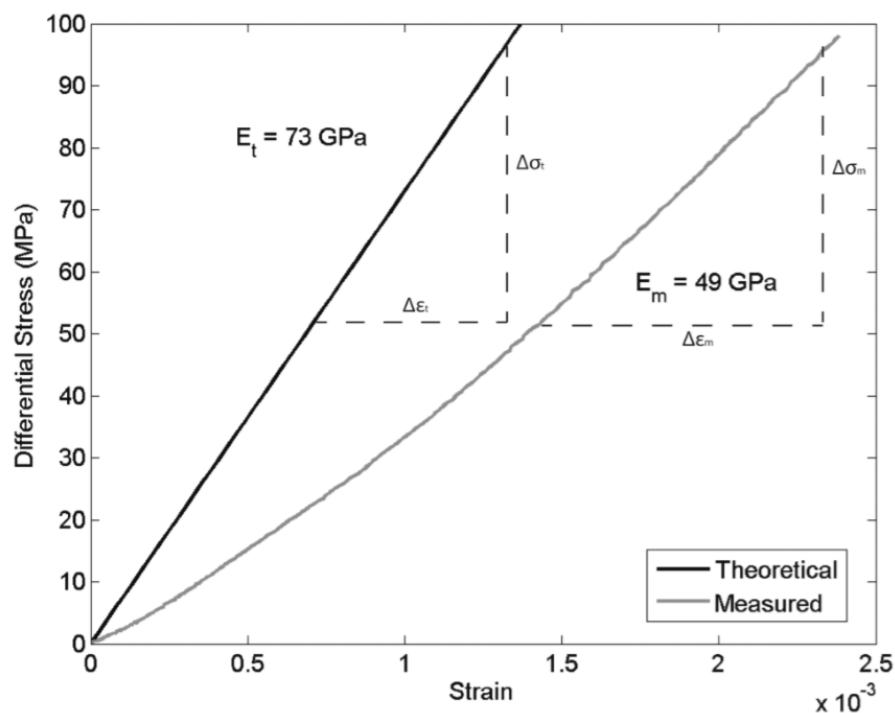


Figure 2.2: Stress-strain curve for theoretical (black) and measured (grey) values of an aluminium-alloy cylinder from Fazio (2017).

As some load will be accommodated by the apparatus itself, sample strain values must first be corrected for the Young's modulus, E , of the equipment (E_{app}). To calibrate

values, I apply the methodology detailed in Fazio (2017). Load is applied to an aluminium-alloy cylinder (100.05 mm x 40.01 mm) of a known Young's modulus ($E_t = 73 \text{ GPa}$). The strain (ε_m) is recorded using the LDVTs and the measured Young's modulus, E_m , is calculated as:

$$E_m = \frac{\Delta\sigma_m}{\Delta\varepsilon_m} = 49 \text{ GPa}, \quad (2.1)$$

where $\Delta\sigma_m$ and $\Delta\varepsilon_m$ are the incremental differential stress and incremental strain measured on the linear elastic segment of the calibration curve (**Figure 2.2**), respectively.

The Young's modulus of the apparatus, E_{app} , is calculated over the same incremental stress:

$$E_{app} = \frac{\Delta\sigma}{\Delta\varepsilon_m - \Delta\varepsilon_t} = \frac{\Delta\sigma}{\Delta\varepsilon_{app}} = 130 \text{ GPa}, \quad (2.2)$$

where $\Delta\varepsilon_t$ is the theoretical incremental strain of the aluminium-alloy cylinder and $\Delta\varepsilon_{app}$ is the incremental strain of the apparatus.

The apparent stiffness of the apparatus, k_{app} , is obtained by (Jaeger et al., 2007):

$$\Delta\varepsilon_t = \frac{k_{app}}{L * k_{app} + A * E_m} * \Delta Z_{app}. \quad (2.3)$$

Here, L is the sample length and A, its cross-sectional area. The incremental deformation accommodated by the apparatus, ΔZ_{app} , is calculated over the linear elastic segment through:

$$\Delta Z_{app} = L * \Delta\varepsilon_{app} = 0.03 \text{ mm}. \quad (2.4)$$

Rearranging **equation 2.4** for k_{app} yields:

$$k_{app} = \frac{A * E_m * \frac{\Delta\varepsilon_t}{\Delta Z_{app}}}{1 - L * \frac{\Delta\varepsilon_t}{\Delta Z_{app}}} = 1.2e^9 \text{ N/m} \quad (2.5)$$

and the corrected strain, ε_{corr} :

$$\varepsilon_{corr} = \varepsilon_m - \frac{\Delta\sigma_m}{E_{app}}. \quad (2.6)$$

2.2.3 PIEZO-ELECTRIC TRANSDUCERS

For data acquisition, the protocol of Benson et al. (2007) was followed. Each sample was positioned inside a rubber jacket in which an array of twelve 1 MHz single-component Piezo-Electric Transducers (PZTs, model PAC Nano30) were embedded (Figure 3.1). The sensors have a relatively flat frequency response between 125-750 KHz, ensuring high quality AE. The jacket was then placed inside the deformation cell and the PZTs connected to high speed digitizers (10 MHz sampling rate) via 40 dB signal preamplifiers.

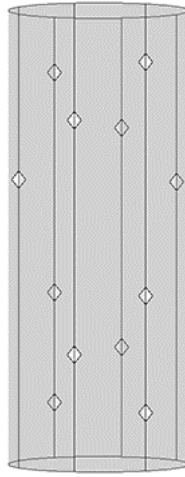


Figure 2.3: Piezo-Electric Transducers (diamonds) are evenly distributed around the sample.

Unlike traditional geophones that measure ground motion through accelerometers, PZTs are devices that use the piezoelectric effect to monitor variations (Negi and Chakraborty, 2019). As such, certain considerations must be made when analysing the data. In each of the sensors a crystal of piezoelectric material is positioned and outputs a continuous voltage. When the crystal undergoes strain, e.g. from a passing acoustic wave, the output voltage changes in proportion to the applied displacement. Due to their amplitude sensitivity, ruggedness and extremely high frequency response they have been successfully applied in numerous fields. However, due to a lack of calibration of these sensors, comparing values of amplitude or frequency content of AE with the work of others should only be done when the equipment is identical.

Active compressional (P) wave surveys for velocity measurements were obtained periodically during testing. For each survey, each PZT were individually triggered in turn

and the energy was recorded by the entire array. Triggered AE events were detected when energy exceeded a minimum threshold of 60 mV for 6 sensors. An ITASCA-Image Richter system (AE recorder) was used to digitise the signals with amplitudes recorded as a voltage. Acquired data is directly streamed to the storage system allowing for several hours of continuous data to be stored.

2.3 DEFORMATION RESULTS

In-situ measurements recorded during laboratory experimentation are shown below. Aside from changes in confining pressure, each experiment is performed identically and under drained conditions. Once the pressure vessel has been sealed, axial pressure is increased until 5 MPa to hold the sample in place without applying strain. Following this, confining pressure is increased until the desired value is met. Once the desired experimental conditions are achieved, axial load is increased causing deformation of the sample at a constant strain rate of 10^{-5} mm/second.

2.3.1 ALZO GRANITE

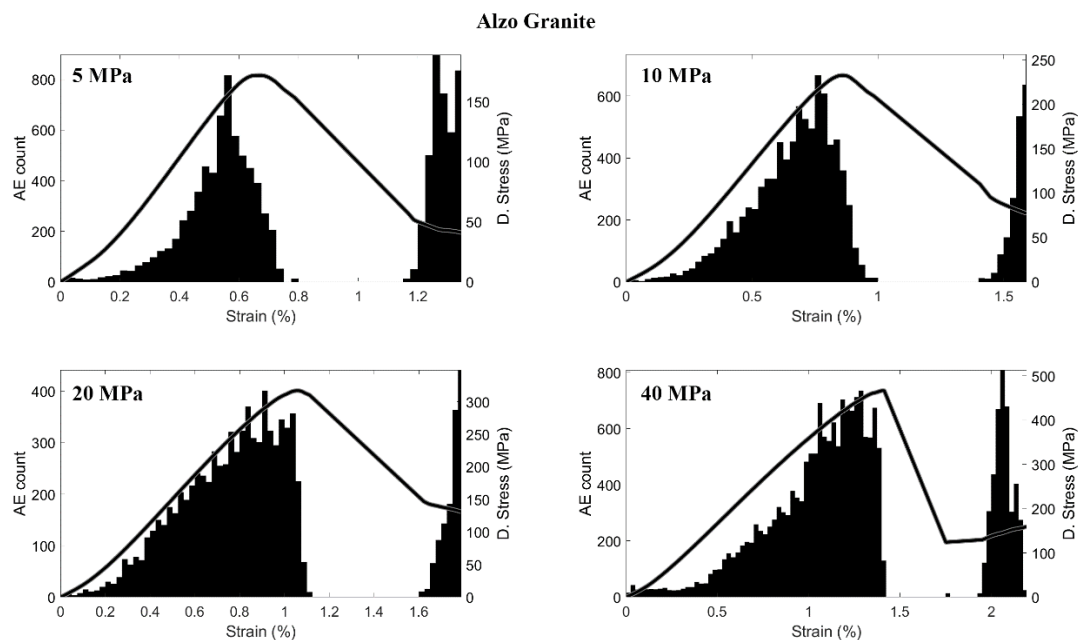


Figure 2.4: Acoustic Emission counts (black bars, 0.01% strain bins) and stress-strain curves (black line) for Alzo Granite.

Mechanical data for the four Alzo Granite experiments of **chapter 4** are presented in **Figure 2.4**. For confining pressures of 5, 10, 20, and 40 MPa, dynamic failure (**Figure 1.8, page 11**) of the samples occur at 175 MPa, 240 MPa, 325 MPa and 475 MPa

respectively. Strain values at failure are 0.71%, 0.9%, 1.1% and 1.45%. Counts of Acoustic Emission (binned in windows of 0.01% strain) follow an increasing trend once each sample has passed the crack closure threshold, peaking 0.1-0.2% before failure during crack coalescence. Post-experimentation imaging (**Figure 2.5**) highlight relatively simple deformation structure in the form of singular shear planes.

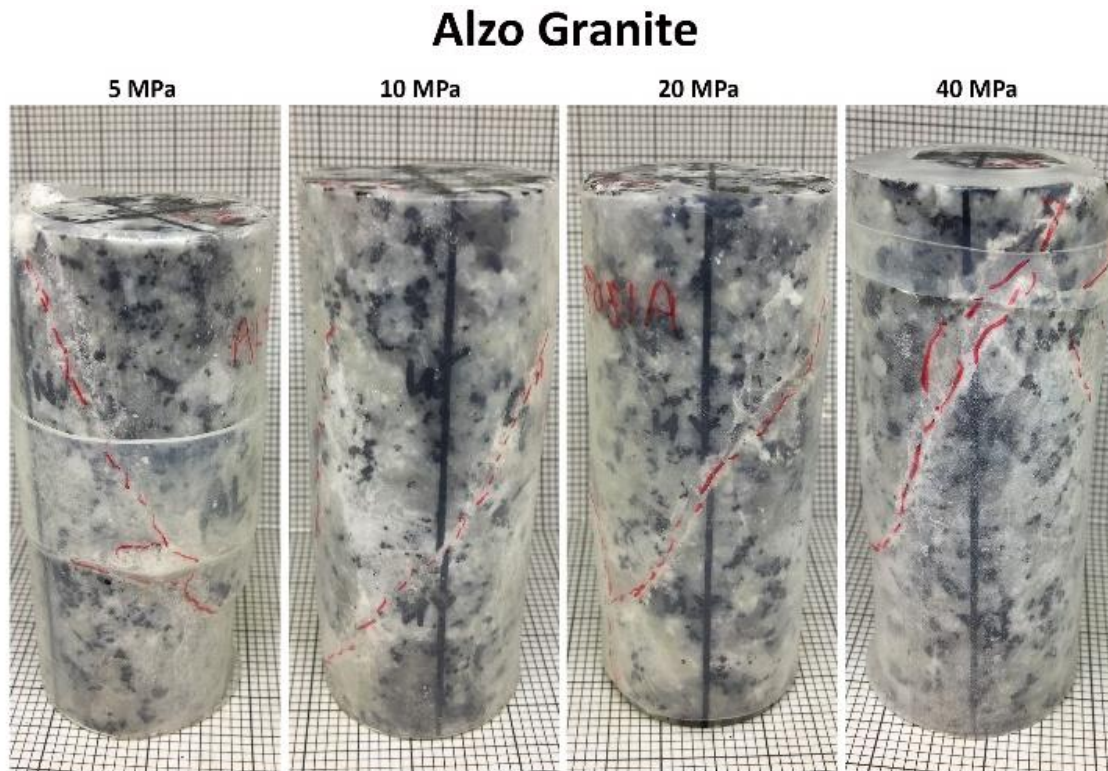


Figure 2.5: Post-experimentation imaging of Alzo Granite. Shear zone structure is highlighted in red.

2.3.2 DARLEY DALE SANDSTONE

Mechanical data for the sandstone samples used in **chapter 4** are shown in **Figure 2.6**. For confining pressures of 5, 10, 20, and 40 MPa, dynamic failure (**Figure 1.8, page 11**) of the samples occur at 60 MPa, 110 MPa, 150 MPa and 220 MPa respectively. Strain values at failure are 0.75%, 0.9%, 1.2% and 1.3%. Unlike deformation in the Alzo Granite, failure of these samples is considerably more gradual. As confining pressure increases, a pseudo-ductile like behaviour (a slow decrease in differential stress as strain increases) becomes more apparent. Counts of AEs (binned in windows of 0.01% strain) show a similar exponential increase in events as samples near Ultimate Compressive Strength. As before, post-experimentation imagery reveals relatively simple shear zone structure. With the exception of the sample deformed at 40 MPa that demonstrates conjugate structure.

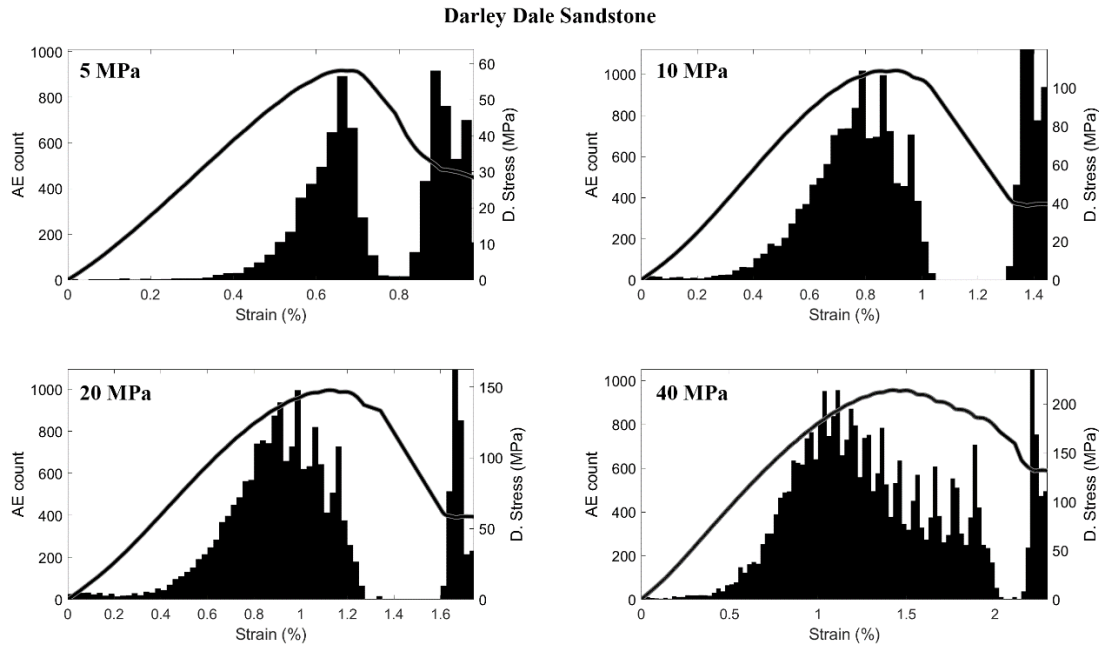


Figure 2.6: Acoustic Emission counts (black bars, 0.01% strain bins) and stress-strain curves (black line) for Darley Dale Sandstone.



Figure 2.7: Post-experimentation imaging of Darley Dale Sandstone. Shear zone structure is highlighted in red.

For the sample used in **chapter 5** deformation follows similar trends (**Figure 2.8**, left). Failure occurs at 110 MPa at a strain of 0.65%. Unlike the previous experiments, this sample was sheared after failure for 0.5% of strain. Peaks in AE count (binned in windows of 0.01% strain) correlate well with short-term decreases in differential stress. CT-imaging (Computed Tomography, **Figure 2.9**, left) reveals simple shear zone structure as a linear region (dark, less dense) from the centre right to the bottom left of the sample.

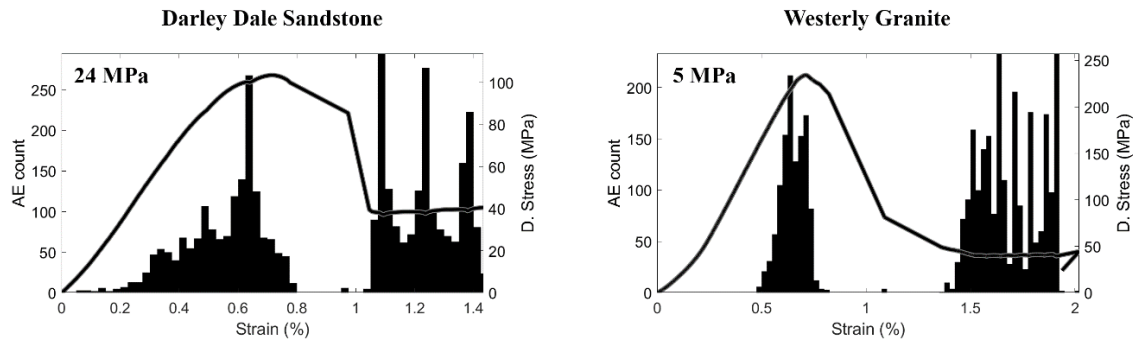


Figure 2.8: Acoustic Emission counts (black bars, 0.01% strain bins) and stress-strain curves (black line) for Darley Dale Sandstone (left) and Westerly Granite (right).

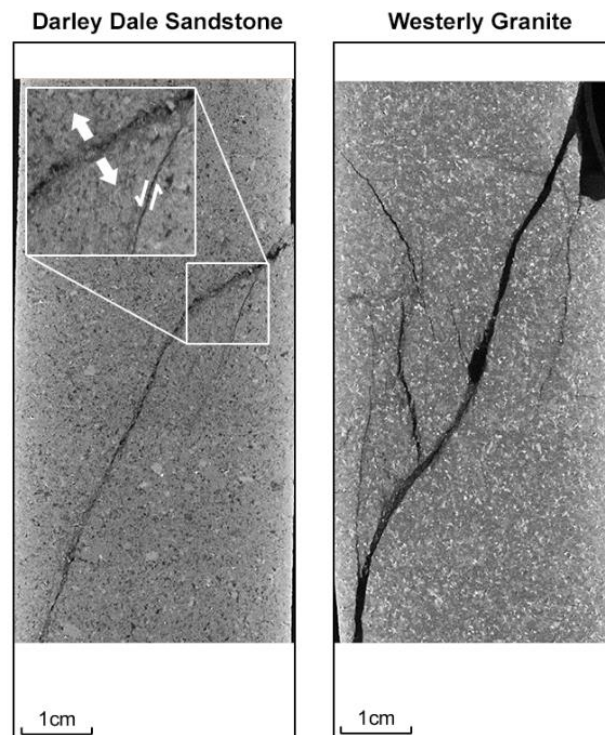


Figure 2.9: Selected CT images of the samples used in chapter 5. Deformation structure within the Darley Dale Sandstone sample is revealed to be relatively simple, whilst Westerly granite highlights diffuse and complex fracture structure.

2.3.3 WESTERLY GRANITE

The sample of Westerly Granite shows comparable trends with the Alzo Granite. A rapid increase in AE events in the lead up to failure as well as a rapid drop during crack coalescence trends (**Figure 2.8**, right). As with the sandstone sample also analysed in **chapter 5**, the sample is sheared for 0.5% of strain. Unlike the sandstone however, deformation structure is revealed to be diffuse and broadly distributed (**Figure 2.9**, right). Several faults are observed to intercept a thicker shear fracture.

3 WAVEFORM PICKING AND SOURCE LOCATION

3.1 INTRODUCTION

Acoustic Emission (AE) analysis typically falls under the category of “Big Data”. During rock deformation experiments many thousands of AE are produced by fracturing events. Depending on the acquisition setup, a single experiment can easily yield $> 60'000$ individual waveforms. Furthermore, low amplitudes, varying source mechanisms and uncertain energy arrivals complicate manual identification of the onset of energy, i.e. phase picking, resulting in possible error and uncertainty in source location. Consequently, an automated approach is required that can address the non-linearity and non-stationary nature of AE data.

Acoustic Emission refers to the release of transient elastic waves produced by the sudden redistribution of stress when a material that is subjected to an external stimulus. In deformation experiments, AE are related to the initiation and growth of fractures (Lockner et al., 1992), matrix cracking (Scholey et al., 2010), fibre breakage and various debonding processes (Bohse, 2000). Detection of these signals is a valuable asset to non-destructive testing as they provide immediate feedback of a dynamically evolving system without the need for interference. However, a notable limitation of AE analysis is that results are dependent on the successful discrimination of the signal from the background noise.

Many commercial systems currently employ a threshold-based methodology for phase picking, where signal is considered to be anything above a minimum amplitude. In situations where signal-to-noise ratios (S/N) are consistently high (e.g. > 10 dB) this method is very effective. However, as S/N reduces there is an increase in false detections and poor accuracy of phase identification (Pomponi and Vinogradov, 2013). In passive AE monitoring, where signal amplitudes can be less than -50 dB, such a method is limited to the level of noise in the dataset and the calibration between sensors. An additional weakness of such energy ratio methods is that whilst they are intuitive and less computationally intensive, they are limited by the use of a static partition window. Depending on the width of this window, the energy ratio may not be the largest at the signal onset resulting in an incorrect pick (Guoping et al., 2004). Additional difficulties are introduced by the lack of calibration of the PZT sensors typically used in AE studies (Høgsberg and Krenk, 2015).

3.1.1 HILBERT-HUANG TRANSFORM

Widely recognised in non-destructive testing, the Hilbert-Huang Transform (HHT) (Huang et al., 1998) is a powerful tool for signal analysis and data processing of AE data. Composed of two main theoretical aspects, the HHT first decomposes complex signals into a series of intrinsic modal functions (IMF) by empirical mode decomposition. Subsequently, instantaneous frequency and instantaneous amplitude content of individual IMF are then computed through Hilbert spectral analysis. Unlike a traditional Fast Fourier Transform, as the signal is decomposed in the time-domain, the time varying characteristics of AE frequency content are preserved at a high resolution with minimal aliasing of the modal components.

Already, several studies have highlighted the great potential of the HHT for classifying source and damage mechanisms. Hamdi et al. (2013) and Ding et al. (2018) evaluated the performance of the method in polymer composites. Both studies attributed different mechanisms of damage, e.g. delamination, to specific types of AE signal, whilst, Yang et al. (2014) applied the technique to monitor ‘burn’ features in surface grinding processes. Siracusano et al. (2016) even went so far as to propose separation of P and S wave signals using the HHT.

3.1.2 PERMUTATION ENTROPY

Theoretically and conceptually simple, permutation entropy (PE) is a measure of the complexity of time series data (Bandt and Pompe, 2002). Based on the distribution of ordinal patterns, which describe order relations between values of a time series, PE estimates a probability density function of the number of patterns within a sequence from which an entropy value is calculated, thus removing any dependence on amplitude values. The larger the value of permutation entropy (in the range 0 to 1) are, the higher the diversity of ordinal patterns is and the more complex the input data are (Unakafova and Keller, 2013).

Several entropy methods have been proposed and applied in a variety of disciplines such as medicine (Ródenas et al., 2015; Sharma et al., 2015), seismology (Ramírez-Rojas et al., 2018; Zoukaneri and Porsani, 2015) and rock mechanics (Jia et al., 2019; Jian et al., 2004). Through analysis of synthetic microseismic signals Jia et al. (2019) concluded that their entropy based methodology had better noise immunity and a higher sensitivity to

changes in amplitude, frequency and seismic phase compared to traditional energy-ratio techniques.

3.1.3 TIME DELAY NEURAL NETWORKS

Designed with the purpose of identifying patterns and trends in shift-invariant time-series data, time delay neural networks (TDNN) allow for the classification of data without explicitly knowing the beginning or end of a signal (Waibel et al, 1989). Similar to the PE method, TDNNs model the propagation characteristics of time series data. Used to great effect in speech recognition, TDNNs are able to construct models of the key elements of sounds, performing robustly in the presence of reverberations and even different speakers (Haffner and Waibel, 1992; Peddinti et al., 2015; Snyder et al., 2015). As AE are sounds that are prone to substantial variations in amplitude and frequency due to source and path effects, such an approach is suitable here.

Through combined characterisation of the ordinal properties of frequency content, amplitude variations and entropy estimation of the received waveforms, a distributed time delay neural network is trained to recognise the differences between noise and signal data that is unique to the acquisition setup used in the experiment. The method proposed in this study overcomes the weaknesses inherent to each of the input parameters by effectively modelling a ‘best-fit’ approach to signal classification and allows for a more accurate pickup of the first arrival even when amplitudes are too low for traditional threshold and energy-ratio based methodologies.

3.2 THEORY AND METHODS

3.2.1 HILBERT-HUANG TRANSFORM

Intrinsic modal functions represent simple oscillatory modes of complex signals. Unlike harmonic signals, IMF can have variable frequency and amplitude content through time. Known as empirical mode decomposition (EMD), IMF of individual AE are obtained through a continuous screening process called “sifting” and must satisfy the following requirements: the number of extrema and the number of zero-crossings must either be equal or differ by a minimum of one, whilst the mean of the upper and lower envelopes is zero (Huang et al., 1998).

The procedure from Huang et al. (1998) follows as thus:

1. The local extrema in the time series $X(t)$ are identified
2. Local maxima are connected by a cubic spline line to produce an upper envelope
3. This is repeated for the local minima to produce a lower envelope

The difference between $X(t)$ and the mean of the two envelopes, m_1 , is the first component h_1 :

$$h_1 = X(t) - m_1. \quad (3.1)$$

Using h_1 as the new time series, this process is repeated k times until the standard deviation of h_{1k} , σ_k , is less than 0.1:

$$\sigma_k = \sum_{t=0}^T \frac{|h_{k-1}(t) - h_k(t)|^2}{h_{k-1}^2(t)}. \quad (3.2)$$

Thus, h_{1k} is defined as the first IMF component of the data:

$$c_1 = h_{1k}. \quad (3.3)$$

Typically, c_1 contains the highest frequency component of $X(t)$. Subsequent IMF, which contain longer period data, are then calculated from the residue r_n where:

$$r_n = r_{n-1} - c_n. \quad (3.4)$$

The sifting process is stopped when r_n becomes a monotonic function from which no new IMF can be extracted. Consequently, the test data is decomposed into n empirical modes where

$$X(t) = \sum_{j=1}^n c_j + r_n. \quad (3.5)$$

Once obtained, the Hilbert transform H , or instantaneous amplitude A_{inst} , of each IMF component is calculated as:

$$H(c_n)(t) = \frac{1}{\pi} \int_{-\infty}^{\infty} \frac{c_n(\tau)}{t - \tau} d\tau. \quad (3.6)$$

The phase angle θ ,

$$\theta = \text{Im}(\log(H(c_n))), \quad (3.7)$$

is then used to compute the instantaneous frequency content f_{inst} as

$$f_{inst} = \frac{\Delta(\theta) / T_s}{2 * \pi}, \quad (3.8)$$

where T_s is the sampling period.

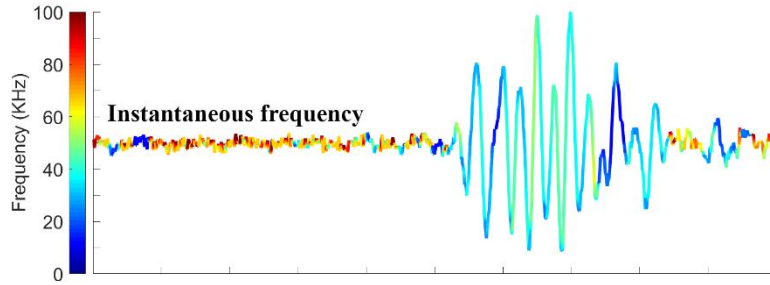


Figure 3.1: Dominant frequency content of the AE waveform. Red and blue indicates high and low frequency content respectively. Pre-signal noise is characterised by high frequency and the signal itself with low values.

To characterise the data for use in classification, each step of the vector $freq(t)$ is then defined as the $f_{inst}(t)$ of the highest $A_{inst}(t)$ of all IMF components in $X(t)$. Thus, $freq$ is simply a high-resolution vector of the dominant frequency content through time. This is visually represented in **Figure 3.1** where the colour of the AE trace indicates the dominant frequency. There are clear differences in the characteristic frequency content of the pre-signal noise (high frequency, red) and the onset of energy (low frequency, blue). The former is typically represented as high frequency data and can be considered as chaotic, with little-to-no relation between each time step. The latter, however, can easily be recognised through a consistent dominance of high amplitude, low frequency waves. It is these attributes that define the difference between AE signal and the background noise.

3.2.2 SEISMIC ENVELOPE AND PERMUTATION ENTROPY

The Root Mean Square (RMS) envelope provides a scaled amplitude estimate of the AE trace (**Figure 3.2**, red line). The envelope represents the instantaneous energy of the signal and is computed in a sliding window of 10 samples. Such a narrow window is selected to avoid smoothing of the low amplitudes at signal onset. In low-noise

environments the amplitude of the signal greatly exceeds that of the pre-signal noise and provides a good marker of the onset of energy. However, as noise increases, this onset becomes increasingly difficult to identify resulting in a high degree of uncertainty.

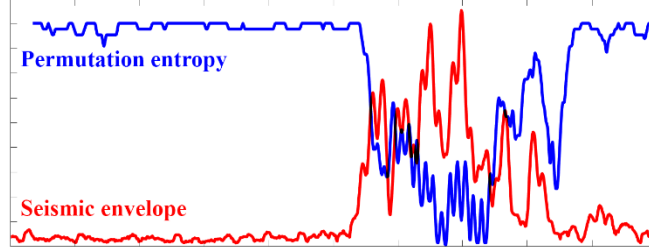


Figure 3.2: Example Root Mean Square envelope (red) and calculated entropy series (blue). Pre-signal noise is characterised by low seismic envelope values and high values of entropy and vice-versa for the signal.

The Permutation Entropy method describes the uncertainty and the degree of irregularity in a random series (**Figure 3.2**, blue line). To compute the empirical PE (refer to Unakafova and Keller, (2013) for more details), ordinal patterns of the AE are obtained with delay of $\tau = 1$, indicating a distance of 1 between points in patterns and an order of $d = 5$, meaning patterns contain 6 points ($d+1$). With a high degree of overlap between points, it is possible to use all of the information about order relations between points in the AE waveform. The distribution of ordinal patterns are obtained by the simple enumeration of the type of pattern (an example for $d = 2$ is provided in **Table 3.1**). To reflect the complexity in the time series, the PE is computed in a sliding time window of 30 points is calculated at time t as:

$$PE_d^\tau(t) = - \sum_{j=0}^{(d+1)!-1} \frac{q_j}{M} \ln \frac{q_j}{M} = \ln M - \frac{1}{M} \sum_{j=0}^{(d+1)!-1} q_j \ln q_j, \quad (3.9)$$

where $q_j = \#\{k \in \{t, t-1, \dots, t-M+1\} \text{ has the ordinal pattern } j\}$ (with $0 \ln 0 := 0$) and M is defined as the number of ordinal patterns in the window.

Table 3.1: The ordinal patterns of order $d = 2$ from Unakafova and Keller (2013).

Ordinal pattern						
$(\mathbf{i}_1, \mathbf{i}_2)$	(0,0)	(0,1)	(0,2)	(1,0)	(1,1)	(1,2)
$\mathbf{n}_2(\mathbf{i}_1, \mathbf{i}_2) = 3\mathbf{i}_1 + \mathbf{i}_2$	0	1	2	3	4	5

3.2.3 DISTRIBUTED TIME DELAY NEURAL NETWORK

In order to learn the critical attributes of noise and signal, a supervised Distributed Time Delay Neural Network (DTDNN) is sequentially trained on AE waveforms through binary separation of noise and signal data, assigned -1 and 1 respectively. Signal is defined as the time period between the theoretical onset of energy and the point at which energy drops below a pre-pick noise threshold. Due to uncertainties in the waveform content following the main arrival (i.e. reflections) the model is only trained on noise identified during the pre-signal period. Post-signal noise is classified with NaN values.

Working as a feedforward neural network, multiple time-shifted copies of the input vectors are fed into a model, where each time step (t) are applied weights that relate them to past and future values, therefore, modelling the input vectors pattern or trajectory. This is performed through 10 successive hidden layers, where each subsequent layer provides a finer characterisation of the input data. The purpose of the time-shifted copies is to remove position dependence (e.g. the beginning of the signal) and achieve shift-invariance. An error gradient is computed by backpropagation through the network across time from the binary vector. After each training epoch, the error gradients of the shifted copies are averaged and then used to apply a weighting update. Thus, the network only learns the most important features of the input data. The output of the network is a binary vector from which the onset of energy can be identified (**Figure 3.3**). Intermediate values between -1 and 1 highlight the uncertainty of signal classification. Performance of the network is measured by the mean square error between the binary training vector and the output model.

Initially, the model is trained under supervision. Five high amplitude waveforms are randomly selected from an AE pool. They are manually picked, and the model iteratively trained on the concatenated input parameters (training dataset) after each waveform. At this stage, the model already has a relatively high degree of picking accuracy. Following this, the model then undergoes semi-supervised training. A waveform of any amplitude is randomly selected from the available pool. The input parameters are calculated and are simulated in the neural network model generating an output model.

The difficulty in this methodology is picking the signal onset from the output model. The simplest approach tested here was to define a window around the likely onset, typically between the minimum and maximum values of the model output, and then select the highest signal-to-noise ratio (SNR) of the original waveform in this window. From a physical

perspective (i.e. sample dimensions, acoustic velocity) there can only be a limited time window for subsequent energy to arrive, thus the window is set to between 20 and 60% of the waveform length. For subsequent waveforms for that event, this window is then set between the first arrival pick and that time plus 20% of the waveform length. The actual arrival time occurs approximately at the mean value of the model output between the minimum value in the window and 80% of the maximum. Several approaches were tested to select the onset in this window: when the model output equals zero, when the gradient along the model output exceeds a certain value. However, for the sake of simplicity, the onset was identified as the highest S/N ratio of the input waveform around this point.

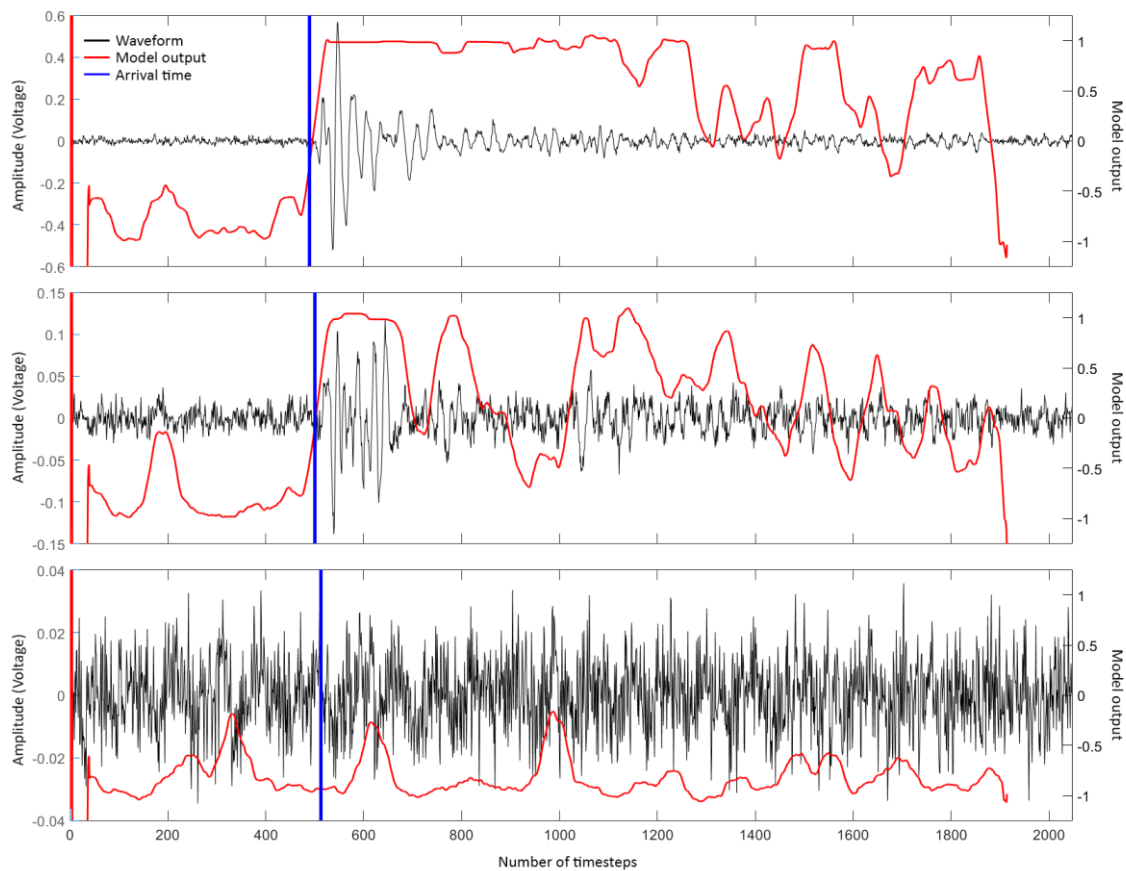


Figure 3.3: Model Output (red) provides a simpler time series from which to automatically identify the signal onset (blue). Portions of the waveform confidently classified as signal are represented by a 1, whilst pre-signal noise is classified as -1.

Once the onset is identified, two ‘picking quality’ ratios are calculated around this value. A short-term SNR of the original waveform and an SNR of the model output. With extensive testing it was found that an SNR value of 2 for the former and values between 0.3 and 0.9 for the latter were a reliable threshold. When both ratios are exceeded, the input

parameters are added to the training data and the neural network is updated. To improve computation speed, the model is trained in batches of 10 waveforms. Waveforms can be further down sampled to increase computation speed. As this is an iterative process, the model is steadily improved over time which allows for the later inclusion of data that may not have been initially included. The model ceased training once the training dataset exceeded 300 waveforms.

3.2.4 SOURCE LOCATION

During the deformation test (**Figure 2.7 page 23**, 20 MPa), 12 waveforms are recorded for each AE event. The waveforms are ordered in descending value according to their amplitude and simulated in the neural network model. The first trace (the highest amplitude and so likely the first to arrive) is picked within the same window definitions used in model training. Subsequent traces are picked within a window between this first arrival and maximum possible arrival time set according to the velocity of the medium. For the traces of length 2048 timesteps analysed here, the window was 350 timesteps wide. This window was then iteratively narrowed according to the model output. For low amplitude waveforms, this windowing proved crucial in identifying the correct peak in the model output (**Figure 3.3**, lower trace).

Once the onset of energy has been identified for each arrival, pick times are inverted for source location using a Time Difference of Arrival (TDOA) method (Comanducci et al., 2020; Tobias, 1976). Although weak to velocity anisotropy, TDOA is commonly used in micro-seismic source location. TDOA values are calculated by pairwise subtraction of the time of arrival values to each sensor from a single source. Theoretical TDOA values are calculated through iterative estimation of the source location. The L2 norm of the residual between theoretical and true TDOA values arrives to a local minimum at the true source location. A minimum of nine arrival times is recommended as location errors begin to stabilise at this point; the accuracy of this method greatly improves with the addition of more sensors.

3.3 RESULTS AND DISCUSSION

3.3.1 ALL PARAMETER MODEL VALIDATION

To validate the final neural network, performance indices are calculated for the training dataset once it is complete. In batches of 10 waveforms, two new models are

sequentially trained as before. For each model, the remaining data that is yet to be included into the model is then used as the validation dataset. For each validation waveform, a mean square error (MSE) between the model output and the idealised binary training vector ($[-1 \ 1]$), and the actual picking error. The latter is measured in timesteps (dimensionless) around the true arrival, negative values indicate early picking, whilst positive indicates late. With the second training instance, the training dataset is the validation dataset. The purpose of the first model is to assess the ability of the neural network to solve data it has not seen, whilst the second model investigates how well the model can solve its own training data. Performance indices (**Figure 3.4**) demonstrate a high degree of accuracy of the model, even when the training data count is low. A reduction in the mean square error for both models highlights a steady improvement in noise and signal classification. An increase in average picking error in the first model (**Figure 3.4a**) at 125 training data suggests the inclusion of difficult to classify waveforms, however, the error is rapidly reduced at 200 training data. For the second model (**Figure 3.4b**), results are steady throughout training, demonstrating the consistency of the semi-supervised methodology used. For both models, an MSE of 0.25 is acceptable as pre-signal noise is rarely free of artefacts in AE data.

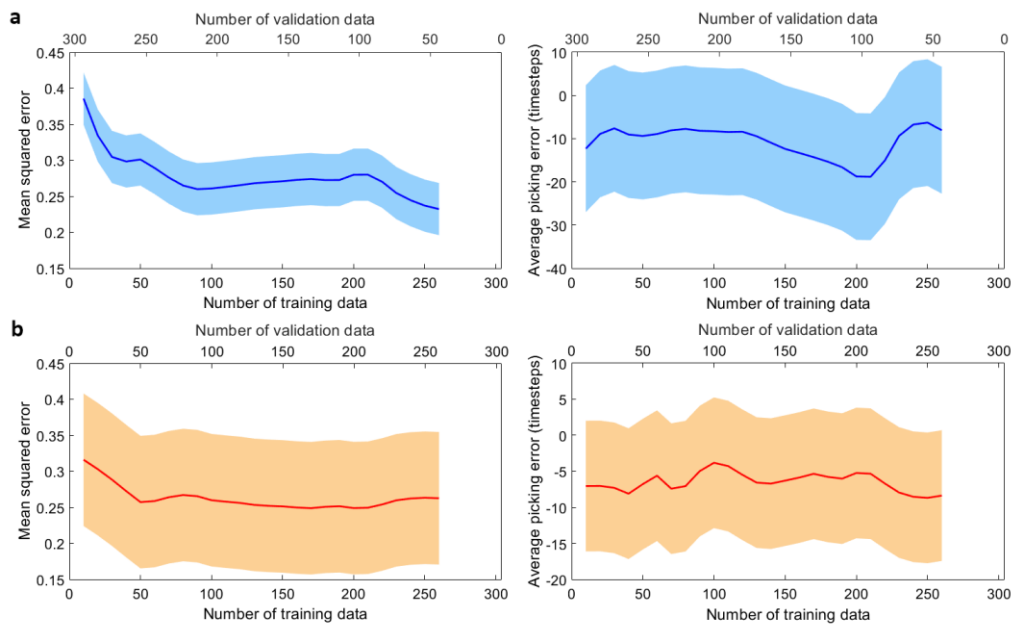


Figure 3.4: a) A model is sequentially trained in batches of 10 waveforms and then validated with the remaining data. Dark lines indicate the average value of performance indices and the lighter region indicates the 95% confidence interval. b) Here the model is validated on its own training data after each batch of 10 waveforms.

Further validation is performed through analysis of the error distribution according to waveform amplitudes (**Figure 3.5**). A histogram highlights a gaussian distribution to the training data. Picking errors (timesteps) highlight problematic amplitudes plotted as averages and their 95% confidence interval. It is likely that the large errors observed at -82 dB and -60 dB are associated to only one or two difficult waveforms. However, it is also important to observe the similarity in error distribution between the two models, suggesting a uniqueness to the final neural network solution.

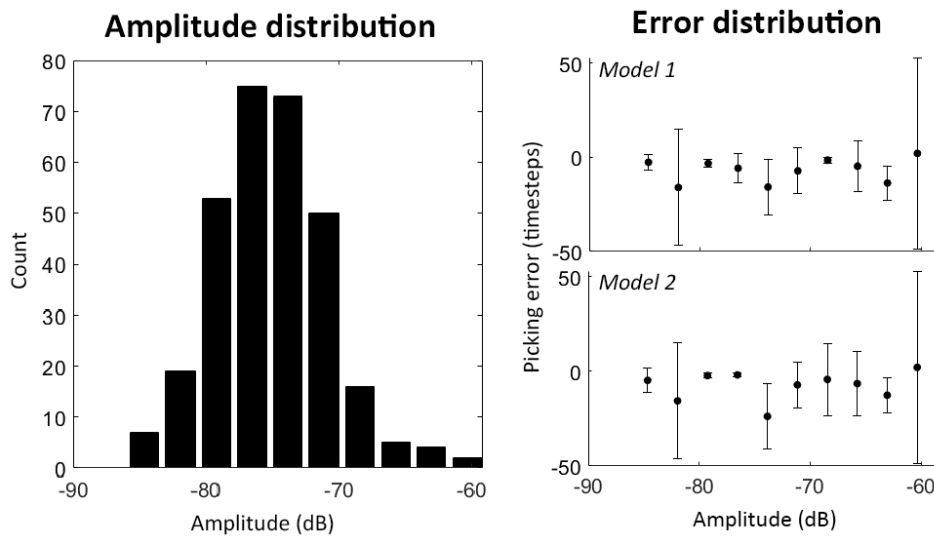


Figure 3.5: Amplitude distribution of data used in training the neural network model (left) and associated picking errors (black circles) with 95% confidence interval plotted as error bars (right).

3.3.2 SINGLE PARAMETER MODEL VALIDATION

As in the previous section, performance indices are calculated for two separate validation models, however, only a single input parameter is tested for each model. Results for neural networks training only on instantaneous frequency, seismic envelope and entropy are plotted in **Figure 3.6**, **Figure 3.7** and **Figure 3.8**, respectively. Both instantaneous frequency and seismic envelope impart relatively low errors. The seismic envelope rapidly converges to a solution that is able to solve known and unknown data. Entropy on the other hand, produces the largest error of the three input parameters. After 175 training data, the MSE rapidly increases.

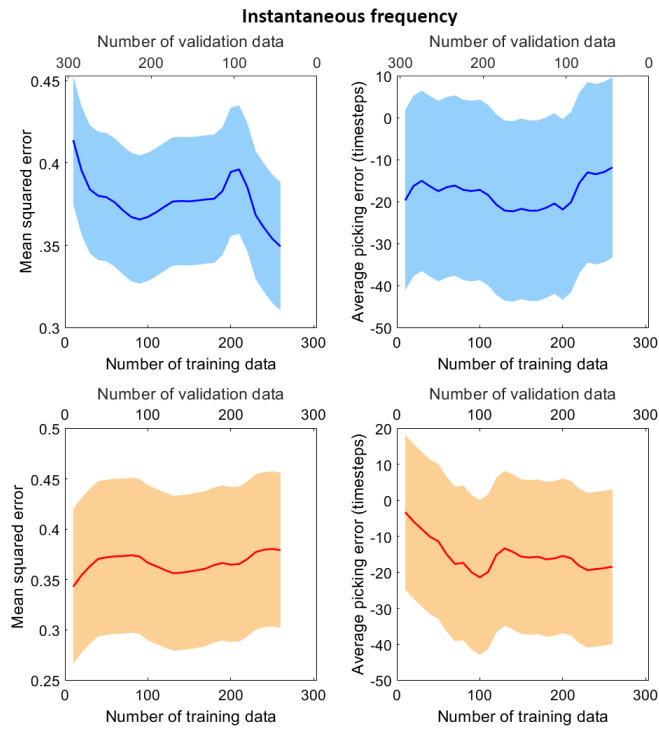


Figure 3.6: Validation of model trained only on instantaneous frequency content. Dark lines indicate the average value of performance indices and the lighter region indicates the 95% confidence interval.

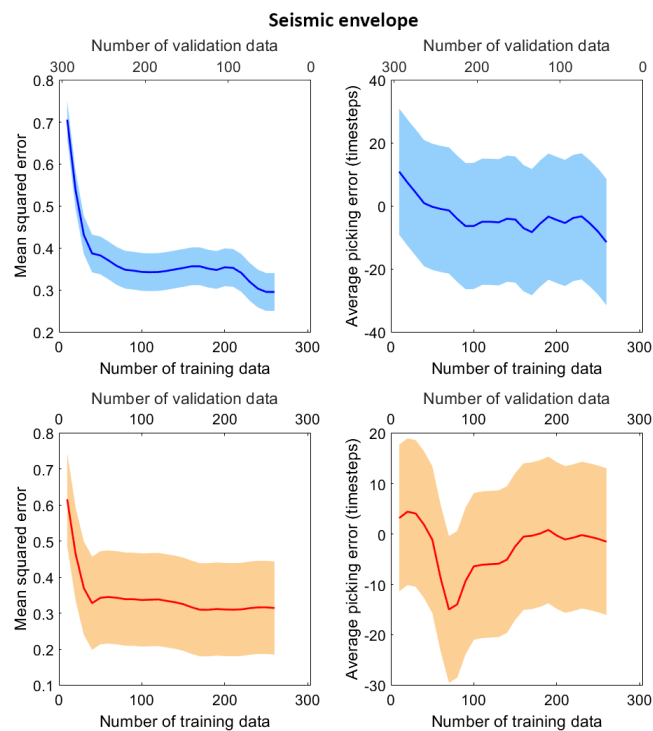


Figure 3.7: Validation of model trained only on seismic envelope. Dark lines indicate the average value of performance indices and the lighter region indicates the 95% confidence interval.

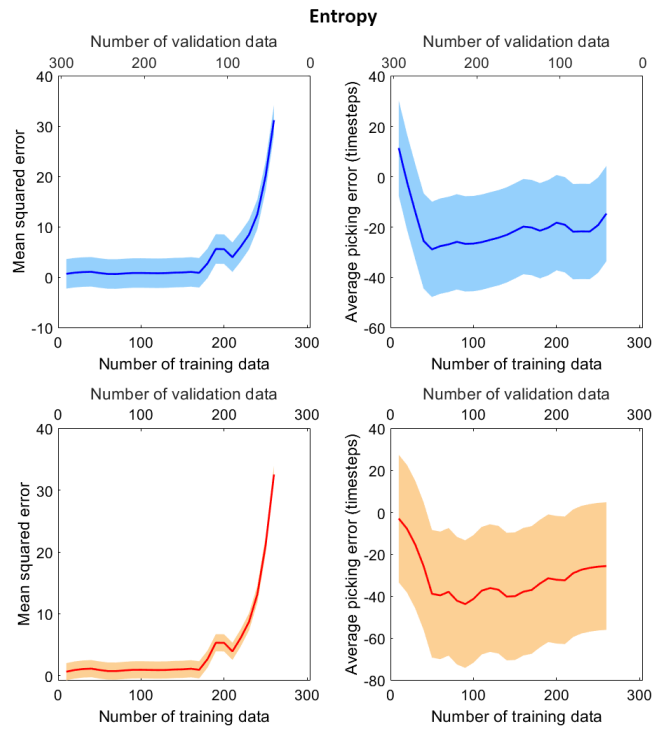


Figure 3.8: Validation of model trained only on entropy. Dark lines indicate the average value of performance indices and the lighter region indicates the 95% confidence interval.

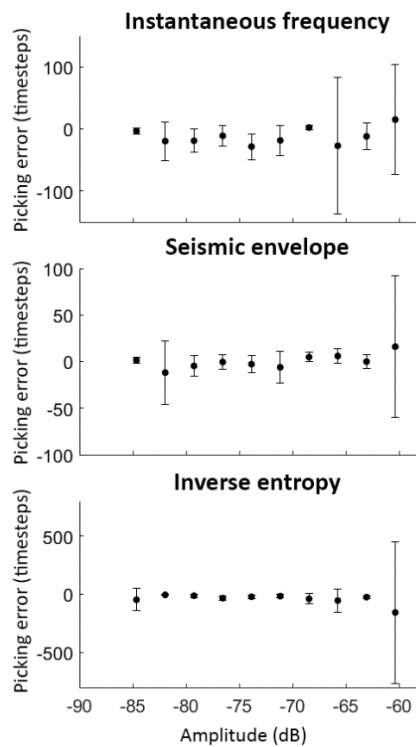


Figure 3.9: Associated picking errors in amplitude windows for the single parameter analysis.

The reason behind this becomes clear when examining the error distribution according to waveform amplitude (**Figure 3.9**). A significantly large error is created at the highest amplitudes. As stated before, this was found to be generally linked to one or two problematic waveforms, where the high amplitudes were producing anomalous entropy measurements. Whilst the semi-supervised approach is not without its flaws, the inclusion of several different waveform parameterisation methodologies acts to minimise the individual weaknesses of each. However, care should be taken to remove difficult data and ensure adequate sampling of the whole amplitude range. The histogram in **Figure 3.5** suggests a minimum of 50 waveforms for each amplitude window (windows with less than 50 waveforms show the highest errors).

3.3.3 FULL-DATASET VALIDATION

Following the training of the neural network model, all waveforms from the triggered AE dataset are picked using the model. Sources are then located using the TDOA methodology. Of the 24360 detected AE, 6741 events are located within the sample, a recovery rate of 27%. Of the 12 available arrivals, an average of 11 are picked for each AE. Example waveform pick results for 2 AE are detailed in **Figure 3.10**. Both AE demonstrate a significant degree in variety in the character of the onset of energy. The second highlights an additional weakness of the acquisition setup used here. The PZT used to record AE, detect both P and S waves. At longer hypocentral distances (>1 cm) the P-wave tends to become heavily attenuated resulting in poor detection. As a result, it is likely that the S - wave is picked in most cases. In the second AE, the first two arrivals have a P-arrival. A more in-depth methodology that can characterise these two separate onsets is required to overcome this. Although it does not play a significant role in this test, this is a likely cause of some of the errors occurring at high amplitudes seen previously.

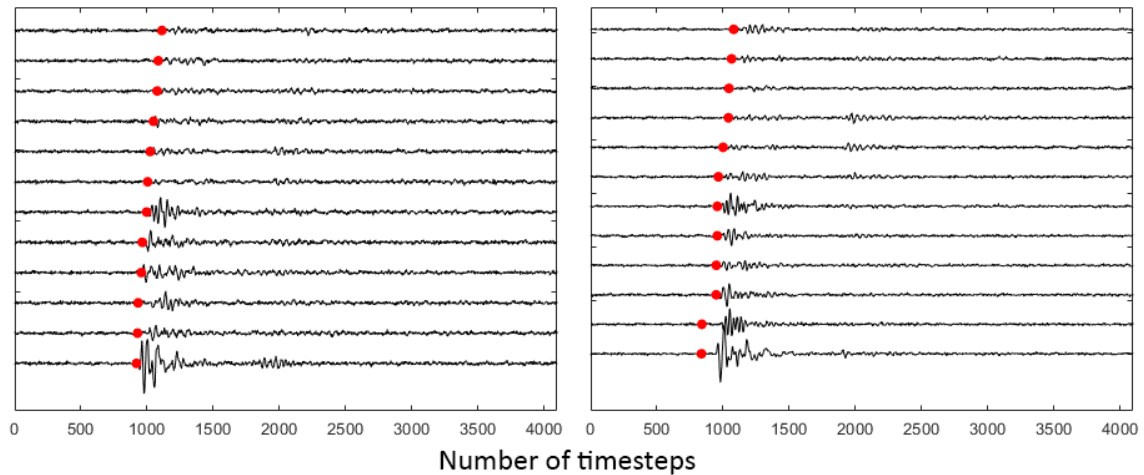


Figure 3.10: Example AE with their recorded waveforms picked (red dots). Note in the second AE (right) the picking of a P-wave arrival for the bottom two waveforms.

As a simple comparison, the same dataset is also picked using a simple RMS envelope threshold-based method. When waveform amplitudes exceed a set value of noise, an arrival time is identified. AE are then relocated using the above TDOA methodology with source locations plotted as scatter and density plots in **Figure 3.11**. Approximately four times as many events were successfully located by the neural network as compared to the threshold approach. Whilst both methods highlight source locations that localise to a shear zone (**Figure 3.11**), it is much more apparent in the method presented by this study.

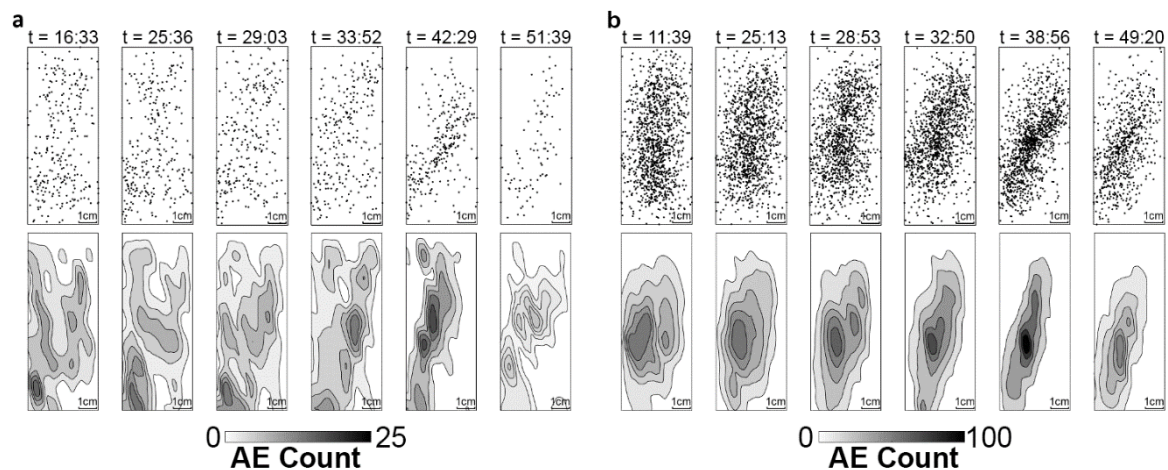


Figure 3.11: Source locations plotted as density plots. Data are plotted in 1200 event bins. a) Data picked with a threshold method. b) Data picked with the Neural Network results in a higher density of source locations and cleared fault zone structure.

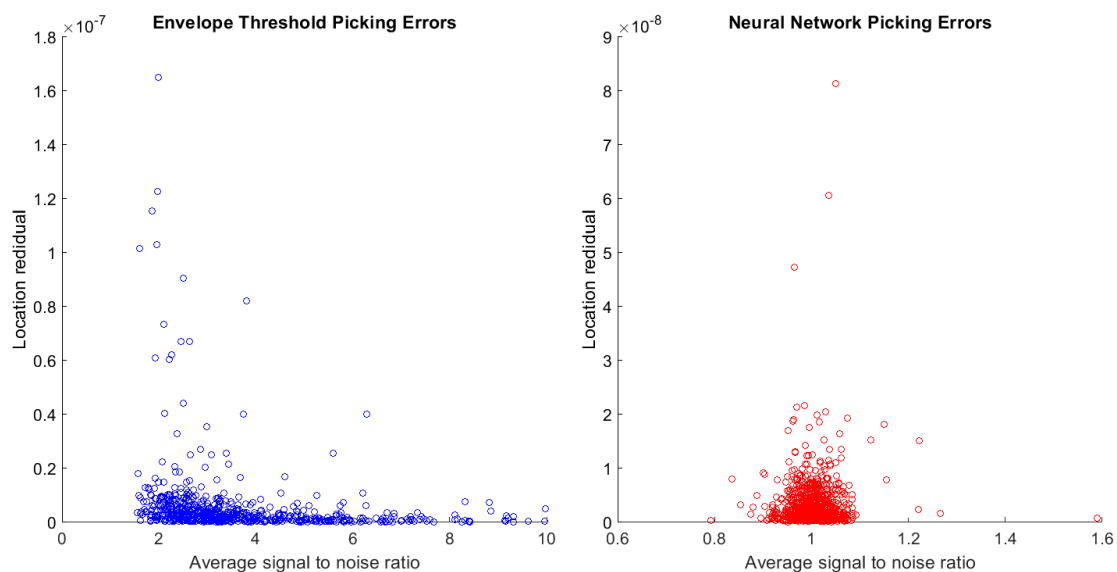


Figure 3.12: Picking errors are compared for both methodologies. The threshold method has very high location residual errors compared to the neural network for low signal to noise ratios.

Average signal to noise ratios further demonstrate systematic behaviour and a robust repeatability of the neural network (**Figure 3.12**). For the envelope method, high location residuals typically correlate with low S/N and vice versa for low, suggesting that the quality of picking plays a fundamental role in the location accuracy. However, for the neural network the average S/N value is 1 and the location residuals are far lower than the other. One explanation is that the neural network is more reliably picking low amplitude data, thus bringing down the average, or more likely, it is identifying the discrete change in waveform characteristics when an acoustic signal arrives.

3.4 CONCLUSIONS

This study has presented a workflow and an application of a machine learned waveform picking tool. A distributed time delay neural network is trained to recognise the onset of AE energy using instantaneous frequency, seismic envelope and entropy measurements. Statistical results demonstrate the reliability of the method and highlights the strength in using multiple waveform characterisation techniques in determining the arrival of acoustic energy. It is not crucial that the techniques presented here are the ones that are used. Any method that highlights a distinct change in character for each phase (i.e. pre-signal noise, signal) will work here. One advancement of this approach that could potentially be made is to characterise the differences between different wave types (e.g. P-wave, S-wave) and pick the individual onsets of those.

It is important to stress that this is a fully automated process that can be applied to nearly any AE dataset the authors can think of. Aside from the 5 waveforms used to initially train the model no user intervention is required. A high degree of picking accuracy and the inclusion of low amplitude data that may normally be missed by traditional single parameter threshold methods results in datasets with a high source location recovery rate and a reduction in the propagation of errors in further analysis of the data.

4 FOCAL MECHANISMS AND SOURCE EFFECTS

4.1 INTRODUCTION

Fracturing of brittle media in the lead up to dynamic failure occurs as a result of discrete, sudden releases of stress. This accumulation of damage eventually leads to the connection of structure and coalescence of a fault. During controlled laboratory deformation experiments, fault growth is considered to be analogous to the development of earthquake rupture due to a statistical similarity in source dimensions (Hanks, 1992). Studies of Acoustic Emission (AE) data, the laboratory counterpart to seismic waveforms, are very useful as they highlight the development of fault zone structure in a controlled environment. Several studies point towards sequences of fracturing mechanisms that occur as damage propagates. Lei et al. (2000) demonstrated the occurrence of tensile fracturing at the front of a ‘process zone’ with significant shear cracking following in its wake. The authors further concluded that the linkage between fractures formed the major mechanism of crack interaction and fault development prior to the yield point. Experiments on fine-grained granites suggest that this process is tensile dominated (Cox and Scholz, 1988), however a more significant shear-component is highlighted in coarser grained material (Lei et al., 1992).

Although representing at least 30% of fracturing mechanisms (Graham et al., 2010; Stanchits et al., 2006), an often overlooked aspect of shear zone development is the Compensated Linear Vector Dipole (CLVD) or ‘closure’ fracture mechanism. Vavryčuk (2005) observed that shear fracturing in anisotropic media comprises of varying contributions of tensile and compaction components that is dependent on the orientation of faulting. The author highlighted a similarity in the directional variability of both components suggesting a common influence between the two. As the pressure required to keep a fracture open is lower than it is to extend (Belyadi et al., 2017), any open flaws ultimately play a role in shear zone formation as they will act to accommodate any applied strain before new tensile fracturing occurs. For example, van der Baan et al (2016) cyclically varied fluid pressures near the crack tip to simulate non-continuous fracturing. The authors observed that a drop in local pressures resulted in partial fracture closure and temporarily halted or slowed fracture propagation. As closing fractures also amplify local stress concentrations, new fractures may further develop and grow in proximity (McBeck et al., 2019). This ‘excitation’ of fault growth, where the propagation of unstable fractures

encourages the development of others in the vicinity (Chen et al., 2014), is an important aspect of shear zone formation as it ultimately leads to dynamic failure of the rock mass.

Determination of fracturing mechanisms typically falls under two categories: first-motion polarity analysis (e.g. Graham et al., 2010; Stanchits et al., 2006), and moment-tensor inversion (e.g. Vavryčuk, 2002, 2001). A study demonstrated that the solutions for both methodologies result in broadly similar observations and trends suggesting that the choice of either approach will be due to limitations of the AE acquisition setup (Graham et al., 2010). Particularly the application of the moment tensor is more complicated at the laboratory scale due to reflections and other ringing effects distorting the waveform coda. On the other hand, they also noted that the use of an average polarity method to calculate focal mechanisms led to poor representation of the non-shear components of fracture development.

To address these limitations this study applies a least squares methodology whereby first-motion polarity measurements are fitted to idealised focal spheres of tensile, shear and compaction type fracturing. This approach leads to a better representation of the 3D geometry of the source. It is however limited by the idealised spheres used in the fitting. Acoustic emission data from systematic testing of Alzo Granite and Darley Dale Sandstone highlight distinct fracturing processes in the lead up to dynamic failure that are dependent on the rock type and the confining pressure used.

4.2 METHODOLOGY

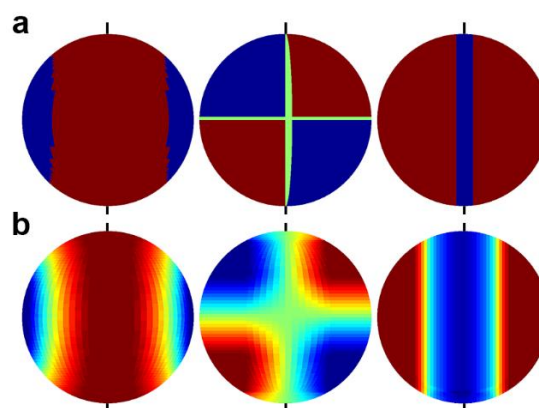


Figure 4.1: a) Absolute polarity of idealised focal mechanisms of C-type (left), S-type (middle) and T-type (right) fracturing. b) Deviatoric amplitude distribution of the same mechanisms.

Samples of Alzo Granite (**Figure 2.5, page 22**) and Darley Dale Sandstone (**Figure 2.7, page 23**) are deformed until dynamic failure at confining pressures of 5, 10, 20 and 40 MPa. Following picking and location (**chapter 3**), first motion amplitudes and their polarities are obtained for each waveform of the AE. The objective of the following procedure is to minimise the fit between idealised focal spheres of tensile (T-type), shearing (S-type) and compaction (C-type) events through iterative rotation (azimuth and elevation) of the picked polarity measurements. Polarity amplitudes are normalised according to the maximum amplitude arrival of each AE event and projected onto a sphere of the same dimension of the idealised models. Two constants are obtained and multiplied together to solve the minimisation problem; the L2 norm of absolute polarity (-1 or 1, **Figure 4.1a**) and the L2 norm of deviatoric amplitudes (smoothed distribution, **Figure 4.1b**), both calculated as the sum of least squares of the residual between idealised mechanism and the measured normalised amplitude distribution. Estimated orientation of a fracture plane is indicated by the black lines. Dip and dip direction are calculated relative to this plane. Although this may not be 100% correct for shearing events, either plane may be selected, normal faulting parallel to the shear direction is assumed for most of these data under compressive conditions.

There are some limitations of this approach. First is the choice of segmentation of the idealised focal spheres. In reality, fracturing mechanisms fall on a range of distributions between pure compaction, pure shear and pure tensile (Frohlich et al., 2016). Unlike MTI, this method is limited to specific motions and so for example, is unable to precisely identify the amount of shear in a tensile event. The addition of intervening mechanisms to the inversion procedure would address this but would significantly increase processing time. Furthermore, an additional limitation of this method is that it does not consider attenuation or other scattering effects of the recorded waveforms which may affect the fitting to the deviatoric mechanism.

For each mechanism type, probability density functions (PDF) are calculated for the time of occurrence of individual AE (converted here to a strain value). Data are further separated by AE amplitude. Low amplitude data are AE with amplitudes in the bottom 5% of the total amplitude range for each mechanism of an experiment. A relative threshold was selected as amplitudes are not calibrated between sensors and experiments. These PDF are then summed together, and a percentage contribution calculated. This approach was selected instead of histogram bins as it resulted in a smoother distribution and better

highlighted trends in the data. To ensure trends are statistically relevant, percentage values are calculated every 10 events for a specific experiment and then smoothed in a moving window of 0.04% strain. Plots are broken up into three characteristic deformation stages that correlate with phases of: a) Fracture Nucleation and Fault Growth (0 - 70% UCS), b) Crack Coalescence (70 - 95% UCS), c) Dynamic Failure of the sample (>95% UCS).

4.2.1 MECHANISM ORIENTATIONS AND DIVERGENCE MAPS

Assuming a dominance of normal faulting under compressive conditions, fracture azimuth and dip are assumed as slip vectors in order to calculate the divergence between neighbouring events. Vector directions are interpolated onto a 3D grid to identify broader trends, after which the along-strike component is set to zero to calculate vector divergence as a 2D plane. Data are windowed according to the previously discussed deformation stages. Colours scales are calibrated to individual plots to highlight contrasting structure.

4.3 RESULTS

Spatio-temporal variations of solved focal mechanism solutions are shown in the following section. Individual samples are discussed below. Phases of 1) Fracture Nucleation and growth, 2) Crack Coalescence and 3) Dynamic Failure are indicated in each of the panels. The current sample is in the top left of the figure with a failure plane drawn on the hand sample in red. Probabilities of solved mechanisms occurring at a specific strain highlight the relative proportions of T-type (tensile, yellow). S-type (shear, green) and C-type (closure, blue). A specific period of fracture development marked as a red line and called $\epsilon_{critical}$ is indicated for each sample. Spatial maps of fracture polarity orientation and mechanism slip divergence are plotted beneath with the observed failure plane marked with a dashed red line.

Alzo Granite at 5 MPa

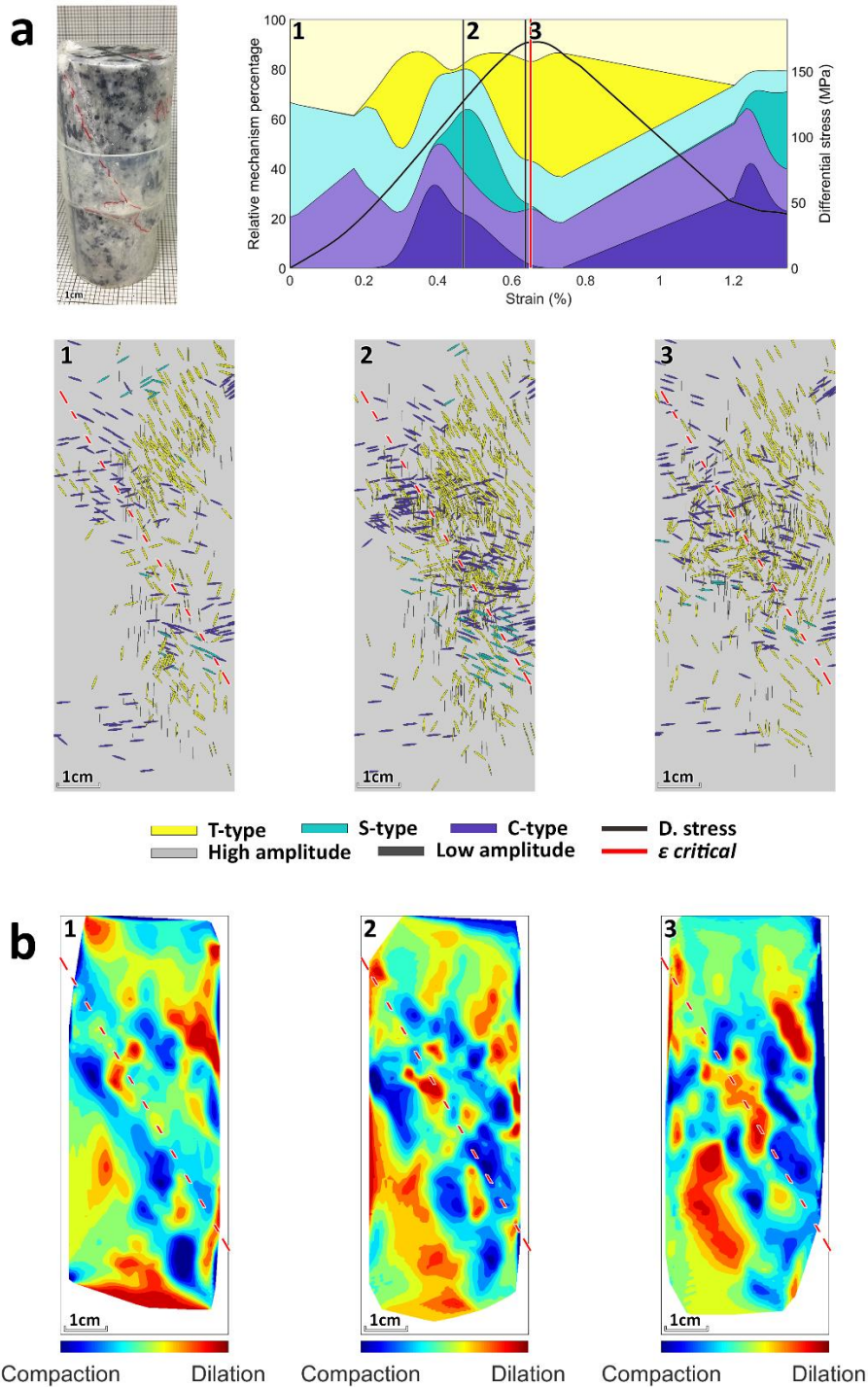


Figure 4.2: a) Post-failure imagery and fault plane in red (top left) for Alzo Granite at 5 MPa. Focal mechanism probabilities (top right) show T-type (yellow), S-type (green) and C-type (blue) events separated by amplitude (lighter for high, darker for low) as strain increases. Fracture mechanism plane distributions (bottom) show the spatial distribution and orientations of events. b) Divergence maps of mechanism slip vectors. Red regions indicate dilatational regions where vector directions are diverging. Blue indicates compactant regions where vector directions are converging. Data are windowed into phases of 1) Fracture Nucleation and Growth, 2) Crack Coalescence and 3) Dynamic Failure.

Alzo Granite at 10 MPa

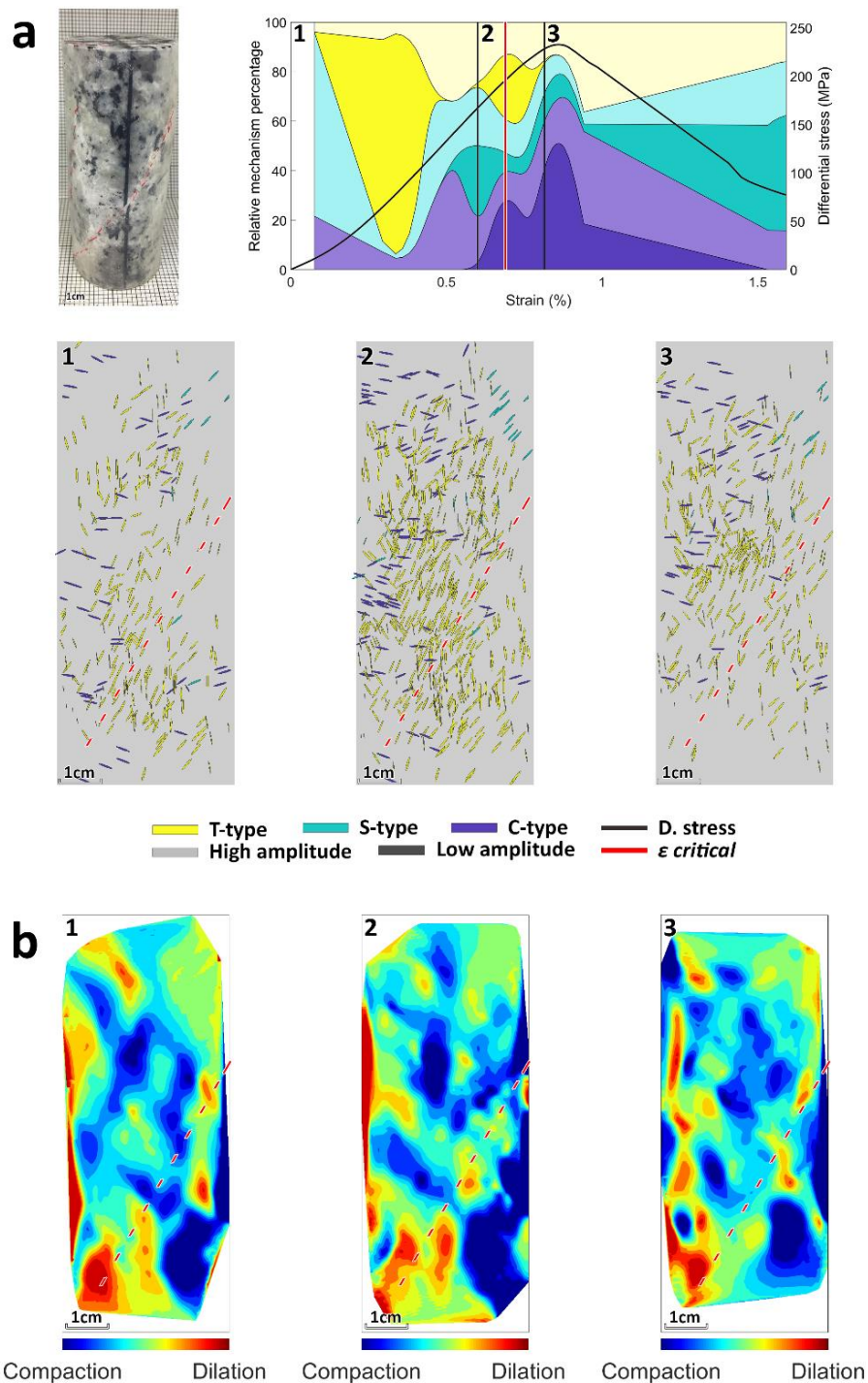


Figure 4.3: a) Post-failure imagery and fault plane in red (top left) for Alzo Granite at 10 MPa. Focal mechanism probabilities (top right) show T-type (yellow), S-type (green) and C-type (blue) events separated by amplitude (lighter for high, darker for low) as strain increases. Fracture mechanism plane distributions (bottom) show the spatial distribution and orientations of events. b) Divergence maps of mechanism slip vectors. Red regions indicate dilatational regions where vector directions are diverging. Blue indicates compactant regions where vector directions are converging. Data are windowed into phases of 1) Fracture Nucleation and Growth, 2) Crack Coalescence and 3) Dynamic Failure.

4.3.1 FRACTURE NUCLEATION AND GROWTH

There is significant uncertainty as to the relative contributions of tensile, shear and closure type mechanisms during the early stages of deformation due to a low amount of data coverage. However, general trends suggest an early dominance of T-type fracturing that is replaced with varying contributions of S-type and C-type events. Nevertheless, the nucleation of new fractures forms the dominant mode of deformation during this stage in both Alzo Granite (AG) and Darley Dale Sandstone (DDS). Furthermore, reactivation of this tensile damage is also likely to occur for preferentially aligned fractures as strain increases.

4.3.1.1 ALZO GRANITE

Early alignment of fracture structure is visible as a rightward dipping region of mixed dilatancy and compaction in the Alzo Granite at 5 MPa (**Figure 4.2b**, Panel 1, red dashed line) and a preferential alignment of T-type fracturing (**Figure 4.2a**, bottom, Panel 1). Dilatational regions to the top right and bottom left highlight off-fault damage not associated to the main structure. At 10 MPa, this phase in the granite is characterised by more low amplitude T-type events (**Figure 4.3a**, top right, Phase 1) that are broadly distributed in the sample (**Figure 4.3a**, bottom, Panel 1). The eventual failure plane is marked as weakly linear region of dilation (**Figure 4.3b**, Panel 1). At 20 MPa (**Figure 4.4a**, bottom, Panel 1) and 40 MPa (**Figure 4.5a**, bottom, Panel 1) clusters of C-type fracturing are observed to form above and below regions of increased dilation (**Figure 4.4b**, Panel 1, red dashed line).

4.3.1.2 DARLEY DALE SANDSTONE

A dominance (**Figure 4.7a**, top right) of poorly aligned tensile fracturing (**Figure 4.7a**, bottom, Panel 1) occurs for the sandstone at 5 MPa (**Figure 4.7a**, top left). Unlike the granite which demonstrated relative continuous regions of dilatancy, deformation in the sandstone is notably “patchier” in its distribution as confining pressure increases. At 10 MPa, T-type and C-type fracturing are broadly distributed throughout the sample (**Figure 4.8a**, bottom, Panel 1). However, at 20 MPa, C-type events align preferentially along the eventual failure plane (**Figure 4.9a**, bottom, Panel 1). At 40 MPa conjugate regions of dilatancy follow the eventual failure planes (**Figure 4.10b**, Panel 1, red dashed line).

Alzo Granite at 20 MPa

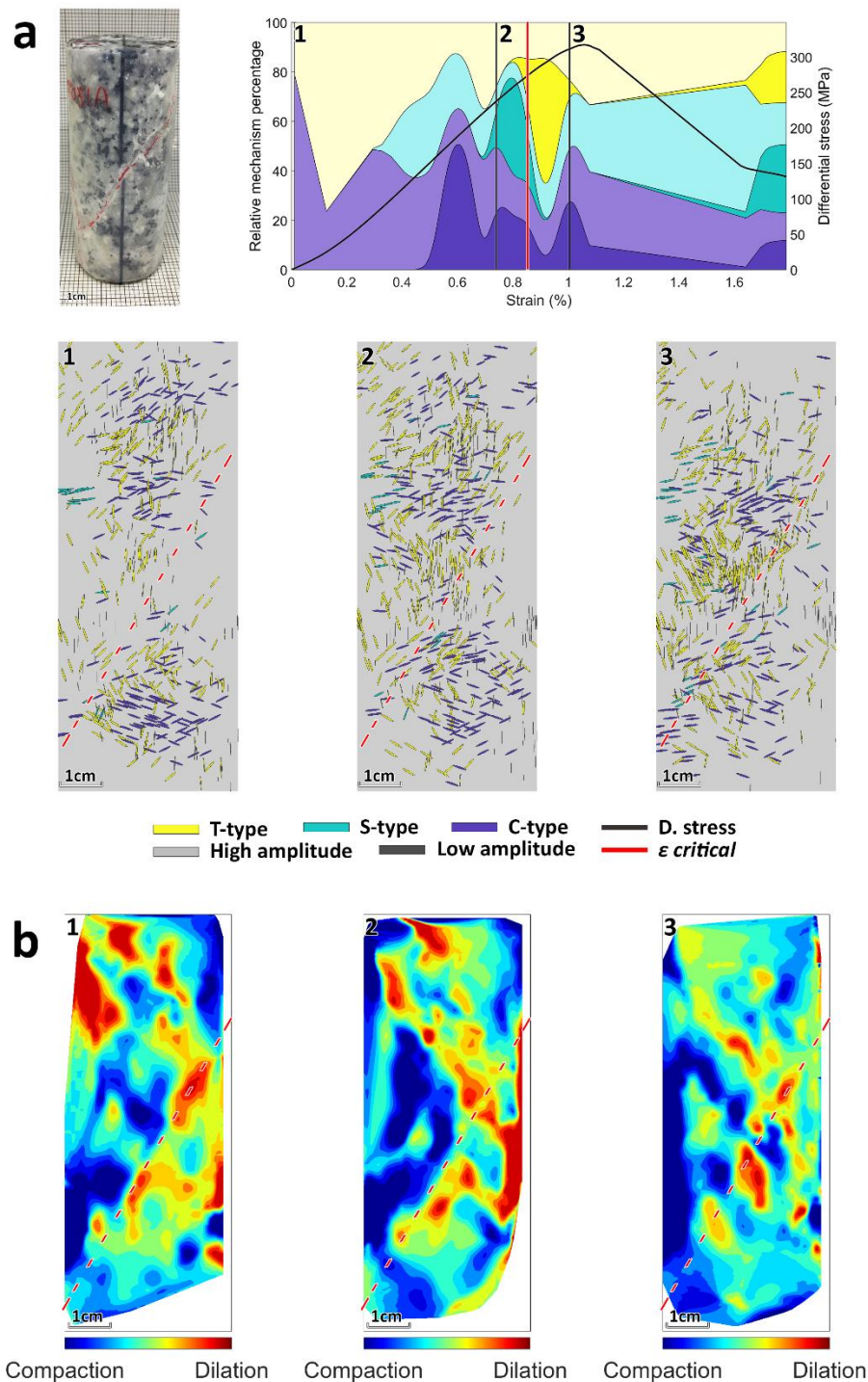


Figure 4.4: a) Post-failure imagery and fault plane in red (top left) for Alzo Granite at 20 MPa. Focal mechanism probabilities (top right) show T-type (yellow), S-type (green) and C-type (blue) events separated by amplitude (lighter for high, darker for low) as strain increases. Fracture mechanism plane distributions (bottom) show the spatial distribution and orientations of events. b) Divergence maps of mechanism slip vectors. Red regions indicate dilatational regions where vector directions are diverging. Blue indicates compactant regions where vector directions are converging. Data are windowed into phases of 1) Fracture Nucleation and Growth, 2) Crack Coalescence and 3) Dynamic Failure.

Alzo Granite at 40 MPa

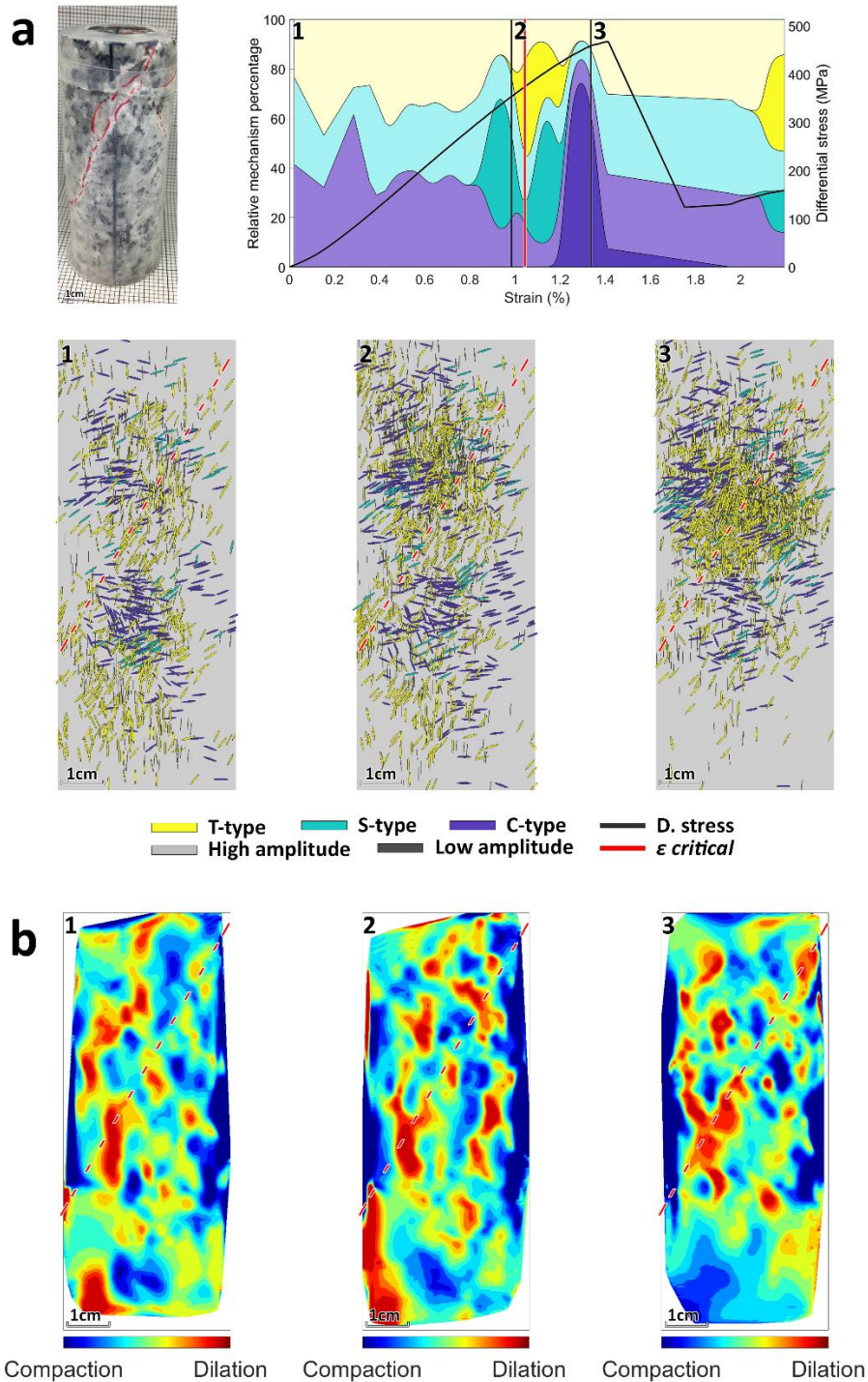


Figure 4.5: a) Post-failure imagery and fault plane in red (top left) for Alzo Granite at 40 MPa. Focal mechanism probabilities (top right) show T-type (yellow), S-type (green) and C-type (blue) events separated by amplitude (lighter for high, darker for low) as strain increases. Fracture mechanism plane distributions (bottom) show the spatial distribution and orientations of events. b) Divergence maps of mechanism slip vectors. Red regions indicate dilatational regions where vector directions are diverging. Blue indicates compactant regions where vector directions are converging. Data are windowed into phases of 1) Fracture Nucleation and Growth, 2) Crack Coalescence and 3) Dynamic Failure.

4.3.2 CRACK COALESCENCE AND DYNAMIC FAILURE

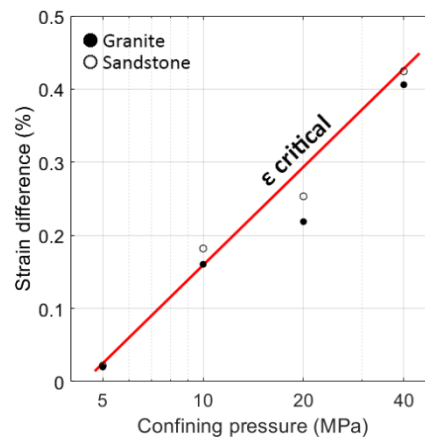


Figure 4.6: The strain difference between $\epsilon_{critical}$ and ultimate compressive strength follows a log-linear relationship with confining pressure.

The onset of this phase is recognised by a softening of the stress-strain curve as samples approach ultimate compressive strength (UCS). Crack coalescence is identified from a small increase in high amplitude C-type events coinciding with a reduction of low amplitude S-type events. This is shortly followed by a burst of low amplitude T-type events. This is marked as $\epsilon_{critical}$ in each of the mechanism probability plots and occurs between 70% and 95% of UCS. The strain difference between $\epsilon_{critical}$ and UCS occurs systematically and shares a log-linear relationship with confining pressure (**Figure 4.6**).

4.3.2.1 ALZO GRANITE

During Crack Coalescence and Dynamic Failure (Phases 2 and 3), regions of dilatancy remain relatively continuous (**Figure 4.2b**). As confining pressure increases, more extensive off-fault fracturing that is not related to the final failure plane occurs (e.g. **Figure 4.4b**, Panel 2). Regardless of confining pressure, S-type events show very little relationship to Dynamic Failure. Rather, these events remain localised to specific regions throughout experimentation (e.g. **Figure 4.3a**, bottom). However, T-type events show clear alignment to the failure direction (**Figure 4.2a**, bottom, Panel 2). At 40 MPa, fracture damage is very broadly distributed throughout the sample with linear regions of dilatancy suggesting the formation of multiple, potential failure planes (**Figure 4.5b**, Panel 2). Dynamic failure is typically represented by a short burst of C-type events followed by high amplitude tensile fracturing (e.g. **Figure 4.3a**, top right, Phase 3). Regions of dilatancy remain from the previous phase of Crack Coalescence but become more localised along the failure plane whilst off-fault regions become more compactant.

Darley Dale Sandstone at 5 MPa

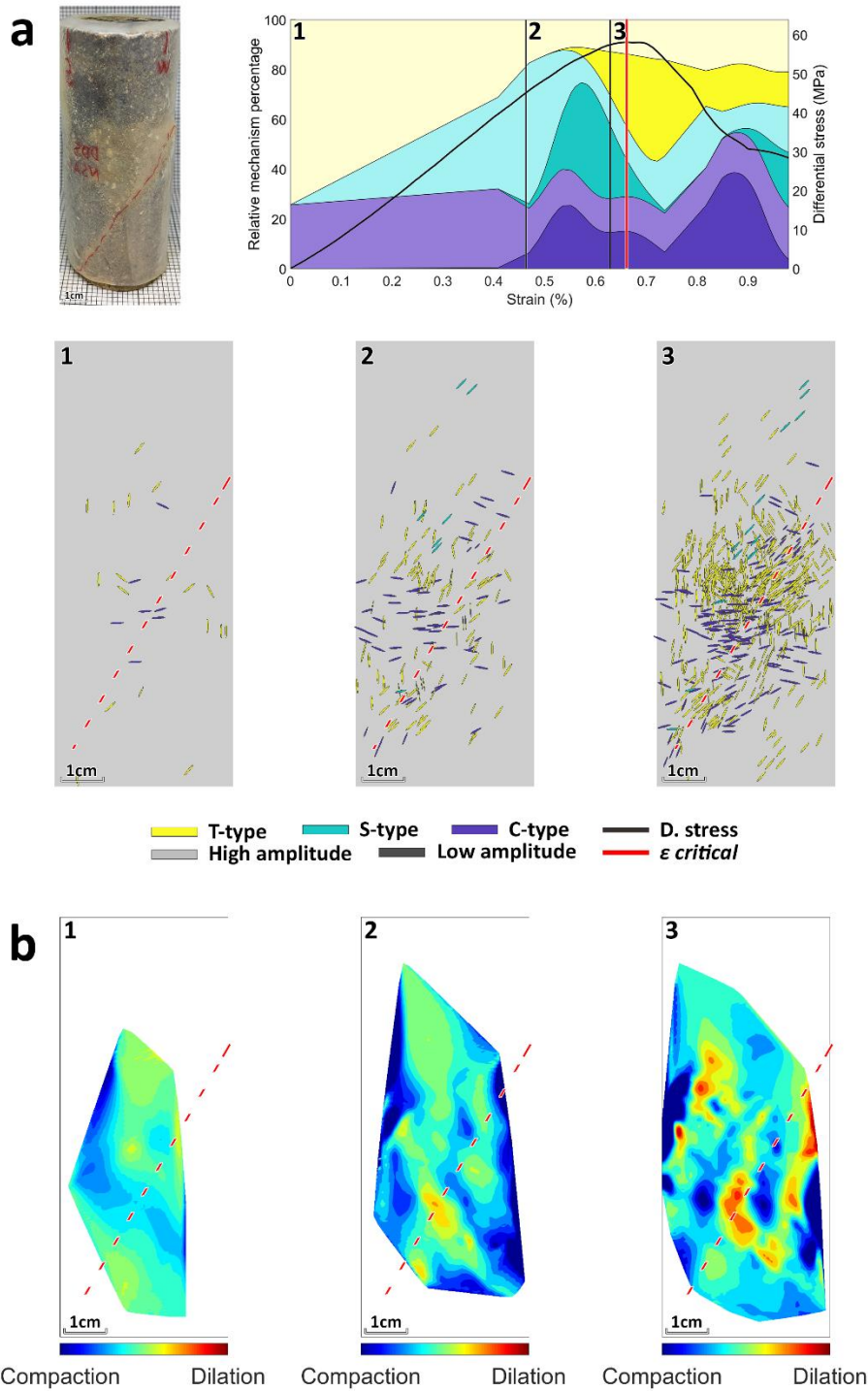


Figure 4.7: a) Post-failure imagery and fault plane in red (top left) for Darley Dale Sandstone at 5 MPa. Focal mechanism probabilities (top right) show T-type (yellow), S-type (green) and C-type (blue) events separated by amplitude (lighter for high, darker for low) as strain increases. Fracture mechanism plane distributions (bottom) show the spatial distribution and orientations of events. b) Divergence maps of mechanism slip vectors. Red regions indicate dilatational regions where vector directions are diverging. Blue indicates compactant regions where vector directions are converging. Data are windowed into phases of 1) Fracture Nucleation and Growth, 2) Crack Coalescence and 3) Dynamic Failure.

Darley Dale Sandstone at 10 MPa

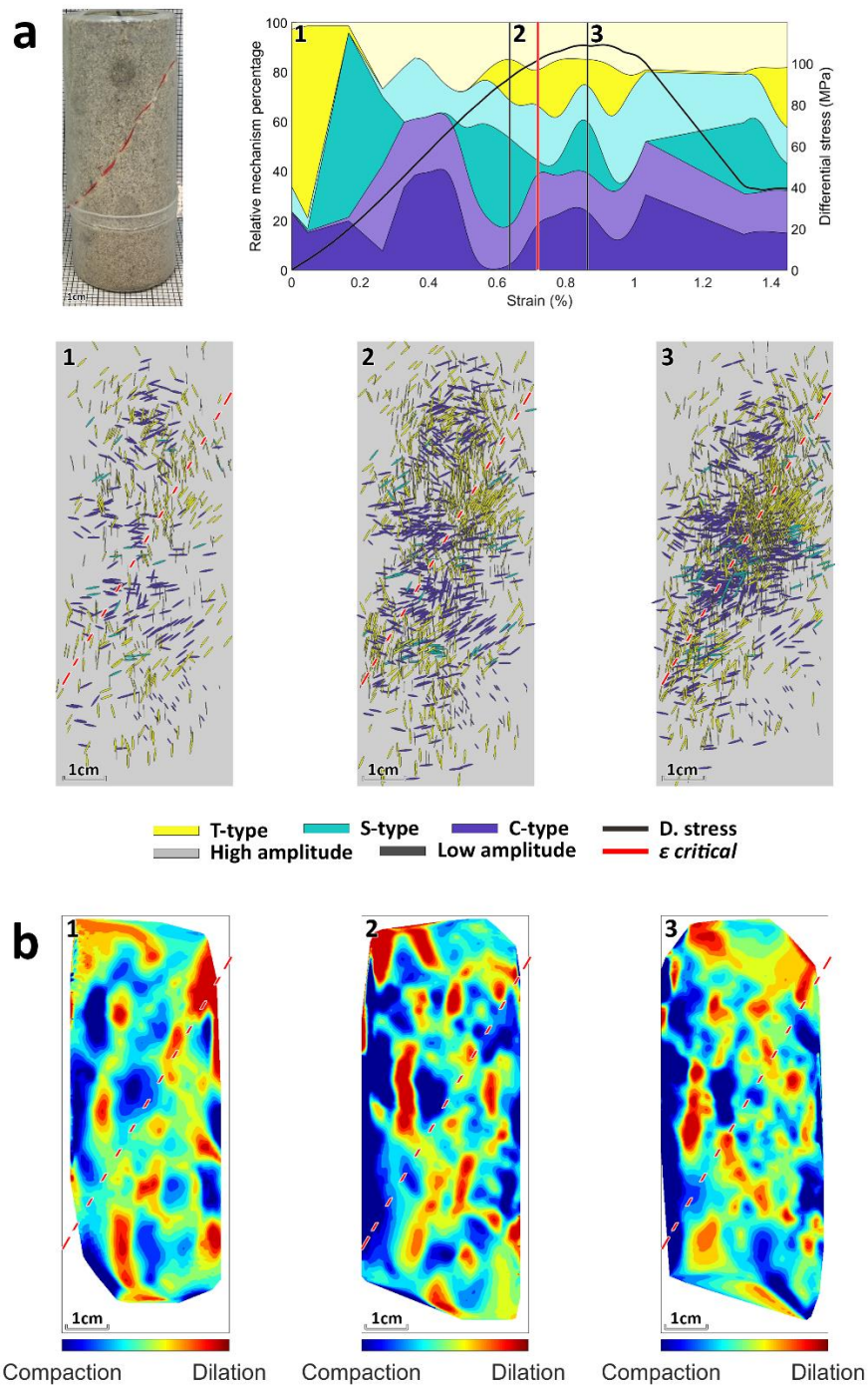


Figure 4.8: a) Post-failure imagery and fault plane in red (top left) for Darley Dale Sandstone at 10 MPa. Focal mechanism probabilities (top right) show T-type (yellow), S-type (green) and C-type (blue) events separated by amplitude (lighter for high, darker for low) as strain increases. Fracture mechanism plane distributions (bottom) show the spatial distribution and orientations of events. b) Divergence maps of mechanism slip vectors. Red regions indicate dilatational regions where vector directions are diverging. Blue indicates compactant regions where vector directions are converging. Data are windowed into phases of 1) Fracture Nucleation and Growth, 2) Crack Coalescence and 3) Dynamic Failure.

4.3.2.2 DARLEY DALE SANDSTONE

C-type events occur as a pre-cursor to the eventual failure plane as either cross-fault structure (e.g. **Figure 4.7a**, bottom, Panel 2) or as along fault compaction (**Figure 4.8a**, bottom, Panel 2). Preferential localisation of T-type fracturing also occurs along fault zone structure, however events are not orientated in any particular direction. At 20 MPa, during Crack Coalescence multiple conjugate structures can be seen forming (**Figure 4.8b**, Panel 2), although compaction along their length leads to preferential selection of a single failure plane (**Figure 4.8b**, Panel 3). At 40 MPa, conjugate structure that was established during Fracture Growth remains constant through the later phases (**Figure 4.9b**, Panel 3) with extensive off-fault fracturing occurring throughout the sample (**Figure 4.9a**, Panel 3).

Darley Dale Sandstone at 20 MPa

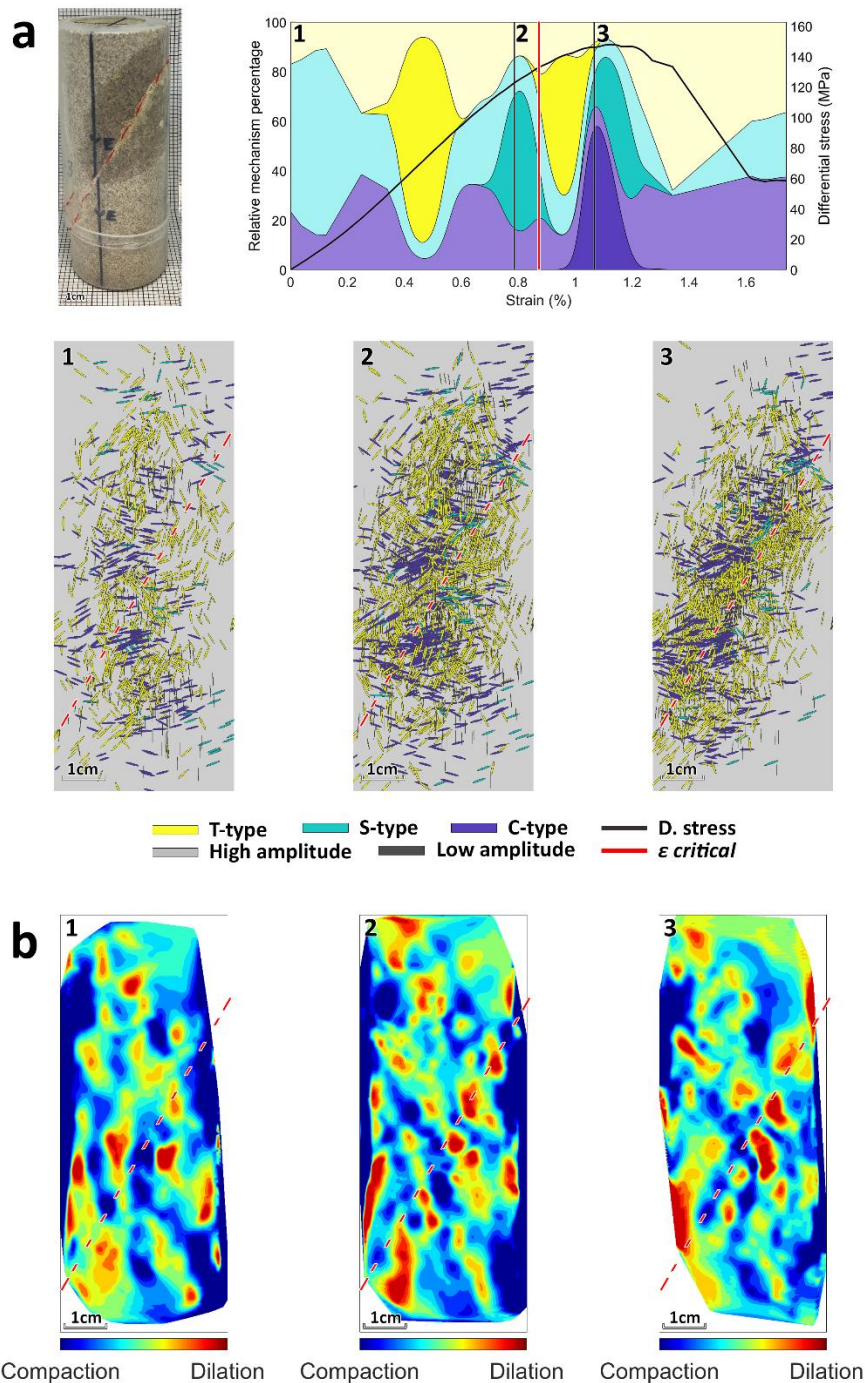


Figure 4.9: a) Post-failure imagery and fault plane in red (top left) for Darley Dale Sandstone at 20 MPa. Focal mechanism probabilities (top right) show T-type (yellow), S-type (green) and C-type (blue) events separated by amplitude (lighter for high, darker for low) as strain increases. Fracture mechanism plane distributions (bottom) show the spatial distribution and orientations of events. b) Divergence maps of mechanism slip vectors. Red regions indicate dilatational regions where vector directions are diverging. Blue indicates compactant regions where vector directions are converging. Data are windowed into phases of 1) Fracture Nucleation and Growth, 2) Crack Coalescence and 3) Dynamic Failure.

Darley Dale Sandstone at 40 MPa

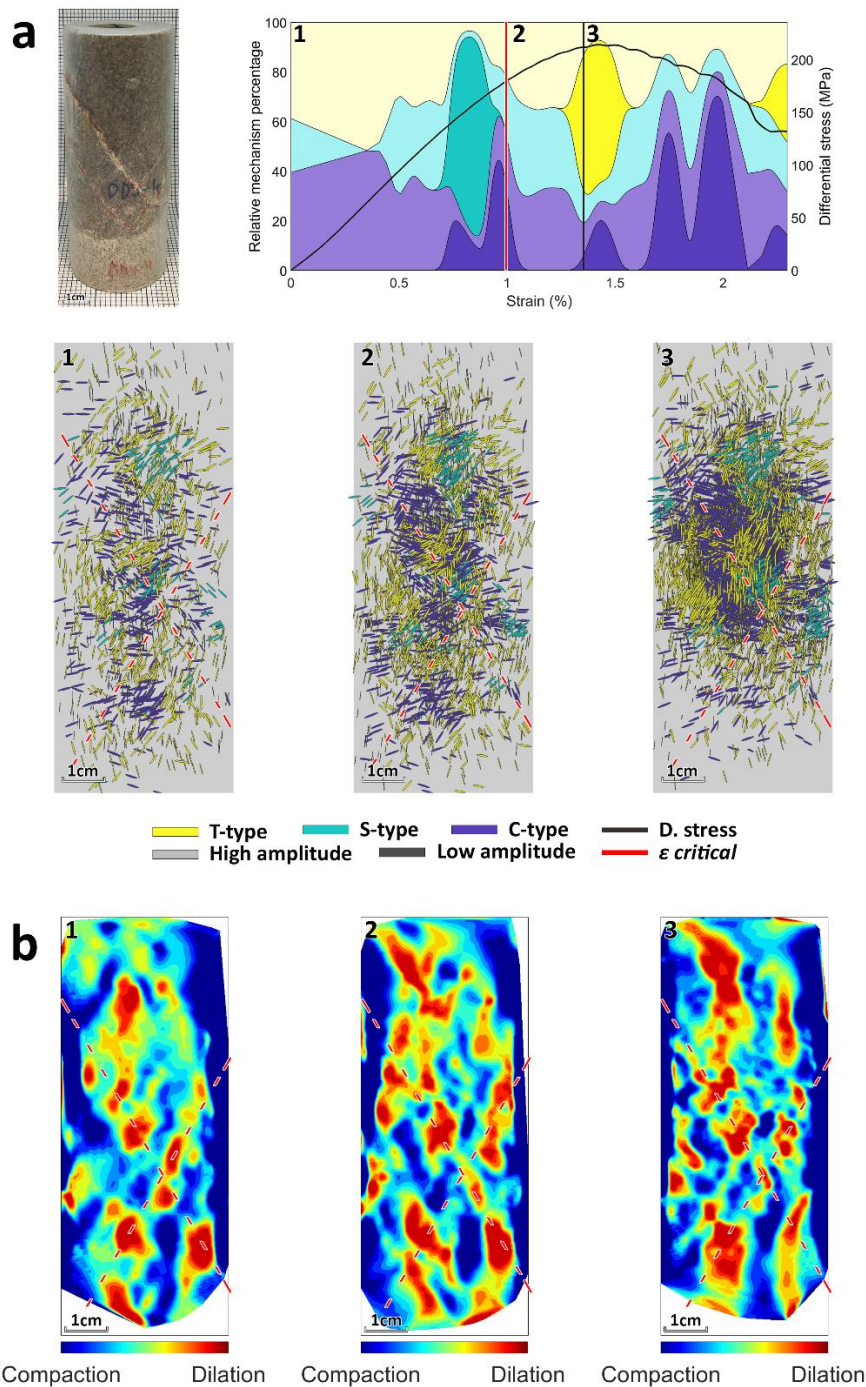


Figure 4.10: a) Post-failure imagery and fault plane in red (top left) for Darley Dale Sandstone at 40 MPa. Focal mechanism probabilities (top right) show T-type (yellow), S-type (green) and C-type (blue) events separated by amplitude (lighter for high, darker for low) as strain increases. Fracture mechanism plane distributions (bottom) show the spatial distribution and orientations of events. b) Divergence maps of mechanism slip vectors. Red regions indicate dilatational regions where vector directions are diverging. Blue indicates compactant regions where vector directions are converging. Data are windowed into phases of 1) Fracture Nucleation and Growth, 2) Crack Coalescence and 3) Dynamic Failure.

4.3.3 MECHANISM ORIENTATIONS

Table 4.1: Counts of mechanism orientations

	Confining Pressure (MPa)	Parallel to Shear			Perpendicular to Shear		
		C-Type	S-Type	T-Type	C-Type	S-Type	T-type
AG	5	325	64	1103	252	11	489
	10	109	45	705	132	8	390
	20	387	84	847	245	17	451
	40	813	283	2353	293	12	1113
DDS	5	198	22	440	58	0	151
	10	822	161	1465	653	11	1202
	20	822	137	2493	620	112	1671
	40	1825	647	3879	1633	125	1900

To investigate the effect of confining pressure on fracture orientation, slip planes are estimated directly from solved focal mechanisms (Error! Reference source not found.). Individual counts for each plot point are provided in

Mechanism Orientations

Table 4.1. Azimuthal directions are normalised according to the modal direction of S-type events for each experiment in order to separate out events which dip parallel to the macroscopic failure plane and those that dip perpendicular. Circular points indicate the average of each of the mechanism types at the different confining pressures. Error bars are calculated as the standard error ($SE = \sigma/\sqrt{n}$) and represent the spread of the data. Lines of best fit are calculated using weighted linear least squares where the weighting is set as the inverse standard error.

A steepening of S-type events and a shallowing of T-type with increasing confining pressure represent a switch from axial splitting to fault plane localisation in DDS (Error! Reference source not found.). However, AG demonstrates the opposite trend where S-type become shallower and T-type steepen. Furthermore, there is a steepening of C-type events in the perpendicular direction. It is likely that these rotations occur as a result of the same transitional switch present in DDS. However, because the increased strength of AG will inhibit the propagation of S-type events, these events will occur as C-type, with fracturing occurring perpendicular to the direction of shear. This shear inhibition will further reflect

on shear parallel T-type events, raising the average dip as more events become localised along the failure plane at higher confining pressures.

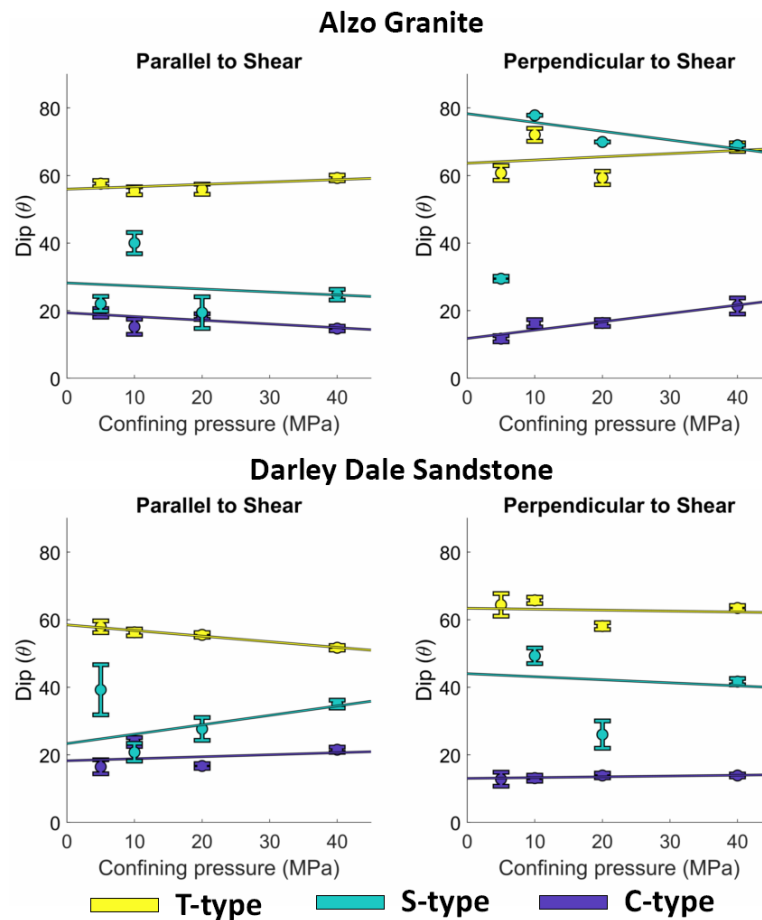


Figure 4.11: Average mechanism orientations are plotted against confining pressure for events dipping parallel or perpendicular to the sample failure plane. Error bars are defined as the standard error and represent the range of data from which the average is calculated.

4.4 DISCUSSION

4.4.1 COHESIVE VS. GRANULAR DRIVEN FAILURE

During compressive loading, fracture growth is driven primarily by the presence of naturally occurring defects in a material. These flaws typically occur as grain boundaries, pores and pre-existing microfractures (Katcoff and Graham-Brady, 2014). The size, shape and distribution of these impurities have long been understood to play a fundamental role in the development of a fault as it is from these that new fractures are enucleated. Two end-members are often used to describe the initial microstructure of a rock (Baud et al., 2014); 1) a cohesive model where intergranular boundaries do not play a large role, instead fracture

initiation is largely driven by stresses at existing flaws and 2) a granular model where the bonds at grain contacts are readily ruptured by stress allowing neighbouring grains to slip and rotate relative to each other.

For the materials analysed here, Alzo Granite (AG) represents the former and Darley Dale Sandstone (DDS) the latter. At 5 MPa (**Figure 4.2**), Alzo Granite demonstrates cohesive structure from the onset with a larger number of diffusely located fracturing events compared to DDS (**Figure 4.7**). As deformation increases dilatancy is observed to localise to a fault plane for both rock types, however, off-fault damage is more prevalent in AG. Early tensile activity in AG is highlighted by a burst of low amplitude T-type events that is only present for 5 and 10 MPa between 0.3 and 0.5% strain. It is likely that this is replaced with high amplitude fracturing at the higher pressures owing to increased rock strength with increasing confinement (Li et al., 1999). Conversely, at 10 MPa DDS demonstrates an earlier dominance of S-type fracturing that switches to compaction at this time (**Figure 4.10**). At 20 MPa, there is a similar burst of low amplitude T-type fracturing to AG, however this is not present at 40 MPa.

These early differences in the fracturing process are related to the granular nature of DDS, where the pre-existing porosity acts to accommodate strain (van der Baan et al., 2016) and is shown by the patchy distribution of dilatant regions compared to the more continuous structure present in AG. It is not until 20 MPa that fault structure becomes evident in DDS with the divergence map approach. Interestingly, this is not demonstrated by the actual distribution of fracturing events within the samples, instead, DDS shows clear localisation of AE towards a fault zone whilst AG remains relatively diffuse regardless of confining pressure. Although, the latter observation may be related to a larger damage zone in AG that is not fully represented by the physical dimensions of the samples analysed here (Lyakhovsky et al., 2015).

In any case, microstructural analysis (Hallbauer et al., 1973; Menéndez et al., 1996; T.-F. Wong, 1982) and acoustic emission studies (Lockner et al., 1992; Zang et al., 1996) have demonstrated that the faulting process involves a multiplicity of flaws (e.g. cracks, pores) that interact along regions that are preferentially aligned to each other (Baud et al., 2014). For equant pores, tensile fractures nucleate at the pore boundary and propagate parallel to the maximum direction of compressive stress. As they propagate further, the bonding at grain contacts are ruptured in the sandstone, whilst in the granite these fractures

are likely to interact leading to a pseudo-granular structure as fracturing becomes more diffuse (e.g. **Figure 4.5b**).

In DDS prior to crack coalescence, c-type fracturing is observed to localise along the eventual fault plane, signifying an important precursor to dynamic failure of the sample. It is likely that these events represent reactivation of pre-existing damage or flaws through pore-collapse or fracture closure due to the lower stresses required compared to tensile initiation. However, as the amount of slip is limited in these events, their ability to accommodate strain is low and so are shortly followed by shearing (DDS) and tensile (AG) damage as the flaw ruptures. It is likely that extensive grain crushing/communion will establish along a single failure plane at this time (e.g. Zang et al., 1996).

Several models seek to assess the distribution of this damage as a fracture grows through a tensile process zone at its tip and a shear-compaction wake along its length (Lei et al., 2000). The results presented here highlight that this model of fracture extension is occurring at multiple sites at once (e.g. **Figure 4.4b**, Panel 2), however, there is an overall dominance of a single mechanism throughout the entire sample at a particular time (**Figure 4.4a**, top right). This observation and the distribution of S-type events highlight significant interaction between the different sites where if one site is too cohesive to allow for shear, another weaker site will accommodate. This leads to repeated activation of previously sheared regions that are not necessarily located along a developing fault plane (**Figure 4.10a**, bottom, Panel 3). Although the method presented here does not consider the shearing components of individual T-type or S-type events, it demonstrates that the fault development process is more dependent on the interaction between neighbouring dilatational and compactant regions rather than shearing along a discrete plane.

4.4.2 FORECASTING DYNAMIC FAILURE

Following each fracture growth cycle there is a discrete burst of low amplitude T-type events that accommodates the applied load before the system stabilises and a new cycle begins. Although all the events involved may not be low amplitude, this study proposes that they represent a phase of fracture extension and the connection of preferentially aligned patches of damage. In the results presented here, the final cycle is represented by the parameter $\epsilon_{critical}$. The timing of this follows a log-linear relationship with confining pressure, highlighting its potential for use as a forecaster of dynamic failure.

The length of ϵ *critical* itself will be dependent on several additional factors. The strain rate controls the speed at which micro-fracturing can occur, where higher values will lead to an increased shortening of ϵ *critical*. When strain rate and confining pressure are held constant, it is likely that the materials cohesiveness prior to failure has the main influence. For example, AG is consistently shown in **Figure 4.6** to predict having higher values of ϵ *critical* compared to DDS due to a higher cohesiveness at the same pressure. Nonetheless, AG also demonstrates a larger standard deviation from the line of best fit suggesting a further dependency on the distribution of induced fracture damage. As this is related to the initial distribution of flaws, this aspect is difficult to quantify.

4.4.3 FAILURE PATTERNS

Two end members of brittle failure pattern are identified (**Figure 4.12**) and follow the traditional models of axial splitting and fault plane localisation as confining pressure increases. A transitional phase at 20 MPa in DDS indicates that the switch from one to the other takes place during fracture growth, however as confining pressure is increased (e.g. DDS at 40 MPa), fault plane localisation begins earlier. It is likely that this process is also occurring in AG but as failure is driven by the interaction of cracks rather than pores it is far less visible, and due to an increased sample cohesiveness, occurs at higher pressures than those analysed here.

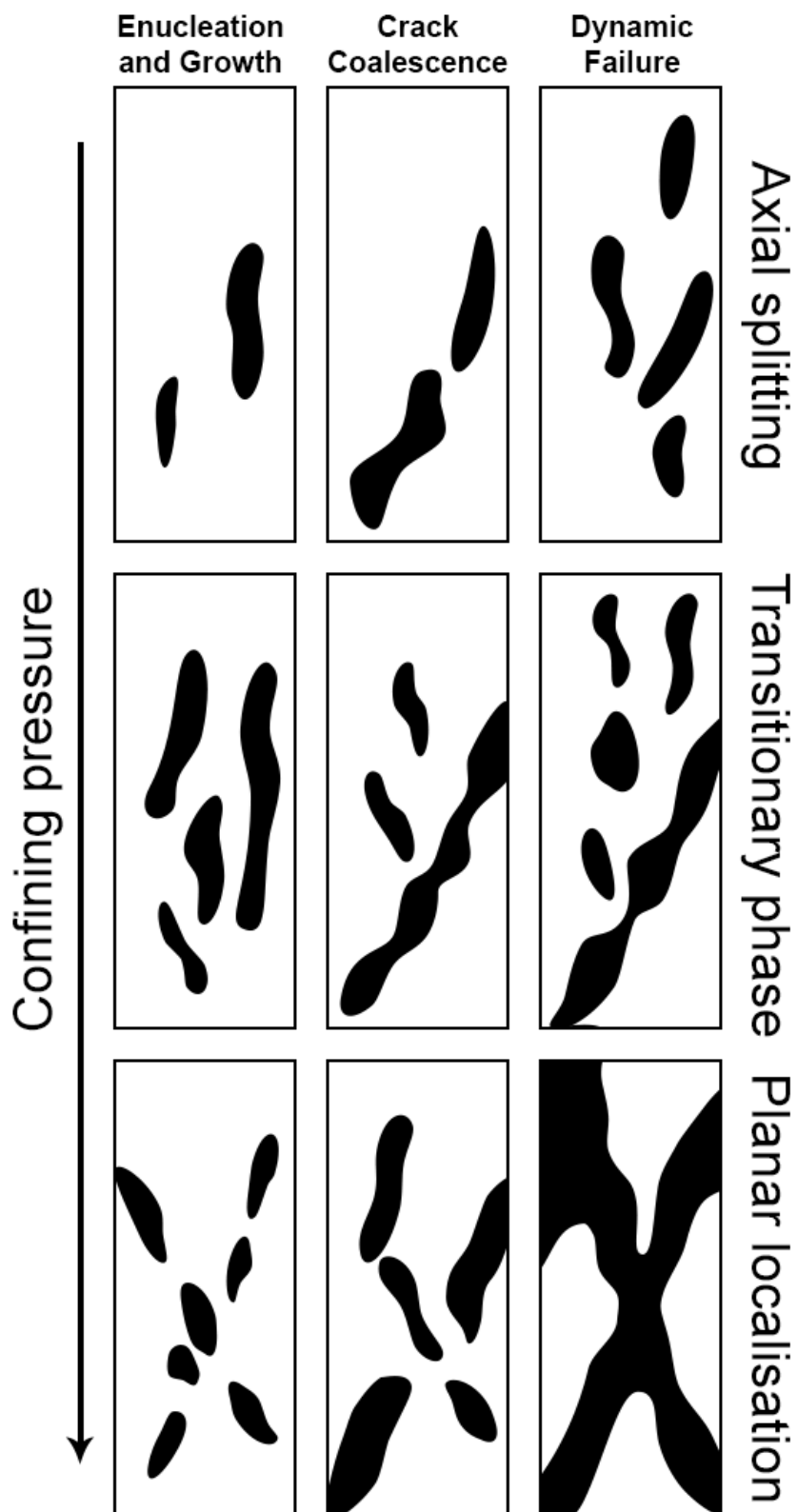


Figure 4.12: Simplified brittle failure patterns. Dilatant regions (black) highlight the changing distribution of deformation structure as confining pressure increases for the different deformation stages. A transitional phase between axial splitting is identified where zones of deformation form into planar structure during crack coalescence.

4.5 CONCLUSIONS

This study presents the results of high-resolution analysis of focal mechanism solutions derived from laboratory acoustic emission data. Samples of Alzo Granite and Darley Dale Sandstone were systematically deformed under conventional triaxial conditions until dynamic failure occurred at confining pressures of 5, 10, 20 and 40 MPa. Mechanism were solved using a least squares minimisation of the 3D first-motion polarity focal sphere to characterise AE as tensile (T-type), shearing (S-type) and compaction/collapsing (C-type). Results are biased towards T-type or C-type, with pure double-couple fracturing represented by a relatively small percentage of S-type fracturing.

Divergence maps of mechanism slip vectors reveal a dependency on the distribution of dilatational and compactant regions for fault zone development, where the distribution itself is dependent on the relative cohesiveness of the material under study and the confining pressure. The more cohesive AG follows a model of crack-driven failure, with previously failed regions being repeatedly activated as deformation progresses as shown through consistent dilatational structures present throughout the tests. Conversely, DDS initiates with pore driven failure with multiple, unrelated fractures developing. However, once damage reaches a critical threshold, it begins to localise in a similar way to AG. A key difference in DDS, however, is the localisation of C-type events along the eventual fault plane prior to crack coalescence. This is an important precursor to dynamic failure that does not appear to occur in AG.

Overall, however, it is T-type fracturing which dominates crack coalescence. Low amplitude tensile events, that may represent an end member to larger scale processes, act as connectors of regions of damage that facilitate macroscopic weakening. The final phase of this occurs systematically and shares a log-linear relationship with confining pressure. The parameter $\epsilon_{critical}$, defined as the difference in strain between the last onset of low amplitude T-type fracturing and ultimate compressive strength, demonstrates an increase with confining pressure that is dependent on the cohesiveness of the sample prior to dynamic failure.

5 PEAK DELAY AND PATH EFFECTS

5.1 INTRODUCTION

As a seismic wave propagates through a medium, heterogeneities (e.g., high-aspect ratio cracks) cause velocity variations (Benson et al., 2007) resulting in the broadening of seismic envelopes. The time delay between the onset of the wave and the maximum amplitude of the seismic energy (so-called Peak Delay) is rapidly becoming a useful parameter to investigate the distribution of heterogeneities in the lithosphere (Calvet et al., 2013; Napolitano et al., 2019). An increase in Peak Delay is generally associated with increasing forward-scattering effects resulting from the interaction with geologically-complex regions (Abubakirov and Gusev, 1990; Calvet et al., 2013; Sato, 1989; De Siena et al., 2016; Takahashi et al., 2009, 2007) and may be described by the Markov approximation of the parabolic wave equation (Saito, 2002; Sato, 1989; Sato and Fehler, 1998). The mentioned field studies interpreted these structures as strongly fractured media presenting large-scale fracture networks that align with the regional tectonic fabric. To better understand how these networks influence geophysical measurements, laboratory rock-physics experiments are now providing new simulations of rock deformation linked to Acoustic Emission (AE), the laboratory proxy for field scale seismicity, under known and controlled conditions (e.g. pressure, temperature, strain rate). Here, the propagation of energy can be simulated in fractured media analogous to the subsurface, either artificially pre-fabricated or dynamically created in triaxial deformation cells (Harnett et al., 2018). AE waveforms are highly sensitive to variations in sample structures, particularly P-wave and S-wave elastic velocity and velocity anisotropy once the density of fractures increases (Bonner, 1974; Hadley, 1976; Lockner et al., 1977; Nur, 1971; Schubnel et al., 2003). AE emissions can thus help us establish a holistic link between the geological structures, their geophysical attributes, and the model outputs of the lithosphere derived from peak-delay mapping.

Considering Peak Delay as a path effect with little input from the source or the receiver, Takahashi et al. (2009, 2007) and Tripathi et al. (2010) developed a simple tomographic method to map this heterogeneity in Japan. They observed a hypocentral, frequency, and spatial correlation of high peak-delays with the distribution of quaternary age volcanoes. Calvet et al. (2013) and Borleanu et al. (2017) further observed that high Peak Delay measurements can easily be corrupted by near-source and near-receiver

heterogeneities, as confirmed when using active data (Zieger et al., 2016) and by finite difference simulations (Takemura et al., 2015) respectively. De Siena et al. (2016) observed significant frequency-dependent peak-delay variations at Mount St. Helens volcano that cannot be explained by small velocity fluctuations. Spatial Peak Delay variations at low frequency (3 Hz) were linked to the lateral impedance contrasts associated to the debris flow of the 1980 eruption. Napolitano et al. (2019) demonstrate that peak-delays (in conjunction with coda attenuation mapping) can reconstruct the complex space-frequency evolution of seismically active, fluid-filled fault systems. The authors observe that peak-delay variations can track shorter-scale cross faulting with increasing frequency, allowing them to discriminate faults affected by historical activity from those where recent earthquakes nucleated.

While the relationship between geological structure and an increase in Peak Delay is evident at the field scale in the far field, there is no direct experimental calibration linking Peak Delays with the structures that influence them in the near field, or at laboratory scale. The Markov approximation is only valid in the far field for a point source when assuming that the wavelength λ is much shorter than the correlation distance (a) of heterogeneities. In near-source studies, the effect of the propagation medium has often been disregarded or roughly corrected (Ripperger et al., 2008). Still, the role of statistical fluctuations in increasing the duration and complexity of ground motion has been recently recognized already at few kilometres away from the source, where source effects were generally thought to dominate (Imperator and Mai, 2015).

In addition to a structural sensitivity, active surveying across synthetic media suggests a strong geometry-dependence of scattering parameters on the relative position of geological structure and the AE acquisition array. Rao and Wang (2009) apply a frequency-domain procedure to calculate attenuation parameters in differently orientated fractured media. Numerical studies identify a dependence of scattering attenuation parameters on frequency where the inverse quality factor is linearly dependent on fracture density (Fang et al., 2013; Vlastos et al., 2007) When fracture and shear zone lengths are less or equal to one-half wavelength, they act as point scatterers. However, as the size approaches one wavelength, attenuation becomes strongly dependent on fracture orientation. Indeed, P-wave attenuation systematically increases with fracture thickness for rays travelling perpendicular to a shear zone (Ekanem et al., 2014).

In this chapter, I examine the multiple forward scattering effects of fractured samples of Westerly Granite and Darley Dale Sandstone as analogues for crustal-scale interfaces. Samples were deformed in conditions representative of the shallow subsurface to produce a shear zone. I applied the peak-delay methodology of Takahashi, et al. (2007) to map the heterogeneity in the samples using AE data. Still, modelling the seismic wavefield in anisotropic and dissipative samples (cm dimension) at frequencies in the range of 50-1000 KHz requires an appropriate characterization of the AE sources. As the Markov approximation is unfulfilled at these frequencies, the imaging is thus paired by models of wave propagation in anisotropic and dissipative media for which the propagation distance is of the order of a few wavelengths (Treeby and Cox, 2010).

Results provide new evidence for scale-specific and geometry-dependent effects that corrupt the waveform in a predictable and deterministic manner: thus, it becomes possible to link a simple peak-delay analysis to a more complex pre-existing shear zone structure. Fracture structure is reconstructed with high detail across a band of frequencies when cross-fracturing is sufficiently dense. These results show that peak-delay mapping can become a valid marker of fracture networks and discrete heterogeneities at laboratory scale and in the near field.

5.2 DATA AND METHOD

5.2.1 PEAK DELAY

The measurement of the Peak Delay time (t_p) follows the approach of Takahashi et al. (2007) where Peak Delay times are measured on the S-phase. Due to limitations of the acquisition equipment used here, (the sensors do not differentiate between P and S waves), the automated strategy applied in this thesis picks P-wave arrivals (**chapter 3**). However, De Siena et al. (2016) demonstrated that, at the field scale, relative lateral variations of $\frac{V_p}{V_s}$ higher than 2 are necessary to explain Peak Delay time fluctuations of the order of those measured at different t_p . For dry sandstone and granite samples velocity ratios do not exceed this threshold (Pickett, 1963; Stanchits et al., 2006), thus suggesting the use of the P-wave here.

During testing, additional complexity was noted in the coda of waveforms where reflected arrivals from the sides of the samples would arrive. To address this, the signals

were cropped between T and $3 \cdot T$ (where T = arrival time). The cropped signals are filtered (6th order Butterworth Bandpass) in four frequency bands, i.e. 50-100, 100-200, 200-400 and 400-800 KHz and the upper RMS envelope calculated to fully encompass the available data and highlight frequency dependent trends. Envelopes are weakly smoothed with a moving time window of 0.001ms to minimise strong scattering effects whilst avoiding smoothing of the peak arrival, which can be easily lost in low amplitude data. The maximum of the envelope is identified as the peak arrival and t_p is measured in microseconds as the time difference between the onset of the waveform and this value. An error for this measurement is defined as the time range for signal envelope values that lie above 90% of the peak value (**Figure 5.1**). Only waveforms that have an error of less than 0.04ms for all frequency bands are selected for further study.

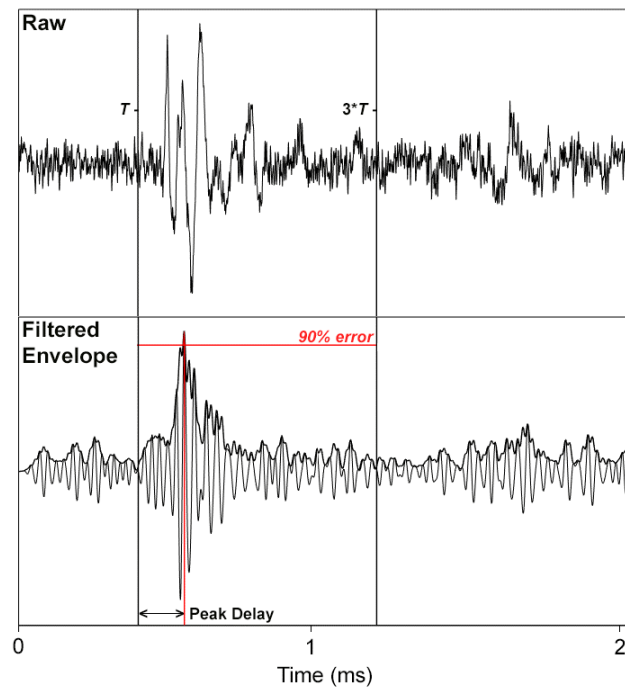


Figure 5.1: Peak Delay is defined as the time between the onset of energy and the maximum energy arrival. The raw AE waveform (above) is filtered within a specified frequency bands and the maximum is identified from the RMS envelope calculated. As there is significant overlap of energy (e.g. direct, transmitted and reflected arrivals), the maximum is selected between the onset, T , and $3 \cdot T$. The range of time for the signal to be above 90% of the signal maximum is defined as the error (red line).

Being cumulative the Peak Delay time cannot be reduced even if along the raypath there are weak heterogeneities (Takahashi, et al., 2007). Therefore, the high values of Peak Delay at the longer distances are simply due to more exposure to heterogeneity along the raypath when measured at the laboratory scale. As a result, Peak Delay is hereafter

considered as a relative value $\Delta \log(t_p)$ around the average. Where a small $\Delta \log t_p$ marks the absence of strong heterogeneity along the ray-path, the opposite is true for high values:

$$\Delta \log(t_p) = \log(t_p) - \frac{1}{n} \sum_{i=1}^n \log(t_{p_i}). \quad (5.1)$$

5.2.2 SOURCE LOCATIONS AND PEAK DELAY MAPPING

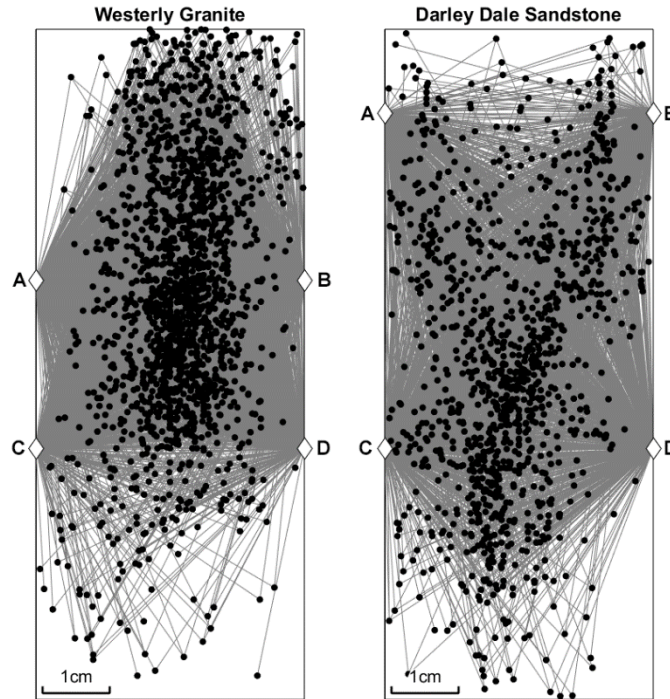


Figure 5.2: Source locations (black dots), PZT receivers (diamonds) and grey lines (raypaths) used in the Peak Delay tomography analysis.

To simplify the analysis, arrivals to PZTs that do not lie orthogonal to the observed failure plane are removed and AE source locations flattened to this orthogonal plane. Subsequently, 5222 waveforms (2320 AE) and 3144 waveforms (1391 AE) were used in the peak-delay study for the granite and sandstone (**Figure 2.9, page 24**), respectively. Epicentres, PZTs and raypaths used in the tomography (assumed here to be straight) are detailed in **Figure 5.2** by black dots, diamonds and grey lines, respectively.

In analogy with field-scale mapping, source-receiver pathways are assigned their associated peak-delay measurement. The medium is discretised into model blocks of $0.01 \times 0.01 \text{cm}$ in size and each block is assigned the average $\Delta \log t_p$ of all the raypaths that cross it. To speed up the procedure and minimise anomalous variations in regions of low

ray-path coverage, only blocks that were crossed by a minimum of 5 rays are solved. Peak-delay values are smoothed at each block by averaging each block value with blocks within 1cm distance.

5.2.3 2D MODELLING OF ANISOTROPY VARIATIONS

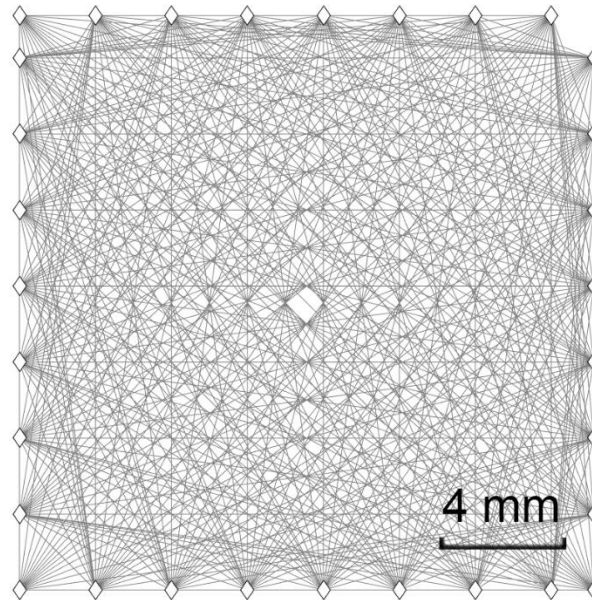


Figure 5.3: Source and receiver array (both represented as diamonds) used in the numerical modelling. Grey lines indicate raypaths.

The MATLAB toolbox K-Wave (Treeby & Cox, 2010) allows for the modelling of elastic wave propagation and accounts for nonlinearity, acoustic heterogeneities and power-law absorption of energy at a scale identical to laboratory conditions. As fractures are developing from the start of the experiment, it is suitable to examine the effects of a single inclusion on Peak delay at low and high frequencies. For simplicity the inclusion is modelled as a stiff central region of lower velocity and density characteristics compared to the rest of the sample.

To understand if (and at which frequencies) Peak Delay is affected by an inclusion, the model is setup as a sample of $x = 20$ mm by $z = 20$ mm with a grid step of 0.1 mm. The lowest/highest velocities are assumed as 3.5 km/s and 5.5 km/s. To ensure sufficient acoustic impedance between the inclusion and host medium densities are assumed as 1.8×10^3 kg/m³ and 2.3×10^3 kg/m³. An isotropic medium is assumed at the start of the laboratory experiment, thus the scattering effects of the host medium is disregarded. Synthetic P-wave energy pulses are then propagated across the medium from an array of receivers around

inclusion (source-receiver paths are detailed in **Figure 5.3**). The source itself is defined as a circular monopole source 0.1 mm in diameter and an initial pressure distribution of 5 Pa.

To simulate fracture structure of various shapes and at different stages of development, two inclusion models are analysed. The first is a 4 mm circular pore at different stages of coalescence. Here, equidistant structure of equal acoustic impedance within the pore region becomes increasingly sparse. The second study then investigates the impact of aspect ratio on Peak Delay tomography where a fully coalesced pore is shortened along the z axis.

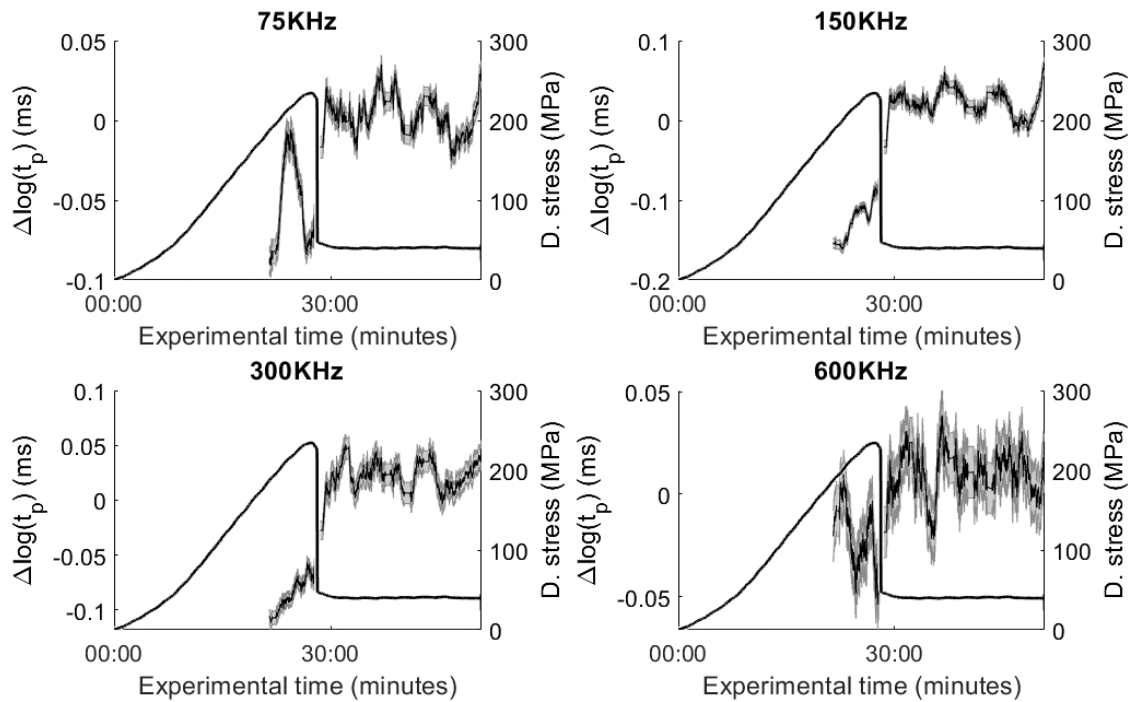
The steps of the simulation are at $1e^{-2}$ milliseconds and the simulation is restricted to 3 microseconds. To maintain the comparison with the laboratory study, Peak Delay values are calculated for the simulated waveforms using the method described in **section 5.2.1** and **section 5.2.2**. Thus, the wavelengths for the simulations are: 47 mm (75 KHz), 23 mm (150 KHz), 12 mm (300 KHz) and 6 mm (600 KHz). In the first two cases, no more than a wavelength will propagate into the medium, whilst only a couple will occur for the higher frequencies. In the real experiment hypocentral distances are of different lengths and heterogeneity may occur at any stage of the raypath, however, as the interest of the modelling is in the variations of Peak Delay when an inclusion is fully sampled from all directions, this setup is a useful indicator of what may happen in the laboratory. Recent research further questions the development of fractures just along strike, showing that failure is also the consequence of the dynamic coupling with diffuse off-fault cracking (Renard et al., 2019). This setup allows the modelling of heterogeneity that is not necessarily related to the development of the shear zone but possibly due to the coalescence of any porous structure.

5.3 RESULTS

5.3.1 TIME DEPENDENCIES OF PEAK DELAY

An important distinction of AE data obtained in the laboratory are the timescales over which deformation occurs. Unlike seismic data, which typically sample structures that may change over a few decades (Napolitano et al., 2019), the nature of the laboratory setup results in extreme variations that can occur over *seconds*. This is shown to have a clear and noticeable effect on the AE waveform in **Figure 5.4**.

Westerly Granite



Darley Dale Sandstone

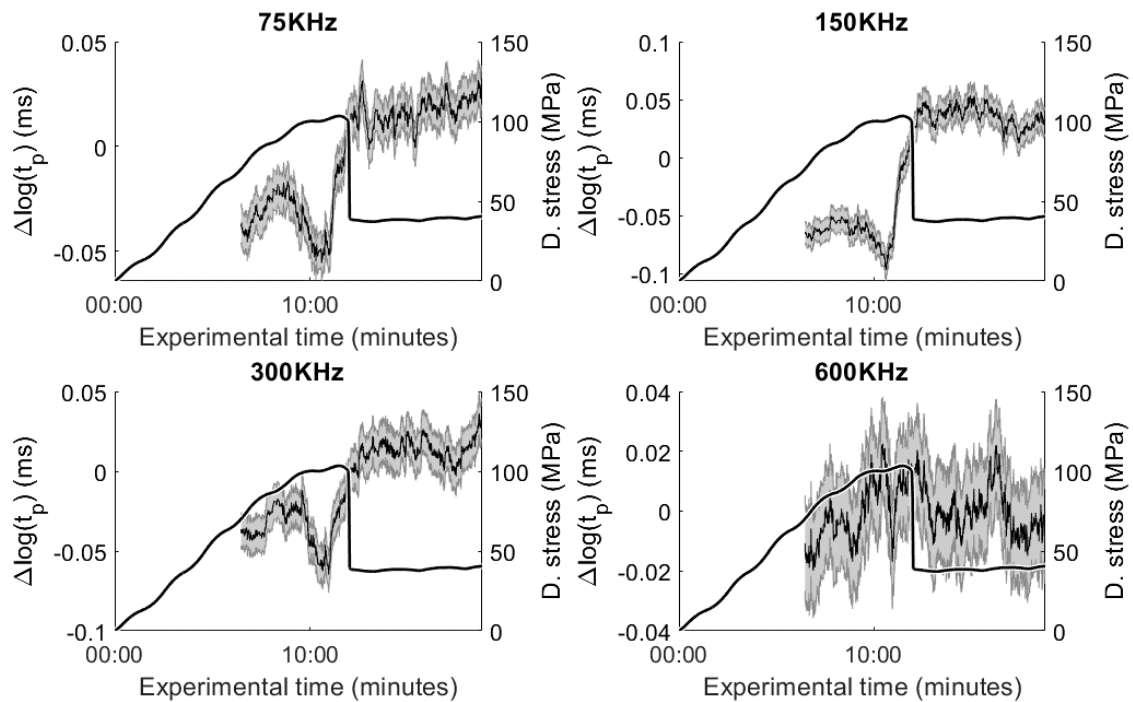


Figure 5.4: Average values of Peak Delay are plotted with their standard error (shaded region) in a moving window of 1500 measurements for each of the analysed frequency bands. Comparison with differential stress highlights a marked increase in the average delay following dynamic failure of the samples.

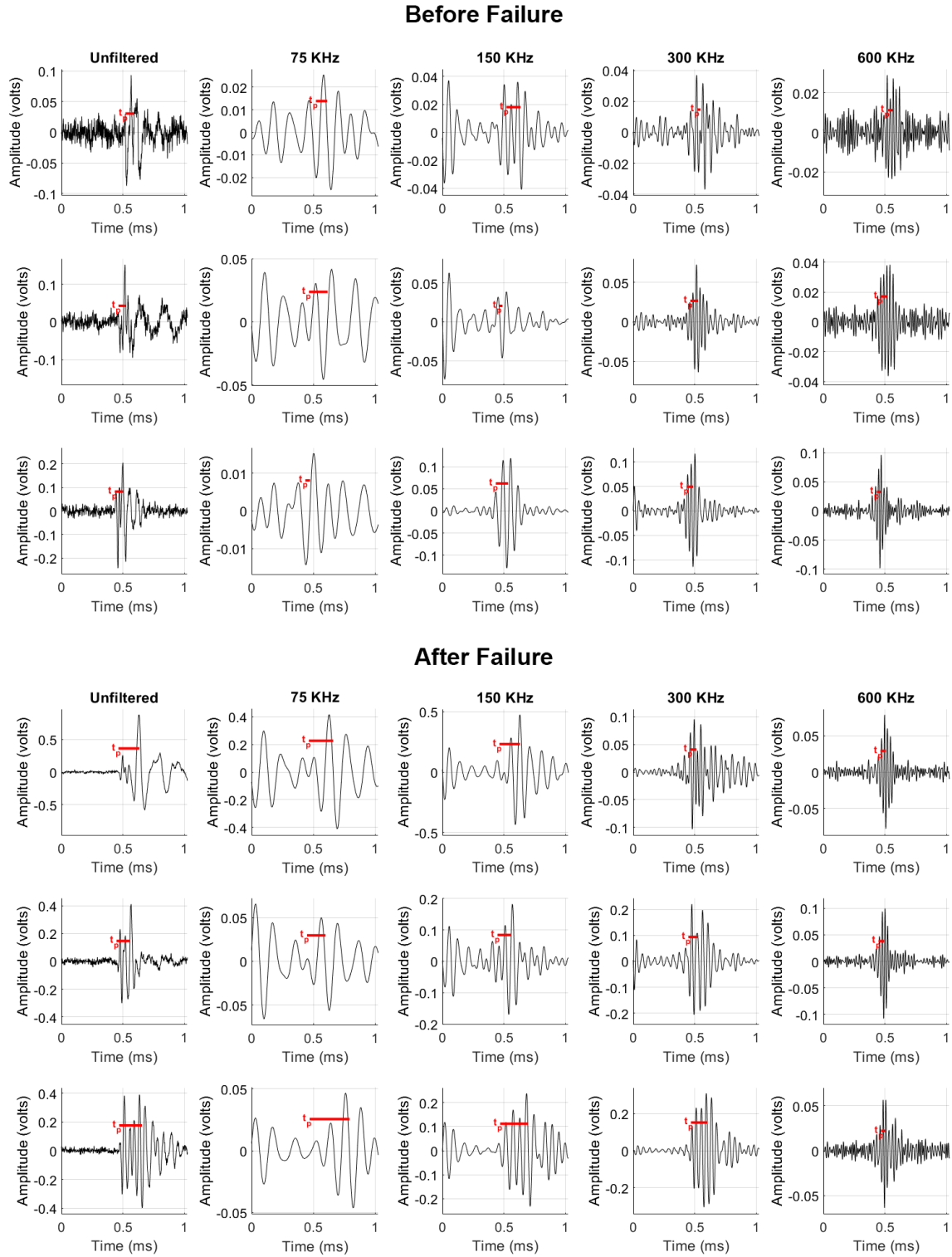


Figure 5.5: Selected waveforms from the sandstone highlight the changing frequency content for before and after sample failure for DDS. As with Figure 5.4, a marked increase in Peak Delay values occur following shear zone coalescence. This trend does not occur at 600 KHz where Peak Delay remains relatively constant.

Peak Delay averages (moving window of 1500 measurements) are plotted against time and compared with differential stress. The shaded region indicates the standard error of the moving window. Except for 600 KHz, values of $\Delta \log(t_p)$ are significantly higher following dynamic failure of the two samples at approximately 30 minutes and 10 minutes respectively. Four periods of Peak Delay development can be identified in each of the panels; 1) A steady increase of values until the crack damage threshold (Figure 1.8, intro), 2) A decrease in values until maximum stress, 3) A rapid and sudden increase of $\Delta \log(t_p)$ during dynamic failure that ends with permanently high values in 4), A phase of consistently high values during the post-failure phase of deformation.

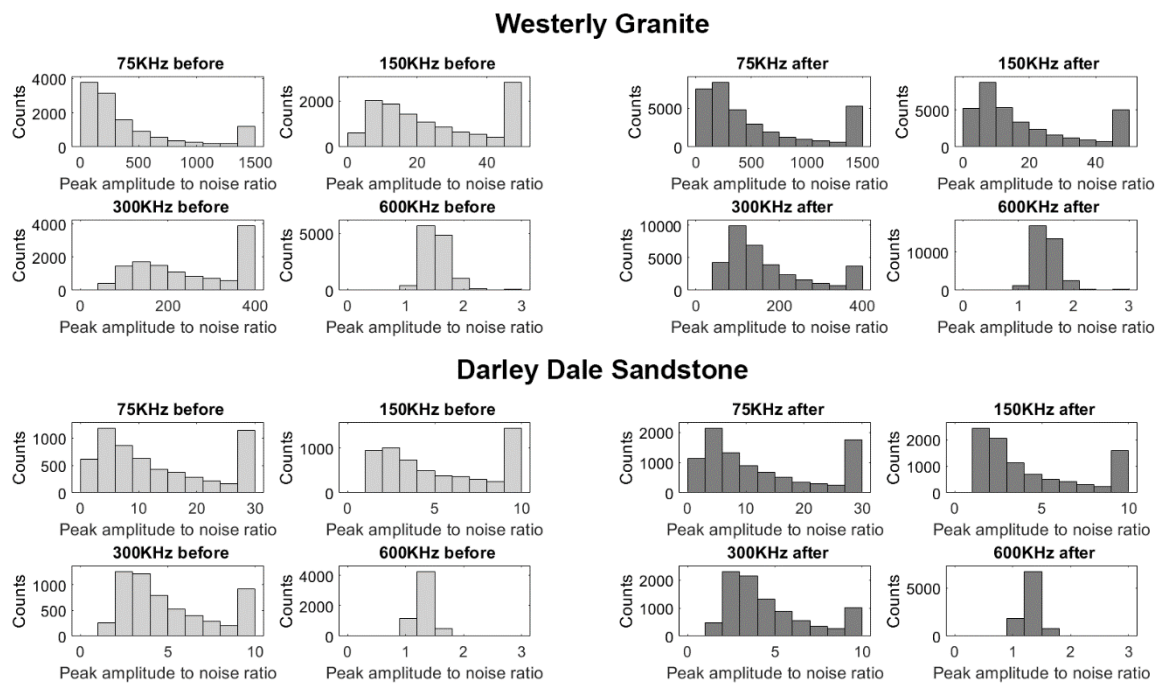


Figure 5.6: Peak amplitude to pre-signal noise ratios are calculated for each Peak Delay measurement to investigate differences in waveform attenuation for before and after failure. Although the effect is minor, attenuation does play a role where counts of low and high amplitude ratios increase and decrease respectively.

Selected high amplitude waveforms (**Figure 5.5**) highlight the change in character of frequency content following shear zone coalescence. Very high amplitudes in the pre-signal noise at 75 KHz do suggest corruption of the actual signal may occur when peak amplitude to noise ratios are low. However, waveforms for after failure do show an increased broadening, and thus higher Peak Delay, at the lower frequencies that is not present at 600 KHz. The lack of any change in the waveform filtered at 600 KHz in each of these plots suggest that at these high frequencies, wavelengths are potentially simply too

short to sample the correlation distance of heterogeneities present in the laboratory samples under normal Rayleigh scattering. However, the assumption of small-scattering deviations that are used in the far-field should be made with care here due to the small wavelengths and the typical scattering distances (mm to cm scale) present in the laboratory data.

It is likely that waveforms that occur after failure will experience intrinsic attenuation due to crack coalescence that lowers amplitudes below the noise floor. As a simple measure of this, peak amplitude to pre-signal noise ratios are calculated for each Peak Delay measurement. Results are binned (**Figure 5.6**) for before (left) and after (right) failure. Ratio counts reveal minor variations that suggest fault zone structure does indeed attenuate the waveform, counts of low and high amplitude ratios increase and decrease respectively. However, the effect is not deemed to be significant as count distributions remain relatively consistent for before and after failure.

5.3.2 HYPOCENTRE DEPENDENT VARIATIONS

As observed at field scale by Takahashi, et al. (2007), t_p generally increases with hypocentral distance (R) at low frequencies. As with those authors, the deviation of $\log(t_p)$ can be fitted with the linear regression line:

$$\Delta \log(t_p)[f] = \log(t_p)[f] - (A[f] + B[f] * \log(R)), \quad (5.2)$$

where f is the frequency band and A & B are regression coefficients. There are some problems with applying this approach here. The variations in Peak Delay with R, are in fact very low (of the order of 0.1) and the spread in the data becomes very high as frequency increases (**Figure 5.7**). When the level of heterogeneity increases, as in exploration or volcano seismology, large angle (also known as Mie or resonance) scattering becomes increasingly important. This is a possible explanation for a family of measurements that occur at $\log(t_p)$ values of -9 ms. Resonance has been recognised as a relevant, fractured-induced effect at 100 KHz in fractured (manufactured) plexiglass (Shih and Frehner, 2016). As recognized by those authors, in plexiglass, scattering does not play a significant role at 100 KHz while scattering and anisotropy are likely more relevant in a rock, especially during fracturing. As such data will ultimately affect the regression fit, $\Delta \log(t_p)$ is calculated as the deviation around the mean value as described by **equation 5.1**.

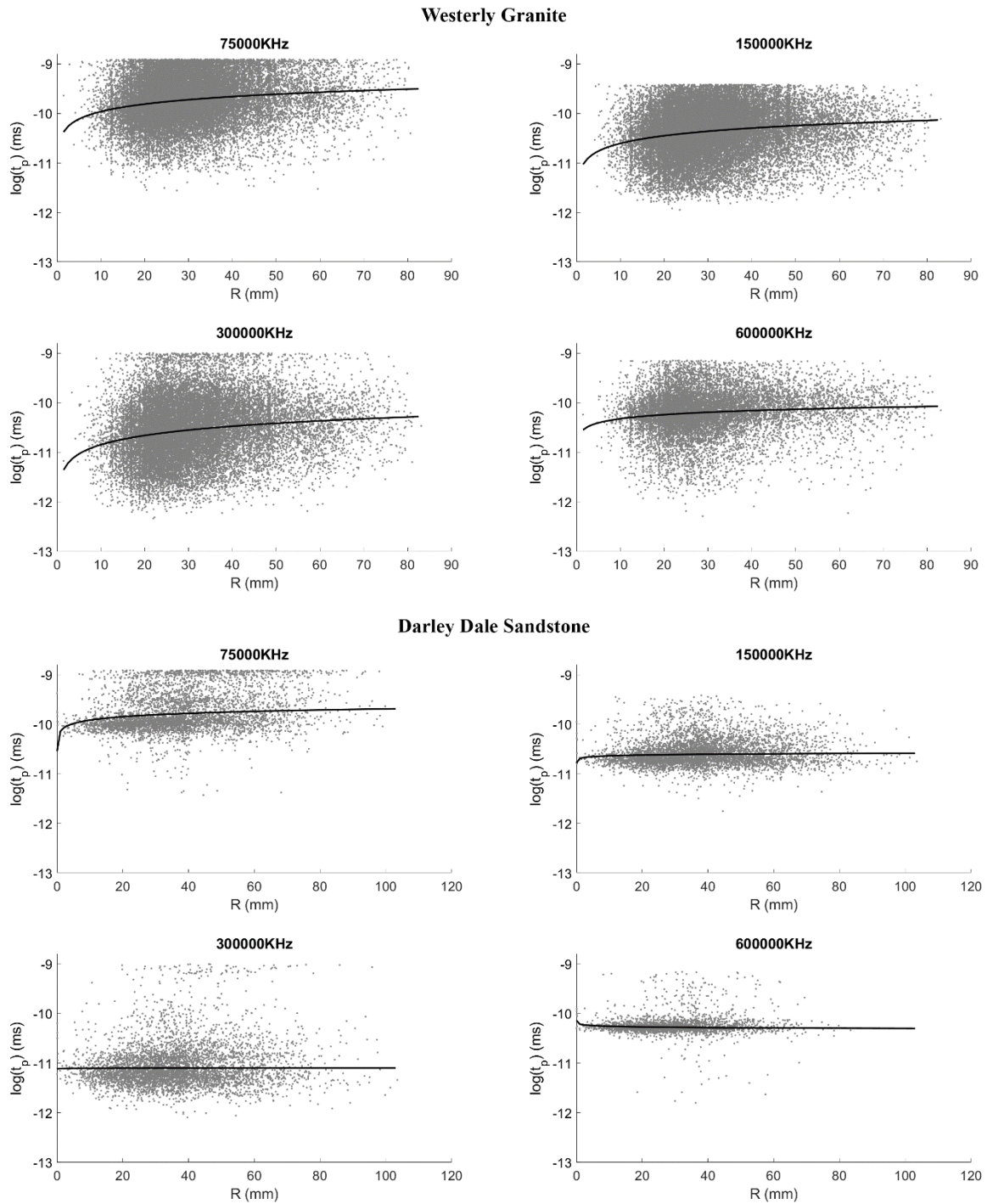


Figure 5.7: $\log(t_p)$ is compared with hypocentral distance R . The black line indicates the regression fit proposed by Takahashi, et al. (2007), however, as the data spread is very high at the higher frequencies and the dependency on R is low, this study calculates the deviation around the average value. A family of anomalously high measurements further suggest the presence of resonant scattering in the data.

5.3.3 MAPPING PEAK DELAY

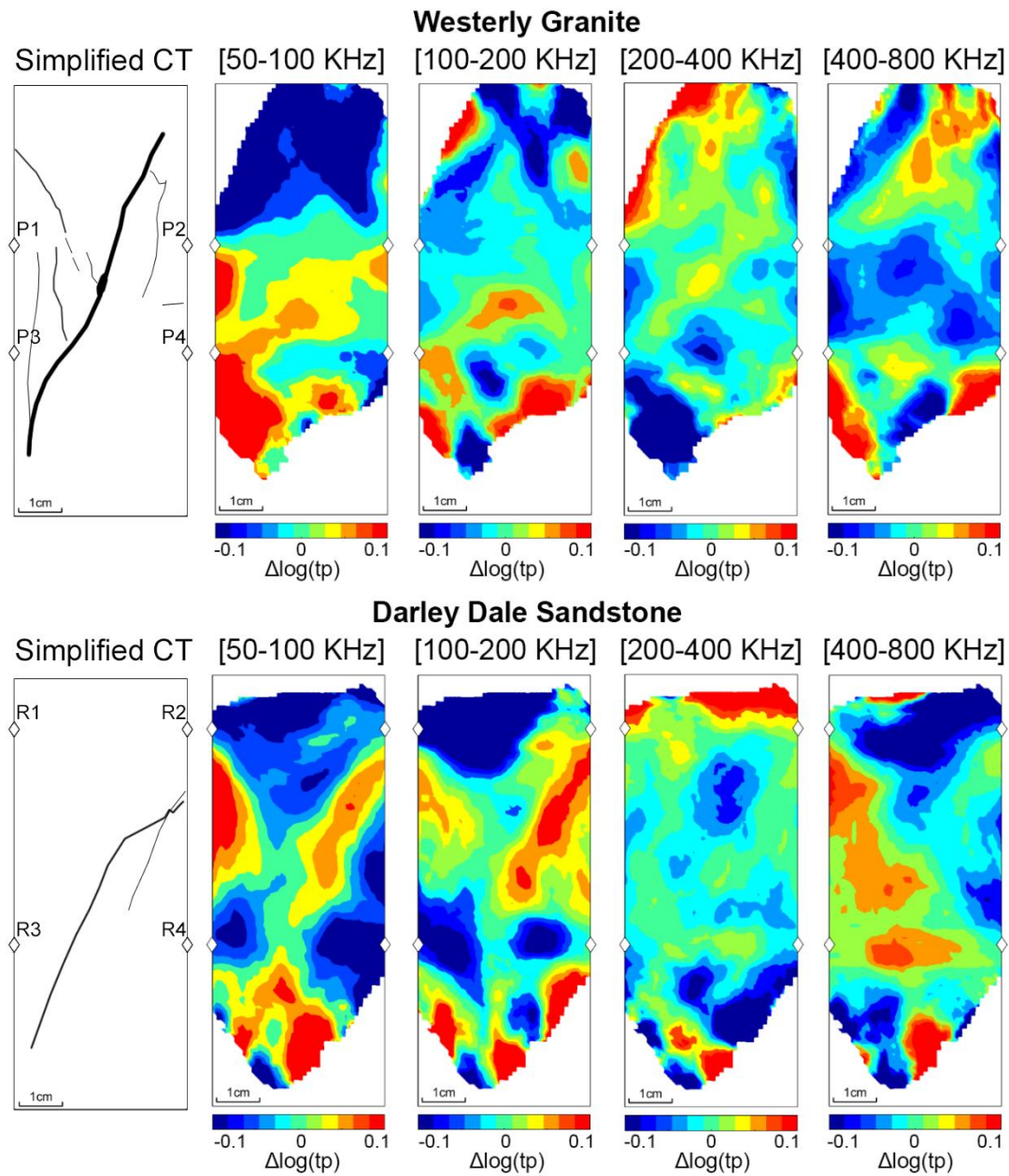


Figure 5.8: Simplified CT image of internal fracture network (left) and spatial distribution of $\Delta \log t_p$ values. Logarithmic Peak Delay variations are shown in the lower colour bar while diamonds show the PZT positions. Only regions crossed by a minimum of 5 rays are displayed. Azimuthal coverage of model blocks (and so confidence) is reduced towards the edges and outside the region delineated by the receivers. Diamonds indicate receivers used in mapping. The bounding boxes indicate the dimensions of the sample.

As with the prior analyses, Peak Delays are revealed to be strongly variable and show spatially dependent trends (**Figure 5.8**). In the case of the granite, regions of high and low $\Delta \log(t_p)$ do not initially correlate very well with the CT Map (top left panel). This

likely due to the diffuse nature of the fracturing within the granite resulting in a heterogeneity that is not evenly sampled from all directions. The sandstone, on the other hand, demonstrates a linear region of high Peak Delay at the low frequencies ([50 -100KHz and [100-200KHz]). The anomaly follows fracture structure (bottom left panel), where the dimensions suggest a sensitivity to the distance between the two linear structures present in the CT image.

5.3.4 2D MODELLING OF ANISOTROPY VARIATIONS

The circular pore is visible as a high Peak Delay anomaly regardless of frequency or simulated coalescence conditions (**Figure 5.9**). Clear variations in the magnitude of the anomaly further highlight a sensitivity of low frequency waves (50-100 KHz) to larger, or less densely distributed, structures such as the pore edges. Moreover, as structures become increasingly coalesced, the highest magnitude of $\Delta \log(t_p)$ shifts to higher bandwidths. The dimensions of the inclusion are further shown to play an important role in Peak Delay mapping (**Figure 5.10**). Like the fully coalesced pore in **Figure 5.9**, modelling demonstrates a frequency isotropic Peak Delay anomaly for inclusions that are roughly equant. However, when the thickness of the inclusion is less than its length, anomalies begin to show significant variation, becoming negative in the last set of panels.

One possible explanation for these observations is the presence of a direct wave and a transmitted wave in the data (**Figure 5.11**). When energy propagates across the length of the fracture, only a small portion of the wave front will directly sample the inclusion resulting in two separate arrivals at low angles of incidence (relative to the orientation of the inclusion). This is further revealed in **Figure 5.12** where a family of anomalously low Peak Delay values that may corrupt the mapping. An alternative explanation, however is the previously discussed resonance scattering generating additional surface waves when energies of a specific wavelength interact with similarly scaled structure. Although it is outside of the scope of this thesis, the results of this study suggest resonance is playing a role in the measurements. Further studies into Acoustic Emission should investigate these effects using a more appropriate modelling approach than the one presented here (e.g. Zhu and Carcione, 2014). The simulations presented here do show at least that the creation of internal interfaces in the sample will produce important delays in the peak of the waveform amplitudes.

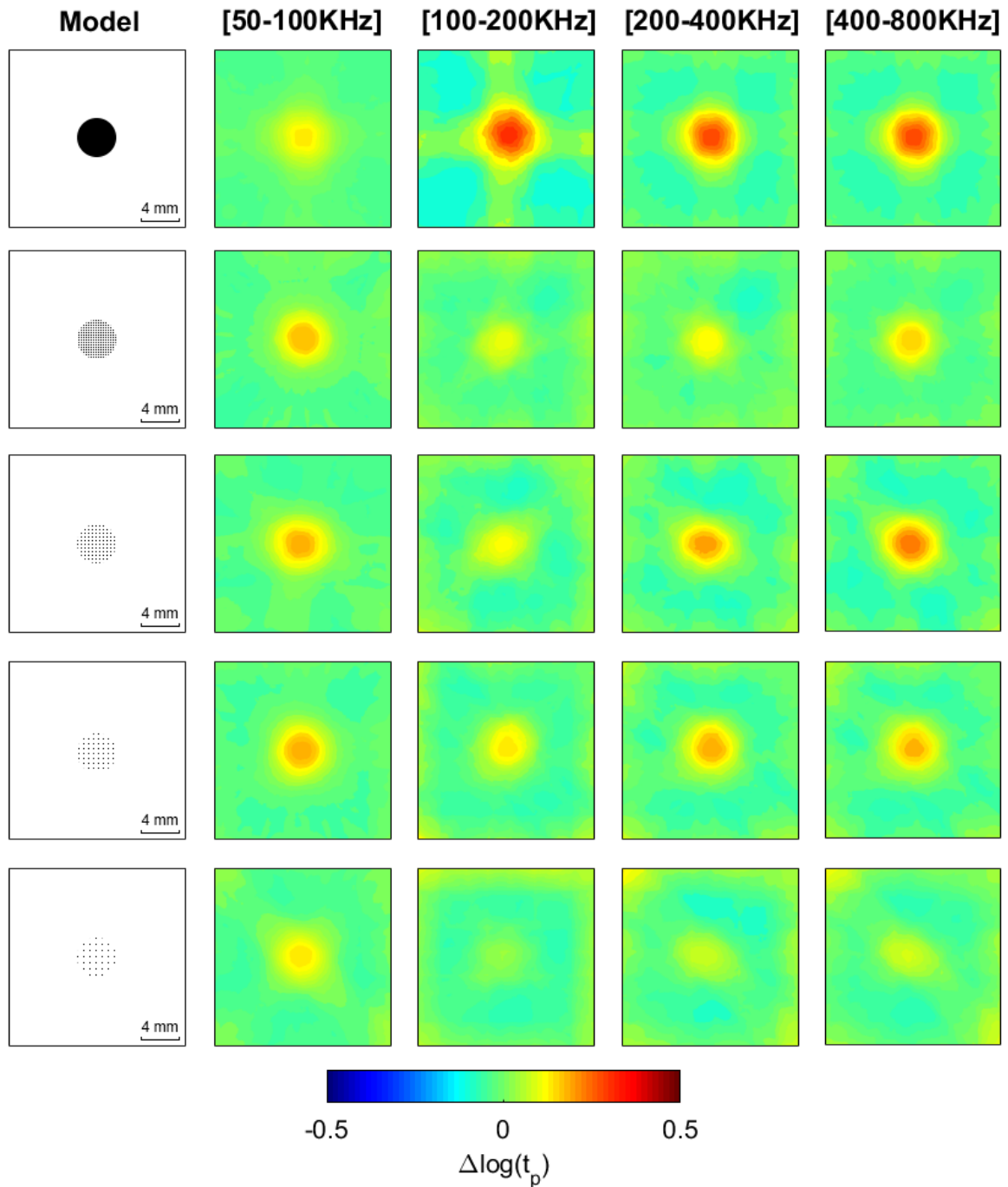


Figure 5.9: Synthetic circular pore Peak Delay modelling. To simulate coalescence conditions, pore structure becomes increasingly sparse. Modelling identifies clear structure dependent amplitude variations of $\Delta\log(t_p)$. Sparsely distributed structure more strongly influences lower frequencies with a high Peak Delay anomaly shifting to higher frequencies as coalescence increases. Once fully formed, the circular pore demonstrates very high Peak Delay anomalies for all frequency bands.

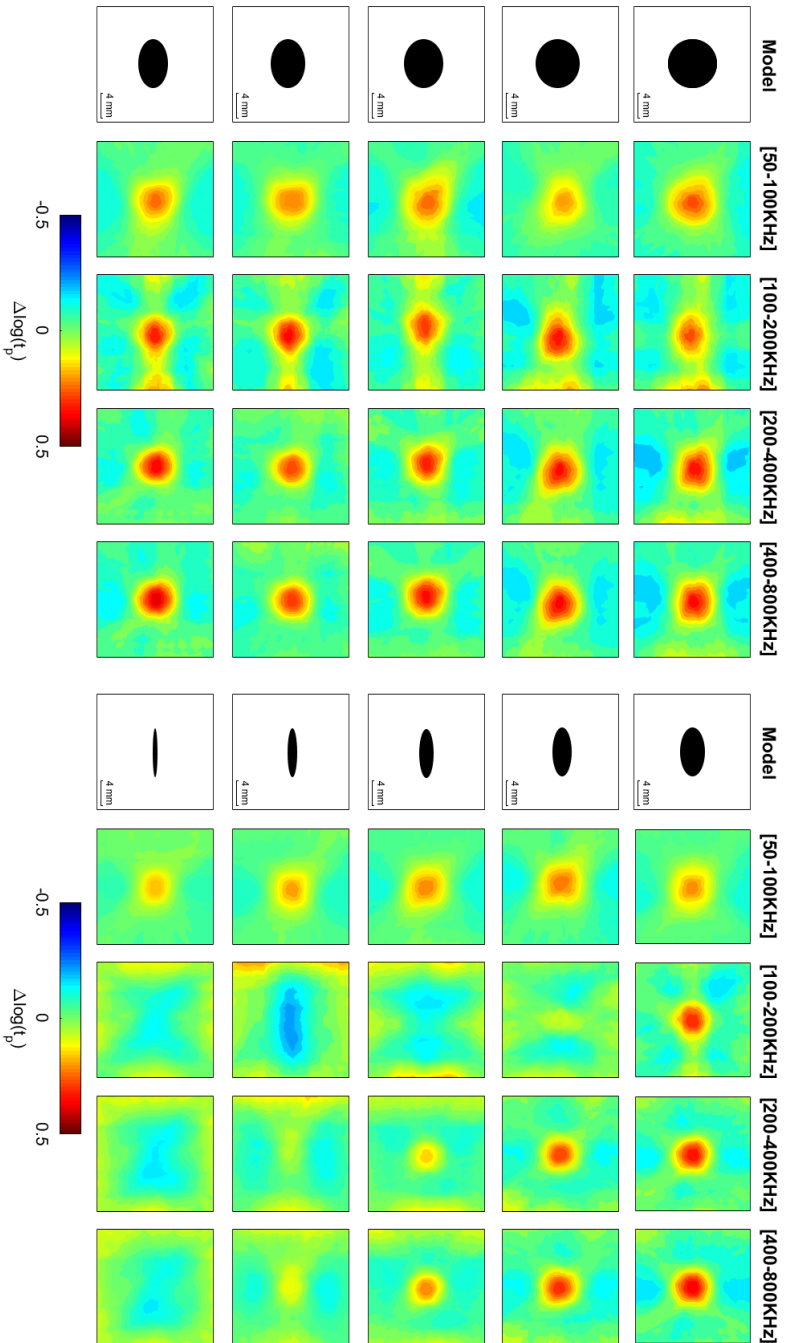


Figure 5.10: Synthetic fracture width Peak Delay modeling. To simulate the effects of fracture width, the aspect ratio of an equant pore is increased in steps of 0.1. When the aspect ratio is beyond 0.5 (left-hand side) the Peak Delay anomaly remains largely unchanged. Near-field radiation is present along the medium edges, particularly at 100-200KHz, although the effect is limited to within a few mm. Peak Delay anomalies begin to significantly vary when the aspect ratio is below 0.5 (right-hand side). As with Figure 5.9 these variations are attributed to interference between direct and transmitted waves.

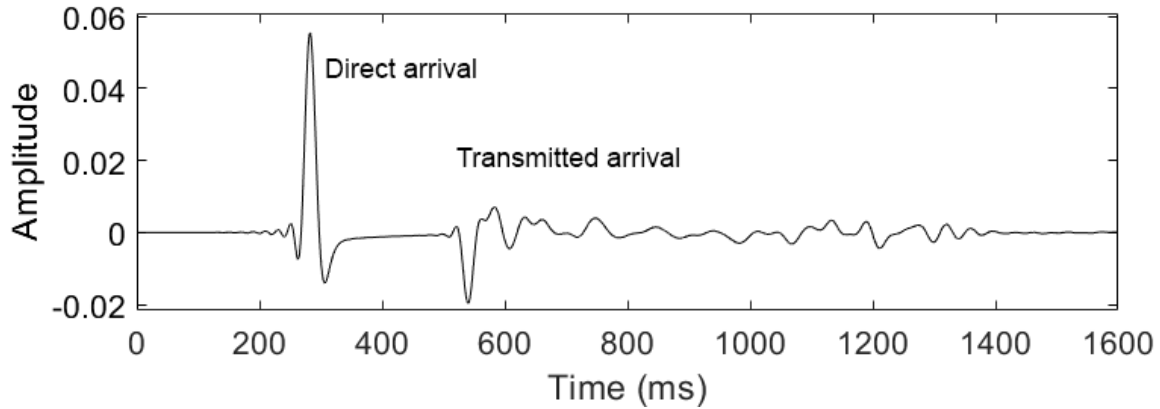


Figure 5.11: Synthetic waveforms reveal the occurrence of two separate wave fronts in the form of direct and transmitted arrivals. These occur when energy propagates along the length of a narrow inclusion.

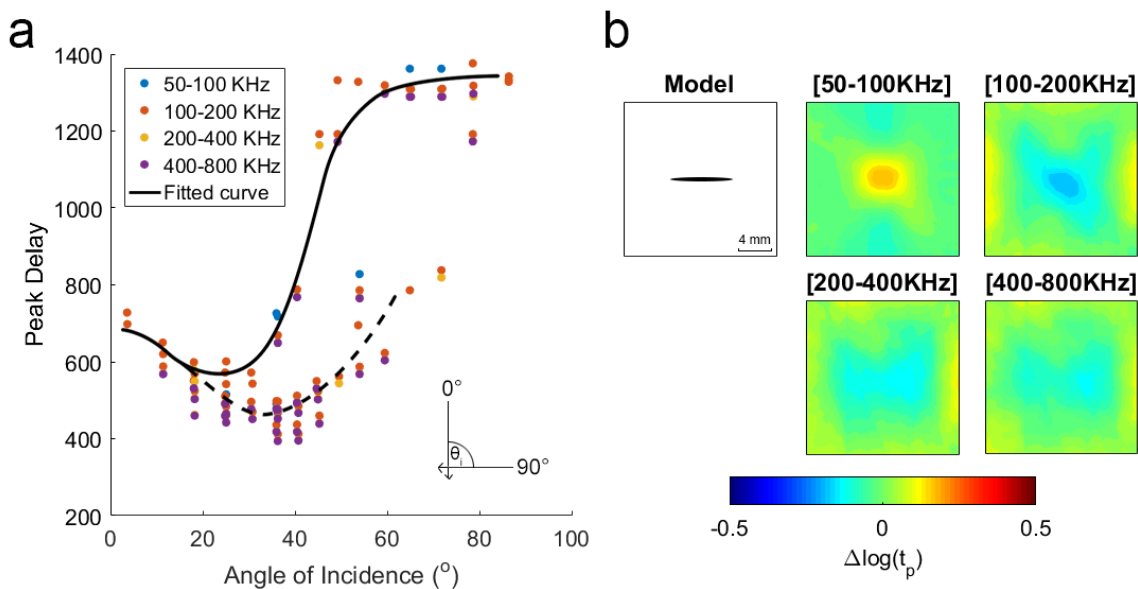


Figure 5.12: a) Angle of Incidence θ_i vs. Peak Delay for synthetic narrow fracture modelling. Below 30° and above 60° Peak Delays are reflective of the travel time through the fracture medium (solid line). Anomalous low values (dashed line) are present between 30° and 60° when energy that travels around the fracture arrives just before the transmitted wave. b) This strongly affects tomography results where the Peak Delay anomaly is observed to rapidly invert as frequency increases. As it is difficult to separate the direct from the transmitted wave at these small hypocentral distances, it is suggested that this behaviour be used as an indicator for narrow or sparse structure.

5.4 DISCUSSION

From the results presented here (**Figure 5.8**), the ability of Peak Delay at imaging fracture networks likely comes from the high acoustic impedance (AI) contrasts of deformation structure with respect to the surrounding, more homogenous medium. Pyrak (1988) and Pyrak-Nolte et al. (1990) demonstrated that the acoustic impedance of fractures follows the equation $AI = k/\omega$, where k is the fracture stiffness (stress/length) and ω is the angular frequency of the wave. As the strength of acoustic impedance directly controls the seismic visibility of a structure, this relation suggests that high Peak Delays are dependent on both fracture stiffness and the frequency of the sampling wave.

Even so, as structural complexity increases (e.g., in Westerly Granite) the imaging ability at the laboratory scale rapidly diminishes as more receivers are required to ensure sufficient coverage around masking structures. Moreover, structures that form late in the experiment will not be visible as they will not be adequately sampled. Whilst this presents a challenge to tomographic techniques, further analysis of how heterogeneity evolves through time, for instance reactivation of microfractures, and its relationship to Peak Delay is required: such an observation could track the changing stress field of, e.g., underground reservoirs.

Rao & Wang (2009) noted that seismic attenuation parameters are strongly dependent on fracture thickness and orientation. In field mapping, where receiver distribution is typically at a scale larger than the structures of interest, this leads to the ability of scattering to image high acoustic impedance at the surface: low-frequency (3 Hz) Peak Delays are able to contour extinct shallow volcanic centres and even wide 10-m thick debris flows (De Siena, et al., 2016). Similar effects have recently been observed at even shallower depths and in relation with the distribution of trees at sub-wavelength scale (Colombi et al., 2016)

In general, fractures act as a low-pass filter where the characteristic cut-off frequency (ω_c) is dependent on fracture stiffness ($\omega_c \propto \text{stiffness}$ - Schoenberg, 1980). For a given frequency, only portions of the fracture with stiffness high enough to produce an ω_c higher than the frequency of the propagating wave will transmit the signal, while regions with lower ω_c will more likely reflect or backscatter the energy in the coda of the signal. As a result, the transmitted wave will only sample the stiffer portions of the fracture

structure, where different frequencies sample different subsets of the geometry. Large open fractures thus affect lower frequency bands more than small stiff fractures (Baird et al., 2013; Biwa et al., 2007; Pyrak-Nolte and Nolte, 1992). This suggests that Peak Delay is a measure of forward scattering due to stiff fractures sampled along the raypath and the frequency dependence of $\Delta \log(t_p)$ a result of the inhomogeneous distribution of structures in the sample. High Peak Delays are simply the dynamic response of elastic waves sensitive to the intrinsic length scale of heterogeneity present in the system.

Something that is not adequately addressed by this study, are those data that are affected by resonance scattering. Particularly frequencies above 150 KHz will be strongly affected and this likely explains the loss of recognisable structures in the mapping. Several attempts were made to remove such data, however automated removal methods proved inconclusive. As Peak Delay values, normally, do not vary strongly with frequency, removing waveforms with high standard deviations of measurements, or simply using a window to remove those high valued events showed some promise. What is required is an approach that can reliably identify those events that are affected by Mie scattering and those that can be assumed to be dominated by Rayleigh scattering. Both processes act as markers of heterogeneity, but the time at which they are recorded in the waveform are different. Indeed, Mie scattering should be considered in any attenuation modelling involving the late coda as such measurements will corrupt amplitudes.

Following these analyses, it is likely that the relative simplicity of the deformation structure allows for the imaging of the shear zone in the sandstone (**Figure 5.8**, DDS). The higher confining pressures and initially porous media readily encouraged the formation of large tensile fracturing in a localised region resulting in high Peak Delays similar to those in the circular pore model (**Figure 5.9**). Conversely, the granite (**Figure 5.8**, WG) which was deformed at a lower confining pressure, demonstrates a far broader zone of damage with significant axial splitting. This complexity of structure resulted in Peak Delay maps that more closely follow the narrow fracture models of **Figure 5.10** with rapid inversions of Peak Delay value as frequency is increased.

5.5 CONCLUSIONS

I adapted standard approaches of Peak Delay and focal mechanism analysis to map shear zone structure and deformation features created in triaxial deformation experiments

of Westerly Granite and Darley Dale Sandstone. Furthermore, the study provides new information to evaluate the biases induced by the relative geometry of acoustic impedance structure and source receiver array in regions of strong deformation. Measurement of seismic Peak Delay on acoustic emission data highlight frequency dependent results that are strongly influenced by the distribution of heterogeneity and stiffness.

At low frequencies (50-100 KHz), regions of anomalously high Peak Delays typically contour broader macroscopic structure such as the shear zone. As frequency is increased, further dependencies on fracture coalescence, orientation and width are identified. When fractures are narrow or sparsely distributed and orientated between 30° and 60° to a propagating wavefield, energy that travels around the structure arrives to a receiver shortly before the transmitted energy. As these arrivals often overlap each other at the low hypocentral distances analysed here, it results in an anomalously low measurement of Peak Delay that is difficult to correct. However, as this effect is weakest at the low frequencies, a significant reduction in Peak Delay in the higher bandwidths can be used as an indicator for sparse or narrow structure.

Furthermore, as a macro-fracture becomes increasingly coalesced, e.g. through a reduction in the distance between adjacent microfractures, the maximum Peak Delay is observed to shift to higher bandwidths. Once a fracture is fully coalesced, it demonstrates a high-magnitude, frequency-isotropic peak-delay. With consideration to the results presented here, I propose it is possible to perform frequency characterisation of time-dependent deformation structure and track the development of a shear zone using Peak Delays.

6 CONCLUDING REMARKS

The overarching objective of this thesis was the development of a set of tools to analyse Acoustic Emission data from triaxial deformation testing of rock samples. The purpose being to elucidate subtle changes of the waveform in response to developing fracture structure, with the longer-term view to improving understanding of field-scale processes. However, due to the unique nature and scale of the laboratory environment several challenges were encountered that eventually decided how the research would progress. Although the studies here were presented in a somewhat sequential order of arrival time, mechanism source and propagation path effects, the research itself was very much a back and forth process with each of the presented chapters heavily dependent on the results of the others.

First and foremost, the greatest challenge was found in picking the arrival time of waveforms. Although this is a common occurrence in time series analysis (there are many studies dedicated to this field of research), AE are characteristically low amplitude with complex source effects which are not sufficiently attenuated over cm scale hypocentral distances. This is further compounded by several thousand AE that can be detected in a single experiment, thus requiring an automated approach. In **chapter 3**, I propose training a Time Delay Neural Network to recognise the differences between signal and background noise. This proved to be incredibly powerful as it relied on a “best fit” approach of multiple waveform derived parameters. For example, over 3 million waveforms were automatically picked for the focal mechanism analysis using this methodology, revealing details that may not have been observed with other techniques.

The next set of difficulties revolved around separating out the effects of the source and the path on waveform characteristics. Source classification was addressed in **chapter 4** using a least squares minimisation of the fit between 3D focal spheres of measured first-motion polarity and idealised models of tensile, shearing and compaction type fracturing mechanisms. Results revealed clear trends in the type and distribution of the different mechanisms that demonstrated dependencies on individual rock properties and the environmental conditions used in the study. One of the most important features identified were a discrete phase of low amplitude tensile fracturing associated with crack coalescence. The timing of these events followed a log-linear relationship with confining pressure highlighting the potential for failure forecasting. Furthermore, a transitional phase

between axial splitting and fault plane localisation was identified using divergence maps of mechanism slip vectors, providing additional clues to the type of dynamic failure that will occur.

In **chapter 5**, I investigated the forward scattering effects of developing fracture structure on the Acoustic Emission waveform. By modelling the Peak Delay of arriving energy as a result of deforming structure results highlight that clear frequency dependent variations do occur due to changes in the medium. However, the processes by which this occurs is complex, both Rayleigh (small angle) and Mie (resonance or large angle) scattering occur and are dependent on the wavelengths and the scale of scattering structure as revealed by synthetic modelling. Furthermore, the dynamic nature of the experiments meant that such structure was constantly evolving, resulting in additional complexity that could not be fully accounted for.

Irrespective of the challenges encountered, this thesis has demonstrated that the Acoustic Emission waveform is a powerful diagnosis tool for rock deformation experiments. Waveforms have been shown to dynamically evolve through varying source and path effects, immediately reacting to deformation structure as it coalesces and allowing for 4D mapping of fracture development. Furthermore, with the advent of easy-to-apply machine learning methodologies, these effects can be observed at a sufficiently high resolution to make quantitative predictions on how fracture structure will evolve through time. Ideally providing avenues on how such techniques may be applied at the field scale for use in the prediction and disaster mitigation of earthquakes and volcanoes, as well as industrial applications in oil and gas extraction, CO₂ sequestration and other sub-surface investigations of fractures and faulting.

7 APPENDIX: MATLAB CODE

The main programs created for this thesis are available below. The codes and the various dependencies that are used throughout are available at <https://github.com/thomaskingunito/thesismatlabcodes>. All the codes are written to work with MATLAB version 2018a.

7.1 WAVEFORM PICKING AND LOCATION

7.1.1 TRAIN PICKING MODEL

This is a semi-supervised programme to train a distributed time delay neural network to recognise the differences between pre-signal noise and signal. It has two main elements; 1) A supervised picking stage where the user manually selects the time of arrival on 5 high amplitude waveforms. 2) An unsupervised picking stage where the algorithm is sequentially trained automatically using several 'quality' ratios to evaluate the data. It is suggested to create a unique picking model for each experiment. Training datasets are created from the experimental data itself (stored in folder sg2). Model is trained in sequential batches and steadily improves as more data is incorporated.

7.1.1.1 VERSION

Version 1.0, 16th January 2019. Thomas King - First Version

7.1.1.2 PARAMETER CUSTOMISATION

Below are the suggested parameters to be modified. I don't recommend changing any of the code outside of these parameters.

```
clear all; close all;

% This is the name of the picking model. I recommend to use folder names to
% avoid confusion as this testname is required when using the locating code
testname = 'Example-Training-Model';

% Set to 1 (yes) or 0 (no) to compile the training dataset
compile = 0;

% Resamples waveforms to a shorter length. It can increase the speed of the
% code but time resolution is lost.
sigsamp = 2048;

% Minimum arrival time. Recommended at 10% of signal length
```

```

minpick = round(sigsamp/10);

% Neural network parameters
d1 = 0:20; d2 = 0:5; % Delays
dtdnn_net = distdelaynet({d1,d2},5); % Hidden sizes set to 5
dtdnn_net.trainFcn = 'trainbr'; % Model trained with bayesian regularisation
dtdnn_net.divideFcn = '';
dtdnn_net.trainParam.epochs = 10; % Model is trained for 10 epochs per sequence
dtdnn_net.trainParam.min_grad = 3e-4;

% Manual training size
manualsize = 5;

% Size of training dataset
trainingsize = 10000;

% Number of training events per sequence
batchsize = 10;

% Final number of events to be in the model
modelsize = 304;

```

7.1.1.3 DATA COMPILATION

To avoid continual re-reading of data, training waveforms are compiled into a single matrix.

```

if compile == 1
    index = 0;
    dirs = dir('sg2/*seg2'); % Directory search for waveforms
    index = 0; clear event
    for i = 1:size(dirs,1)
        event{i,1} = dirs(i).name; % Compile filenames
    end
    cd sg2;
    for i = 1:length(event)
        t = randi(length(event)); % Random waveform selection
        try
            [signal,SR] = leggisg2(char(event{t})); % Load data
            if index == 0
                Ts = SR; % Obtain sampling rate
                Fs = 1/SR; % Obtain sampling frequency
            end
        catch
            continue
        end
        for r = 1:size(signal,2)
            index = index+1; % Compiles data into a single matrix
            allsig(:,index) = resample(signal(:,r),sigsamp,length(signal(:,r)));
        end
        if index > trainingsize % Stop compiling when dataset is big enough
            break
        end
    end
end

```

```

end
cd ..
save rays.mat allsig SR % Store waveform data
end
load rays.mat
Ts = SR*10;
Fs = 1/SR;

```

7.1.1.4 SUPERVISED TRAINING WITH HIGH AMPLITUDE DATA

Interactive manual picking for initial training dataset. User picks the onset and end of the main pulse of the waveform. If the onset is uncertain, click twice off of the graph to the right to skip that data.

```

% Reset parameters
p = []; t = [];
index = 0;
istore = 0;

while index < manualsize

    % Randomly find high amplitude waveform
    amp = 1;
    while amp > 0.1
        i = 0;
        while ismember(i,istore) == 1
            i = randi(size(allsig,2));
        end
        sig = allsig(:,i); sig = sig./max(abs(sig));
        amp = max(abs(sig(1:100)));
    end
    sig = allsig(:,i);

    % Compiles input data
    try
        IFcontent
    catch
        continue
    end

    % Interactive picking plot
    y = (test(:,2)./max(test(:,2)))';
    y(end) = NaN;
    col = cc'.*scalef; % This is the color, vary with x in this case.
    figure(1); subplot(2,1,1); yyaxis left; cla;hold on

    patch(1:1:length(y),y,col,'EdgeColor','interp','Marker','none','MarkerFaceColor','flat');
    colormap(jet)
    xlim([0 sigsamp])
    figure(1); subplot(2,1,2); yyaxis left; cla;hold on
    plot(esig,'r-')
    yyaxis right; cla;
    plot(sn,'b-')
    xlim([0 sigsamp])

```

```

title('Pick signal pulse start')
[pk1,pk2] = ginput(1);
title('Pick signal pulse end')
[pk3,pk2] = ginput(1);

sigtest = sigsamp;

% Training sequence
if pk1 < sigtest && minpick ~= pk1

    % Compiles training vectors
    try
        training_vector
    catch
        continue
    end

    % Train the model
    index = index + 1;
    if index > 1
        p_mul = catsamples(p_mul,p1,'pad');
        t_mul = catsamples(t_mul,t2,'pad');
        [p,Pi,Ai,t] = preparets(dtdnn_net,p_mul,t_mul);
        dtdnn_net = train(dtdnn_net,p,t,Pi);

        % Sometimes the training fails and the model breaks, this is a
        % workaround.
        if sum(isnan(tr.gradient)==1) > 0 | tr.gradient > 100
            load(char(['pkmodel-'
',char(testname),'.mat']),'p_mul','t_mul','dtdnn_net','sigstore','istore')
            continue
        else
            istore = [istore;i]; % Do not repeat waveforms in model
            sigstore{end+1} = sig;
            save(char(['pkmodel-'
',char(testname),'.mat']),'p_mul','t_mul','dtdnn_net','sigstore','istore')
        end
    else
        % Builds initial model for first waveform. Modify this add more
        % data categories
        dtdnn_net.numinputs = 3;
        dtdnn_net.inputConnect = [1 1 1; 0 0 0];
        dtdnn_net = configure(dtdnn_net,p1);

        dtdnn_net.inputweights{1,1}.delays = [0:1:10];
        dtdnn_net.inputweights{1,2}.delays = [0:1:10];
        dtdnn_net.inputweights{1,3}.delays = [0:1:10];

        [dtdnn_net,tr] = train(dtdnn_net,p1,t2);
        p_mul = p1;
        t_mul = t2;
        sigstore{1} = sig;
    end
end
end
end

```

```
save(char(['pkmodel'-
',char(testname),'.mat']), 'p_mul', 't_mul', 'dtdnn_net', 'sigstore', 'istore')
```

7.1.1.5 UNSUPERVISED TRAINING

This section works in the same way as before but uses 'quality' ratios to select training data

```
% Reset parameters
load rays.mat; close all;
load(char(['pkmodel'-
',char(testname),'.mat']), 'p_mul', 't_mul', 'dtdnn_net', 'sigstore', 'istore')
i = 0;
ampadj = 0;
pick_p1_cat = [];
pick_t2_cat = [];

% Training sequence
testindex = 0;
while size(p_mul{1,1},2) < modelsize
    Ts = 1/Fs;
    amp = 2;
    while amp >= 0.95 || amp < 0.05 % Amplitude range
        i = istore(1);
        while ismember(i,istore) == 1
            i = randi(size(allsig,2));
        end
        sig = allsig(:,i); sig = sig./max(abs(sig));
        amp = max(abs(sig(1:100)));
    end

    sig = allsig(:,i);
    Ts = Ts*(length(sig)/sigsamp);

    try
        IFcontent
    catch
        continue
    end

    y = (test(:,2)./max(test(:,2)))';
    y(end) = NaN;
    col = cc'.*scalef; % This is the color, vary with x in this case.
    figure(1); yyaxis left; cla;hold on

    patch(1:1:length(y),y,col,'EdgeColor','interp','Marker','none','MarkerFaceColor','flat');
    colormap(jet)

    p1 = [con2seq(cc(1:length(sn)))';con2seq(esig(1:length(sn)));...
        con2seq(sn(1:length(sn)))];

    % Using the current model iteration, the current waveform is picked
    o = 0; % Tells the picking code that this is a training sequence
    try
```

```

        pick_output_3
    catch
        continue
    end

    figure(1); yyaxis left;
    plot(yp, 'k-')
    ylim([-2 2])
    drawnow
    pk1 = ind(1);

    % Finds the end of the main pulse, otherwise training vector is a fixed
    % length. Data is then plotted
    try
        esig2 = double(envelope((x(1:sigtest))',50,'rms')); esig2 =
    esig2./max(abs(esig2));
        pk3 = find(esig2(round(pk1+(sigsamp/20.48)):end) < ...
            max(esig2(round(pk1-(sigsamp/20.48))-100:round(pk1-(sigsamp/20.48))))); pk3 =
    pk3(1) + round(pk1+100);
    catch
        pk3 = pk1 + 200;
    end
    figure(1); yyaxis left;
    scatter(pk1,0, 'bo', 'filled')
    try
        scatter(ind2,0, 'ro', 'filled')
        plot(yp2, 'r-')
    end
    scatter(pk3,0, 'bo', 'filled')
    drawnow

    % Picking 'quality' ratios
    try
        output_quality
    catch
        continue
    end

    % Do NOT adjust these values. They work.
    if sn3 > 0.3 && sn2 > 2 && sn1 > 1.5 && minpick ~= pk1
        try
            training_vector
        catch
            continue
        end

        p_mu1 = catsamples(p_mu1,p1, 'pad');
        t_mu1 = catsamples(t_mu1,t2, 'pad');
        testindex = testindex +1;
        plot(yp, 'r-')
        istore = [istore;i];
        sigstore{end+1} = sig;
        if testindex > batchsize
            testindex = 0;
            [p,Pi,Ai,t] = preparets(dtdnn_net,p_mu1,t_mu1);
            [dtdnn_net,tr] = train(dtdnn_net,p,t,Pi);

            if sum(isnan(tr.gradient)==1) > 0

```

```
        load(char(['pkmodel'-
',char(testname),'.mat']), 'p_mul', 't_mul', 'dtdnn_net', 'sigstore', 'istore')
        continue
    else
        ampadj = ampadj + (0.5/150);
        save(char(['pkmodel'-
',char(testname),'.mat']), 'p_mul', 't_mul', 'dtdnn_net', 'sigstore', 'istore')
        display(['Number of training data: ', num2str(size(p_mul{1,1},2))]);
    end
end
end
end
save(char(['pkmodel'-
',char(testname),'.mat']), 'p_mul', 't_mul', 'dtdnn_net', 'sigstore', 'istore')
display(['Number of training data: ', num2str(size(p_mul{1,1},2))]);
```


7.1.2 GENERATE VELOCITY MODEL

Creates an output velocity model, identical to the one produced by InSite. Survey data (stored in `sg2_survey`) is automatically picked using an RMS amplitude threshold method. The code attempts to automatically avoid including miss-picked velocities but it is here and there in terms of confidence.

7.1.2.1 VERSION

Version 1.0, 16th January 2019. Thomas King - First Version

7.1.2.2 PARAMETER CUSTOMISATION

```
clear all; close all;

testname = 'Example-Training-Model';
sigsamp = 2048;
figon = 1;
```

7.1.2.3 COMPILE DATA

```
% Waveform origin time
tempi = [];
dirls = dir('sg2_survey/*seg2');
index = 0; clear event
event = cell(size(dirls,1),1);
for i = 1:size(dirls,1)
    event{i,1} = dirls(i).name;
    filename = event{i};
    filename([9,16,20:end]) = '-';
    formatIn = 'yyyymmdd-HHMMSS-fff-----';
    tempi(i,1) = datenum(filename,formatIn);
end
save tempi_survey.mat tempi

% Find receiver positions
if exist('recloc_survey') == 0 || exist('recloc') == 0
    cd sg2_survey
    filename = event{1};
    [tracce,SR,Shot,X,n_samples,RL] = leggisg2(char(filename));
    Ts = SR;
    Fs = 1/SR;
    for j = 1:size(RL,1)
        rec = strsplit(char(RL(j,:)));
        recloc(j,1) = str2num(rec{3}); % NED to XYZ
        recloc(j,2) = str2num(rec{2});
        recloc(j,3) = str2num(rec{4});
    end
    cd ..
    save recloc_survey.mat recloc
end
```

```

% Identify individual survey sequences
minpick = 525;
sepsurvey = diff(tempi);
ind = find(sepsurvey > 1e-4)+1;
ind = [1;ind;length(sepsurvey)+2];

% Source position equals receiver positions
index = 0;
for i = 2:length(ind)
    crows = [ind(i-1):1:ind(i)-1];
    if length(crows)~=size(recloc,1)
        continue
    end
    for r = 1:length(crows)
        index = index+1;
        sourcelocs{index,1} = event{crows(r)};
        sourcelocs{index,2} = recloc(r,1);
        sourcelocs{index,3} = recloc(r,2);
        sourcelocs{index,4} = recloc(r,3);
        sourcelocs{index,5} = temp(crows(r));
    end
end

save sourceloc_survey_m1.mat sourcelocs

% Reset workspace
event = sourcelocs(:,1);
pktimes = cell(size(recloc,1),9,length(event));
i = 1;

```

7.1.2.4 WAVEFORM PICKING

```

i = i - 1;
ordersize= 0;
while i ~=size(event,1)
    % Reset
    pk = cell(size(recloc,1),9); sigM = ones(size(recloc,1),1);
    pk(:, :) = num2cell(NaN);
    sourcestore = cell(1,5);
    filename = [];

    % Load file
    i = i + 1;
    display(['Event ', num2str(i)])
    filename = event{i};
    cd sg2_survey
    try
        [tracce,SR,Shot,X,n_samples,RL] = leggisg2(filename);
    catch
        cd ..
        pktimes(:, :, i) = pk;
        continue
    end
    signal = tracce;
    cd ..

```

```

% Picking
if ordersize ~= size(recloc,1)
    ordersize = ordersize+1;
else
    ordersize = 1;
end
for o = 1:size(signal,2)
    Ts = 1/Fs;
    r = o;
    % Does not pick source waveform
    if o == 1
        pk{r,1} = filename;
        pk{r,2} = NaN;
        pk(r,3:9) = num2cell(NaN);
        continue
    end
    % Does not pick receivers on same axis as source
    if ismember(recloc(r,1),recloc(ordersize(1),1)) &&
ismember(recloc(r,2),recloc(ordersize(1),2))
        pk{r,1} = filename;
        pk{r,2} = NaN;
        pk(r,3:9) = num2cell(NaN);
        continue
    end
    display(num2str(o))

    % Pads data
    n = randn(500,1); n = n./max(abs(n));
    n1 = n.*0.05;
    n = randn(sigsamp,1); n = n./max(abs(n));
    n2 = n.*0.05;
    sig = [n1;resample(signal(:,r)+n2,sigsamp,length(signal(:,r)))];
    Ts = Ts*(length(signal(:,r))/sigsamp);

    % Calculate signal envelope
    esig = envelope(sig,10,'rms');

    % Normalise envelope to pre-signal noise
    esig = esig./max(esig(1:200));

    % Finds first amplitude rise above noise
    ind = find(esig>1.1); ind = ind(ind > 550);
    try
        ind = ind(1);
    catch
        pk{r,1} = filename;
        pk{r,2} = NaN;
        pk(r,3:9) = num2cell(NaN);
        continue
    end

    % Calculate signal to noise ratio around first rise
    sn = []; testrange = 300;
    for s = 1:testrange
        try
            sn(s) = mean(esig((s+ind-round(testrange/2)):(s+ind-
round(testrange/2))+100))/mean(esig((s+ind-round(testrange/2))-100:(s+ind-

```

```

round(testrange/2)));
    catch
        sn(s) = NaN;
    end
end

% Picks highest signal to noise ratio
try
    s = find(sn >= 2); % Preferably above 2
    s = s(1);
    ind = ind-round(testrange/2)+s;
catch
    s = find(sn >= max(sn)); % Otherwise just the maximum
    s = s(1);
    ind = ind-round(testrange/2)+s;
end

% Correct for padding
try
    pk1 = ind(1) - 500;
catch
    pk{r,1} = filename;
    pk{r,2} = NaN;
    pk(r,3:9) = num2cell(NaN);
    continue
end

% Generate picking matrix with signal to noise ratios
if ind(1) > minpick
    try
        rayt = [Ts:Ts:(length(signal)*Ts)];
        fill_pk
    catch
        pk{r,1} = filename;
        pk{r,2} = NaN;
        pk(r,3:9) = num2cell(NaN);
        continue
    end
else
    pk{r,1} = filename;
    pk{r,2} = NaN;
    pk(r,3:9) = num2cell(NaN);
    continue
end
test = find(abs(sig) == max(abs(sig)));
sigM(r)= test(1)*Ts;
end

% Removes late picking
for q = 1:size(recloc,1)
    [~,order] = sort(cell2mat(pk(:,2)), 'ascend');
    ind = find(diff(cell2mat(pk(order,2))) > 0.16e-4)+1;
    for p = 1:length(ind)
        r = order(ind(p));
        pk{r,2} = NaN;
        pk(r,3:9) = num2cell(NaN);
    end
end
end

```

```

% Plots waveforms and picks
pktimes(:, :, i) = pk;
if ismember(i, 1:length(event)) == 1 && figon == 1
    [~, order] = sort(cell2mat(pk(:, 2)), 'ascend');
    stp = max(max(abs(signal)));
    figure(2); yyaxis left; cla
    for jj = 1:length(order)
        Ts = 1/Fs;
        try
            csig = signal(:, order(jj));
            plot(csig+(stp*(jj-1)), 'k-'); hold on;
            scatter(round(pk{order(jj), 2}/Ts), (stp*(jj-1)), 'ro', 'filled')
        end
    end
    drawnow
end
end

```

7.1.2.5 WRITE VELOCITY MODEL

This writes the velocity model in the same structure as InSite

```

% Compile data
sepsurvey = diff(tempi);
ind = find(sepsurvey > 1e-4)+1;
ind = [1; ind; length(sepsurvey)+2];
vel = [];
rindex = 0;
for i = 2:length(ind)
    crows = [ind(i-1):1:ind(i)-1];
    if length(crows)~=size(recloc, 1)
        continue
    end
    rindex = rindex+1; cindex = 0;
    for r = 1:length(crows)

        for r2 = 1:length(crows)
            cindex = cindex + 1;
            if r == r2
                vel(rindex, cindex) = NaN;
            else
                try
                    if pktimes{r2, 3, crows(r)} < 2
                        vel(rindex, cindex) = NaN;
                        continue
                    end
                    dist = norm(recloc(r, :) - recloc(r2, :));
                    vel(rindex, cindex) = dist/pktimes{r2, 2, crows(r)};
                    qual(rindex, cindex) = pktimes{r2, 3, crows(r)};
                catch
                    vel(rindex, cindex) = NaN;
                end
            end
        end
    end
end

```

```

end
end

% Removes questionable picks
velim = [mean(vel(isnan(vel)==0))-2000 mean(vel(isnan(vel)==0))+2000];
for p = 1:size(vel,1)
    [~,order] = sort(vel(p,:), 'descend');
    ind = find(vel(p,order) > velim(2) | vel(p,order) < velim(1));
    vel(p,order(ind)) = NaN;

end

% Calculate velocity data
Vmax = max(vel');
Vmin = min(vel');
Vhet = Vmin./Vmax;

% write file
cHeader = {'vp' 'vs' 'PAni' 'Sani' 'Azimuth' 'Dip' 'Start_year' 'Start_month' ...
    'Start_day' 'Start_hour' 'Start_minute' 'Start_second' 'End_year' ...
    'End_month' 'End_day' 'End_hour' 'End_minute' 'End_second'}; %dummy header
commaHeader = [cHeader; repmat({','},1,numel(cHeader))]; %insert commas
commaHeader = commaHeader(:)';
textHeader = strjoin(cHeader, ','); %cHeader in text with commas
%write header to file
fid = fopen([testname, '_velocity model.csv'], 'w');
fprintf(fid, '%s\n', textHeader);
fclose(fid);
model = [];
model(:,1) = Vmax;
model(:,2) = ones(length(Vmax),1);
model(:,3) = Vhet;
model(:,4) = ones(length(Vmax),1);
model(:,5) = zeros(length(Vmax),1);
model(:,6) = 90.*ones(length(Vmax),1);
model = num2cell(model);

sepsurvey = diff(tempi);
ind = find(sepsurvey > 1e-4)+1;
ind = [1;ind;length(sepsurvey)+2];

index = 0;
modeltime = cell(1,1);
for i = 2:length(ind)
    crows = [ind(i-1):1:ind(i)-1];
    if length(crows)~=size(recloc,1)
        continue
    end
    try
        index = index +1;
        filename = sourcelocs{ind(i)-1,1};
        filename([9,16,20:end]) = '-';
        formatIn = 'yyyymmdd-HHMMSS-fff-----';
        modeltime{index,1} = str2num(filename(1:4));
        modeltime{index,2} = str2num(filename(5:6));
        modeltime{index,3} = str2num(filename(7:8));
        modeltime{index,4} = str2num(filename(10:11));
        modeltime{index,5} = str2num(filename(12:13));
    end
end

```

```

    modeltime{index,6} = str2num(filename(14:15));
    catch
        index = index-1;
        continue
    end
end

for i = 1:index

    if i == index
        modeltime{i,7} = modeltime{i,1}+1;
        modeltime{i,8} = modeltime{i,2};
        modeltime{i,9} = modeltime{i,3};
        modeltime{i,10} = modeltime{i,4};
        modeltime{i,11} = modeltime{i,5};
        modeltime{i,12} = modeltime{i,6};
    else
        modeltime{i,7} = modeltime{i+1,1};
        modeltime{i,8} = modeltime{i+1,2};
        modeltime{i,9} = modeltime{i+1,3};
        modeltime{i,10} = modeltime{i+1,4};
        modeltime{i,11} = modeltime{i+1,5};
        modeltime{i,12} = modeltime{i+1,6};
    end
end

model = [model(1:size(modeltime,1),:),modeltime];
ind = find(isnan(cell2mat(model(:,1)))) == 1);
model(ind,:) = [];
model{1,7} = model{1,7} - 1;

display('fin')
dlmwrite([testname,'_velocity model.csv'],model,'-append');
save pktimes_survey_m1.mat pktimes; save tempi_survey_m1.mat tempi

```

7.1.3 AE SOURCE LOCATION

Picks AE data (stored in folder sg2) using trained neural network. Data is then located using Time Difference of Arrival

7.1.3.1 VERSION

Version 1.0, 16th January 2019. Thomas King - First Version

7.1.3.2 PARAMETER CUSTOMISATION

Below are the suggested parameters to be modified. I don't recommend changing any of the code outside of these parameters.

```
clear all; close all

% This is the name of the picking model. I recommend to use folder names to
% avoid confusion as this testname is required when using the locating code
testname = 'DDS_NSA2';

figon = 1; % Display figures. 1 (on), 0 (off)
location = 1; % Locate data. 1 (on), 0 (off)

nPick = 4; % Minimum number of picks for source location

% Resamples waveforms to a shorter length. It can increase the speed of the
% code but time resolution is lost.
sigsamp = 2048;

% Minimum arrival time. Recommended at 10% of signal length
minpick = round(sigsamp/10);
```

7.1.3.3 COMPILE DATA

```
% Find origin time
dir1s = dir('sg2/*seg2');
index = 0; clear event
for i = 1:size(dir1s,1)
    event{i,1} = dir1s(i).name;
    filename = event{i};
    sourcelocs{i,1} = filename;
    filename([9,16,20:end]) = '-';
    formatIn = 'yyymmdd-HHMMSS-fff-----';
    tempi(i,1) = datenum(filename,formatIn);
end

% Find receiver positions
if exist('recloc') == 0
    cd sg2
    filename = event{1};
    [tracce,SR,Shot,X,n_samples,RL] = leggisg2(char(filename));
```



```

Ts = SR;
Fs = 1/SR;
for j = 1:length(RL)
    rec = strsplit(char(RL(j,:)));
    recloc(j,1) = str2num(rec{3}); % NED to XYZ
    recloc(j,2) = str2num(rec{2});
    recloc(j,3) = str2num(rec{4});
end
if max(max(recloc)) > 0.1
    recloc = recloc./1000;
end
cd ..
save recloc.mat recloc
else
    load recloc.mat
end

% Load velocity model. If it cannot find, sample velocity is set to 5500
try
    ls = dir('*velocity model.csv');
    velmodimport; clear velwin
    for i = 1:size(velocitymodel,1)
        velwin(i,1) = datenum(velocitymodel(i,7),velocitymodel(i,8),velocitymodel(i,9),...
            velocitymodel(i,10),velocitymodel(i,11),velocitymodel(i,12));
        velwin(i,2) = datenum(velocitymodel(i,13),velocitymodel(i,14),velocitymodel(i,15),...
            velocitymodel(i,16),velocitymodel(i,17),velocitymodel(i,18));
        velwin(i,3) = velocitymodel(i,1);
        velwin(i,4) = velocitymodel(i,3);
    end
catch
    velwin = [0, 1000000000, 5500, 1];
end

% Angles between receivers for velocity anisotropy
angles = [];
for i = 1:length(recloc)
    for j = 1:length(recloc)
        [~,ang] = rangeangle(recloc(i,:),recloc(j,:));
        ang = ang(2);
        angles(i,j) = ang;
    end
end

% Reset workspace
sources = []; error = [];
i = 1;
load(char(['pkmodel-',char(testname),'.mat']), 'p_mu1', 't_mu1', 'dtdnn_net')
pktimes = cell(size(recloc,1),9,length(event));

```

7.1.3.4 PICKING AND SOURCE LOCATION

```

i = i - 1;
bindex = 0; fstp2 = 0;
while i ~= size(event,1)

    % Reset

```

```

pk = cell(size(recloc,1),9); sigM = ones(size(recloc,1),1);
pk(:, :) = num2cell(NaN);
sourcestore = cell(1,5);
global cvel
cvel = []; filename = [];
Ts = 1/Fs;

% Load file and set current velocity
i = i + 1;
display(['Event ', num2str(i)])
filename = event{i};
etime = tempi(i);
ind = find(velwin(:,1) < etime & velwin(:,2) > etime);
if isempty(ind) == 1
    continue
else
    global cvel
    cvel = velwin(ind(1),:);
    cd sg2 % Load file
    try
        [tracce,SR,Shot,X,n_samples,RL] = leggi sg2(filename);
    catch
        cd ..
        pktimes(:, :, i) = pk;
        sourcestore{1,1} = filename;
        sourcestore(1,2:5) = num2cell(NaN);
        sourcelocs(i,1:5) = sourcestore;
        continue
    end
    signal = tracce; %(:,rec)
    cd ..
end

% Picking

% Sort waveforms according to amplitude
rsig = max(signal(1:length(signal)/2,:));
[~,ordersize] = sort(rsig, 'descend');
try
    if isempty(ordersize) == 1
        pktimes(:, :, i) = pk;
        sourcestore{1,1} = filename;
        sourcestore(1,2:5) = num2cell(NaN);
        sourcelocs(i,1:5) = sourcestore;
        continue
    end
catch
    [~,ordersize] = sort(rsig, 'descend');
end

% Begin
for o = 1:length(ordersize)

    % Reset
    Ts = 1/Fs;
    r = ordersize(o);
    display(num2str(o))
    sig = resample(signal(:,r), sigsamp, length(signal(:,r)));

```

```

Ts = Ts*(length(signal(:,r))/sigsamp);

% Get neural network input parameters
try
    % tic
    IFcontent
    %toc
catch
    pk{r,1} = filename;
    pk{r,2} = NaN;
    pk(r,3:9) = num2cell(NaN);
    continue
end
p1 = [con2seq(cc(1:length(sn))');con2seq(esig(1:length(sn)));...
      con2seq(sn(1:length(sn)))];

% Get arrival time
try
    pick_output_3
catch
    pk{r,1} = filename;
    pk{r,2} = NaN;
    pk(r,3:9) = num2cell(NaN);
    continue
end
pk1 = ind(1);

% Store arrival times
if pk1 > minpick
    try
        fill_pk
        if pk{r,3} > 800 % clipped data
            pk = cell(size(recloc,1),9); sigM = ones(size(recloc,1),1);
            pk(:, :) = num2cell(NaN);
            sourcestore = cell(1,5);
            pktimes(:, :, i) = pk;
            sourcestore{1,1} = filename;
            sourcestore(1,2:5) = num2cell(NaN);
            sourcelocs(i,1:5) = sourcestore;
            i = i+1;
            fstp2 = 1;
        end
    catch
        pk{r,1} = filename;
        pk{r,2} = NaN;
        pk(r,3:9) = num2cell(NaN);
        continue
    end
else
    pk{r,1} = filename;
    pk{r,2} = NaN;
    pk(r,3:9) = num2cell(NaN);
    continue
end

% Some traces don't work, this is part of a workaround
if fstp2 == 1
    fstp2 = 0;

```

```

        break
    end

end

% If arrival time is after maximum, set time to NaN
TOA = cell2mat(pk(:,2));
test = (sigM-TOA);
pk(test<0 | isnan(test) == 1,:) = num2cell(NaN);
test(test<0 | isnan(test) == 1) = NaN;
TOA(test<0 | isnan(test) == 1) = NaN;
pktimes(:, :, i) = pk;

% Locate AE

% Checks for minimum picks and if locating is turned on
if sum(cell2mat(pk(:,2))) > size(recloc,1)-nPick || location == 0
    sourcestore{1,1} = filename;
    sourcestore(1,2:5) = num2cell(NaN);
    sourcelocs(i,1:5) = sourcestore;
    continue
end

% Reset
restore = []; sourceopts = [];
p=1;

% Source inversion
[answer,res] = localize2(0,[0,0,0],TOA,...
    recloc,cvel,angles);
restore(p,:) = res; % Location residual
sourceopts(p,:) = answer % Source location
global calcdelays
global BUSHDelays

try
    ind = find(restore == min(restore));
    res = restore(ind(1));
    answer = sourceopts(ind(1),:);
catch
    sourcestore{1,1} = filename;
    sourcestore(1,2:5) = num2cell(NaN);
    sourcelocs(i,1:5) = sourcestore;
    continue
end

% Plots waveforms and arrival times
if ismember(i,1:length(event)) == 1 && figon == 1
    [~,order] = sort(cell2mat(pk(:,2)),'ascend');
    stp = max(max(abs(signal)));
    figure(2); yyaxis left; cla
    for jj = 1:length(order)
        Ts = 1/Fs;
        try
            csig = signal(:,order(jj));
            plot(csig+(stp*(jj-1)),'k-'); hold on;
            scatter(round(pk{order(jj),2}/Ts),(stp*(jj-1)),'ro','filled')
        end
    end
end

```

```

        end
        drawnow
    end

    % Compile results
    x0 = answer;
    sources = [sources;x0]; % Source location

    numpicks(i) = size(recloc,1)-ind(1); % Number of picks
    residual(i) = res; % Location residual
    snrrat(i) = max(cell2mat(pk(:,3))); % Signal to noise ratio

    sourcelocs{i,1} = filename; % Position
    sourcelocs{i,2} = x0(1);
    sourcelocs{i,3} = x0(2);
    sourcelocs{i,4} = x0(3);
    sourcelocs{i,5} = tempi(i);

    % Plot source locations
    if ismember(i,1:size(event,1)) == 1 && figon == 1
        figure(4); cla; hold on
        try
            % ind = find(snrrat > 2 & numpicks >= 9 & snrrat < 300 & residual < 2e-6);% &
            % residual > .01e-8);
            % sources = cell2mat(sourcelocs(ind,2:4));
            scatter3(sources(:,1),sources(:,2),sources(:,3),4,'ko','filled')
            alpha(0.3334)
            scatter3(sources(end,1),sources(end,2),sources(end,3),10,'ro','filled')
        catch
            continue
        end
        xlim([-0.02 0.02])
        ylim([-0.02 0.02])
        zlim([-0.05 0.05])

        pbaspect([4 4 10])
        ax = gca; % get the current axis
        ax.Clipping = 'on';
        view([0 0])
        camproj('perspective')
        xlabel('x')
        ylabel('y')
        xhandle = get(gca, 'xlabel');
        yhandle = get(gca, 'ylabel');
        thandle = get(gca, 'title');
        set([xhandle; yhandle; thandle], 'units', 'normal');
        drawnow
    end
end

```

7.1.3.5 CLEANUP AND SAVING

```

display('Removing NaN and Inf')
ind = find(sum(isnan(cell2mat(sourcelocs(:,2:4))))'
+sum(isinf(cell2mat(sourcelocs(:,2:4))))' == 0);
sourcelocs = sourcelocs(ind,:); % Sets events to only those found in the cylinder

```

```

pktimes = pktimes(:, :, ind);
tempi = tempi(ind);
numpicks = numpicks(ind);
residual = residual(ind);
snrrat = snrrat(ind);

display('Removing External Events')
% Remove external events
[X1 Y1 Z1] = cylinder(max([max(recloc(:, 1)) max(recloc(:, 2))])); % Makes a cylinder with
radius
Z1(2, :) = 0.1; % Sets cylinder height
shp = surf2patch(X1, Y1, Z1); % Makes it into a patch
X = shp.vertices(:, 1);
Y = shp.vertices(:, 2);
Z = shp.vertices(:, 3) - max(recloc(:, 3)); % Puts into the correct place
shp = alphaShape(X, Y, Z, 1, 'HoleThreshold', 10000); % Makes it into a shape
ind =
find(inShape(shp, cell2mat(sourcelocs(:, 2)), cell2mat(sourcelocs(:, 3)), cell2mat(sourcelocs(
(:, 4))) == 1);
sourcelocs = sourcelocs(ind, :); % Sets events to only those found in the cylinder
pktimes = pktimes(:, :, ind);
tempi = tempi(ind);
numpicks = numpicks(ind);
residual = residual(ind);
snrrat = snrrat(ind);

save pktimes_m1.mat pktimes; save sourceloc_m1.mat sourcelocs; save tempi_m1.mat tempi;
save error_m1.mat numpicks residual snrrat

```

7.1.4 AUTOMATED WAVEFORM PICKING (IFCONTENT)

This code picks the input waveform. Input data are simulated and an output model (yp) is produced. Signal onset is determined from this output.

7.1.4.1 SIMULATE MODEL

```
yp = sim(dtdnn_net,p1);
yp = cell2mat(yp);
yp = smooth(yp,round(sigsamp/40)); % Smooth model output
```

7.1.4.2 SET PICKING LIMITS FOR TRAINING OR LOCATION CODE

```
if o ~= 0
    rayt = [Ts:Ts:(sigsamp*Ts)];
end
if o > 1
    adj = round(pk{ordersize(1),2}/Ts);
    if isnan(adj) == 0
        test = 'adj:adj+round(sigsamp/5.5)';
        test2 = 'adj';
    else
        test = 'minpick:(length(yp))';
        test2 = 'minpick';
    end
else
    test = 'minpick:(length(yp))';
    test2 = 'minpick';
end
```

7.1.4.3 DETERMINE WINDOW AROUND TRANSITION BETWEEN SIGNAL AND NOISE

```
if max(yp(eval(test))) > 0
    lim = 0.8; fstp = 0;
    while fstp == 0
        try
            ind = find(yp(eval(test)-1) > ...
                lim*max(yp(eval(test)-1)) & ...
                yp(eval(test)-1) < 1.5)+eval(test2);
            try
                ind = ind(ind < length(sig)); ind = ind(1);
            catch
                ind = ind(ind < sigtest); ind = ind(1);
            end
            fstp = 1;
        catch
            lim = lim-0.1;
            if lim <= 0
                fstp = 2;
                break
            end
        end
    end
```

```

        fstp = 0;
        continue
    end
end
if fstp == 2
    pot
end
else
    ind = diff([0.8*max(yp(eval(test))-1),max(yp(eval(test))-1)]);
    ind = find(yp(eval(test))-1 > max(yp(eval(test))-1)+ind)+eval(test2);
    ind = ind(ind < length(sig)); ind = ind(1);
end

ind = find(yp(eval(test2):ind) < mean([yp(ind) min(yp(eval(test2):ind))]))+eval(test2);

```

7.1.4.4 PICKS HIGHEST SIGNAL TO NOISE RATIO

```

snnew = [];
for p = ind(end)-200:length(ind)
    try
        snnew(p) = rms(sig(ind(p):ind(p)+100))/rms(sig(ind(p)-100:ind(p)));
    end
end

try
    indbck = ind;
    ind = ind(find(snnew == max(snnew)));
    pick = ind(end);
catch
    ind = indbck;
    ind = find(abs(yp(ind)) == min(abs(yp(ind)))) + ind(1);
    pick = ind(1);
end

```


7.2 FOCAL MECHANISMS

7.2.1 FOCAL MECHANISM SOLUTIONS

Solves for focal mechanism solutions using first motion polarity amplitudes. Measurements are projected onto spheres and iteratively rotated minimising the fit to idealised mechanisms. I apologise for the state of 'eventdata'.

7.2.1.1

```
clear all; close all;
warning off all
```

7.2.1.2 INITIALISATION

```
load sourceloc_m1.mat
load pktimes_m1.mat
load recloc.mat

compiledata = 1; % Set to 1 to compile waveform data
compilemodel = 1; % Set to 1 to generate fitting models
```

7.2.1.3 COMPILE DATA

```
if compiledata == 1
    index = 0;
    sources = cell2mat(sourcelocs(:,2:5));
    cd sg2
    for e = 1:size(sourcelocs,1)
        index = index+1;
        eventdata{index,1} = sourcelocs(e,1);
        eventdata{index,2} = sources(e,4);
        eventdata{index,3} = sources(e,1:3);

        clear azimuth takeoff
        for r = 1:size(recloc,1)

            % Azimuth and takeoff
            receiver = recloc(r,:);
            source = eventdata{index,3};
            [~,ang] = rangeangle(receiver',source');
            azimuth(r) = ang(1);
            takeoff(r) = ang(2);

        end

        eventdata{index,4} = azimuth;
        eventdata{index,5} = takeoff;
    try
        signal = leggisg2(char(eventdata{index,1}));
```

```

catch
    index = index - 1;
    continue
end
eventdata{index,6} = signal;

ind = find(cellfun(@isempty, pktimes(:,2,e))==1);
pktimes(ind,2,e) = num2cell(0);

eventdata{index,7} = cell2mat(pktimes(:,2,e));

end
cd ..
save focaleventdata.mat eventdata -v7.3
else
load focaleventdata.mat
end

```

7.2.1.4 GENERATE FITTING SPHERES

```

if compilemodel == 1

% Generate blank sphere
[x1,y1,z1] = sphere(80);
x = x1(:);
y = y1(:);
z = z1(:);

% Double Couple Quad
fitDCQ = [x y z];
ind = find(fitDCQ(:,2) > 0 & fitDCQ(:,3) > 0);
fitDCQ(ind,4) = 1;
ind = find(fitDCQ(:,2) < 0 & fitDCQ(:,3) < 0);
fitDCQ(ind,4) = 1;
ind = find(fitDCQ(:,2) < 0 & fitDCQ(:,3) > 0);
fitDCQ(ind,4) = -1;
ind = find(fitDCQ(:,2) > 0 & fitDCQ(:,3) < 0);
fitDCQ(ind,4) = -1;

for i = 1:size(fitDCQ,1)
    [Idx,D] = knnsearch(fitDCQ(i,1:3),fitDCQ(:,1:3));
    ind = find(D < 0.5);
    val = fitDCQ(ind,4);
    val = val(find(isnan(val) == 0));
    fitDCQ(i,5) = mean(val);
end

figure(1); subplot_tight(1,3,2,[0.04,0.01]);
surf(x1,y1,z1,reshape(fitDCQ(:,4),size(x1,1),size(x1,2)), 'linestyle', 'none');
set(gcf, 'color', 'white')
pbaspect([1 1 1])
set(gca, 'xtick', [])
set(gca, 'xticklabel', [])
set(gca, 'ytick', [])
set(gca, 'yticklabel', [])
set(gca, 'box', 'off')

```

```

set(gca,'ztick',[])
set(gca,'zticklabel',[])
title('S-type')
axis off

% CLVD
fitCLVD = [x y z];
[X1 Y1 Z1] = cylinder(0.75);
Z1(2,:) = 1;
shp = surf2patch(X1,Y1,Z1);
X1 = shp.vertices(:,1);
Y1 = shp.vertices(:,2);
Z1 = shp.vertices(:,3)-1;
ind = find(Z1 == 0);
X1 = vertcat(X1,X1(ind));
Y1 = vertcat(Y1,Y1(ind));
Z1 = vertcat(Z1,Z1(ind)+1);
XYZold = [X1 Y1 Z1]; XYZold = XYZold'; x0=[0 0 0].'; u=[0 1 0].'; deg=90;
[XYZnew, R, t] = AxelRot(XYZold, deg, u, x0); XYZnew = XYZnew';
X1 = XYZnew(:,1); Y1 = XYZnew(:,2); Z1 = XYZnew(:,3);
shp = alphaShape(X1,Y1,Z1,1,'HoleThreshold',15);
ind = find(inShape(shp,fitCLVD(:,1),fitCLVD(:,2),fitCLVD(:,3)) == 1);
fitCLVD(:,4) = 1;
fitCLVD(ind,4) = -1;

for i = 1:size(fitCLVD,1)
    [Idx,D] = knnsearch(fitCLVD(i,1:3),fitCLVD(:,1:3));
    ind = find(D < 0.5);
    val = fitCLVD(ind,4);
    val = val(find(isnan(val) == 0));
    fitCLVD(i,5) = mean(val);
end

figure(1); subplot_tight(1,3,1,[0.04,0.01]);
surf(x1,y1,z1,reshape(fitCLVD(:,4),size(x1,1),size(x1,2)),'linestyle','none');
view([0 30]); pbaspect([1 1 1])
set(gcf,'color','white')
set(gca,'xtick',[])
set(gca,'xticklabel',[])
set(gca,'ytick',[])
set(gca,'yticklabel',[])
set(gca,'box','off')
set(gca,'ztick',[])
set(gca,'zticklabel',[])
title('C-type')
axis off

% Mixed Mode
fitMM = [x y z];
ind = find(fitMM(:,3) < 0.1 & fitMM(:,3) > -0.1);
fitMM(:,4) = 1;
fitMM(ind,4) = -1;

for i = 1:size(fitMM,1)
    [Idx,D] = knnsearch(fitMM(i,1:3),fitMM(:,1:3));
    ind = find(D < 0.5);
    val = fitMM(ind,4);
    val = val(find(isnan(val) == 0));

```

```

        fitMM(i,5) = mean(val);
    end

    figure(1); subplot_tight(1,3,3,[0.04,0.01]);
    surf(x1,y1,z1,reshape(fitMM(:,4),size(x1,1),size(x1,2)),'linestyle','none');
    view([0 30]); pbaspect([1 1 1])
    title('T-type')
    set(gcf,'color','white')
    set(gca,'xtick',[])
    set(gca,'xticklabel',[])
    set(gca,'ytick',[])
    set(gca,'yticklabel',[])
    set(gca,'box','off')
    set(gca,'ztick',[])
    set(gca,'zticklabel',[])
    axis off

    save focalmechmodel.mat fitDCQ fitCLVD fitMM
end

```

7.2.1.5 DATA PREP

```

clear all; close all

Load focal eventdata.mat
Load focalmechmodel.mat

Fs = 1000000;           % Sampling frequency
T = 0.1/(Fs);          % Sampling period
L = 2048;               % Length of signal
rayt = (0:L-1)*T;      % Time vector

wn = ([0.0001 20]/1000); %frequency band
[z,p,k] = butter(6,wn,'stop'); %butter filter
[sos,g] = zp2sos(z,p,k); % Convert to SOS form
Hd3 = dfilt.df2tsos(sos,g); % Create a dfilt object

```

7.2.1.6 PICK FIRST MOTIONS

```

fmstore = [];
for e = 1:size(eventdata,1)
    display(num2str(size(eventdata,1) - e +1))
    signal = eventdata{e,6};
    ptimes = eventdata{e,7};
    if length(ptimes) == size(signal,2)
        [~,order] = sort(max(abs(signal)),'descend');
        amp = zeros(1,length(order)); error = amp; pol = amp;
        for o = 1:size(signal,2)
            r = order(o);
            csignal = filter(Hd3,signal(:,r)); csignal = csignal - mean(csignal);
            cpick = round((ptimes(r))/T); %*10
            if cpick-100 <= 0 || isnan(cpick) == 1
                amp(r) = 0;
                pol(r) = 0;
                error(r) = 0;
            end
        end
    end
end

```

```

        continue
    end
    env = smooth(envelope(csignal,1,'rms'),5);
    noise = max(env(1:cpick));
    cropenv = env(cpick-100:cpick+100);
    scsig = smooth(csignal,5);
    for i = 1:length(csignal)-cpick
        if i < cpick
            continue
        end
        if env(i) > 1.1*noise && env(i+3) < env(i)
            amp(r) = csignal(i);
            if amp(r) < 0; pol(r) = -1; else; pol(r) = 1; end
            error(r) = abs(diff([i cpick]));
            break
        end
    end
    eventdata{e,8} = amp; % First motion amplitude
    eventdata{e,9} = pol; % First motion polarity
    eventdata{e,10} = error; % Difference of onset to first motion pick
    fmstore = [fmstore,amp];
end
end

```

7.2.1.7 COMPILE POLARITY DATA

```

pol = [];
for e = 1:size(eventdata,1)
    cpol = eventdata{e,9};
    if isempty(cpol) == 0
        pol = [pol;cpol];
    else
        pol = [pol;zeros(1,length(order)).*NaN];
    end
end
end

% Reset
sources = cell2mat(eventdata(:,3));
chk = [];
e = 1;

```

7.2.1.8 MECHANISM INVERSION

```

tic
while e ~= size(eventdata,1)+1
    display(num2str(size(eventdata,1) - e +1))

    % Minimum of 8 polarity measurements
    if sum(abs(pol(e,pol(e,:) ~= 0))) < 8
        e = e+1;
        continue
    end

    ind = e;

```

```

eventdata{e,11} = ind;

% Compile measurements
th = cell2mat(eventdata(ind,4));
rho = cell2mat(eventdata(ind,5));
amp = cell2mat(eventdata(ind,8));
th = reshape(th,size(th,1)*size(th,2),1);
rho = reshape(rho,size(rho,1)*size(rho,2),1);
amp = reshape(amp,size(amp,1)*size(amp,2),1);
amp = amp./max(abs(amp));

% Models to test
global modlist
modlist = {'fitCLVD','fitMM','fitDCQ'};

% Compile input data
[x,y,z] = sph2cart(th,rho,1);
modS = [x(:) y(:) z(:) amp zeros(length(x(:)),1)]; % Measured
global models
for x = 1:size(modlist,2)
    models{x} = eval(modlist{x}); % Modeled
end

% Reset
storebck = cell(11,size(modlist,2));
residualbck = [];
mechsolbck = [];

% Inversion
for x = 1:length(modlist)
    [output] = focmech(modS,x); % x is current model
    store = output{3};
    storebck(:,x) = store(:,x); % Inversion results
    residualbck(x) = output{2}; % Residual

end
store = storebck;
eventdata{e,13} = store;

% Mechanism is model with lowest residual
try
    order = find(residualbck == min(residualbck));

    eventdata{e,14} = store{1,order(1)};
catch
    eventdata{e,14} = [];
end

display(eventdata{e,14})
e = e+1;

% Autosave
if toc > 3000
    save eventdataamech_m_residual.mat eventdata -v7.3
    tic
end

% Event percentages

```

```
figure(12); cla;
A = eventdata(:,14);
ind = find(~cellfun(@isempty,A));
A = A(ind);
[u,~,n] = unique(A(:));
B = accumarray(n, 1, [], @sum);
bar(B)
set(gca, 'XTickLabel',u)
drawnow
end

save eventdatamech_m1_residual.mat eventdata -v7.3
```

7.2.2 MECHANISM PROBABILITY DENSITY PLOTS

This code plots the focal mechanisms as probability densities against time or strain.

7.2.2.1 VERSION

Version 1.0, 27th January 2019. Thomas King - First Version

7.2.2.2 PARAMETER CUSTOMISATION

Below are the suggested parameters to be modified. I don't recommend changing any of the code outside of these parameters.

```
clear all; close all

% Plotting Parameters
pressure = '40 MPa'; % This is the title of the plot
TorS = 2; % time or strain 1 or 2
averagepolarity = 0; % 1 on 0 off
ampthresh = 0.05; % Seperate mechanisms with an amplitude threshold
saving = 1;

% Plotting colours. Have the same number of colours as mechanisms
C = brighten(parula(3),.25);
C1 = C(1,:);
C2 = brighten(C(2,:),-.1);
C3 = C(3,:);
C = [C1;C2;C3];

% Smoothing Parameters
pdfsmooth = 40; % PDF plot smoothing
nEvents = 10; % Event windowing

% Time Corrections
timecorr = 0;
```

7.2.2.3 COMPILE DATA

```
% load mechanical data
stress_strain

% Load and order data
load eventdatamech_m1_residual.mat
[~,order] = sort(cell2mat(eventdata(:,2)));
eventdata = eventdata(order,:);

% Mechanism list
modlist = {'fitCLVD','fitDCQ','fitMM'};

% Compile mechanism data
ind = [];
load focalmechmode1.mat fitMM
```



```

for i = 1:size(eventdata,1)

    % Skip unsolved mechanisms
    if isempty(eventdata{i,14}) == 1 || isempty(eventdata{i,2}) == 1
        continue
    end

    % Time correction
    eventdata{i,2} = eventdata{i,2} - start - timecorr;
    eventtime(i) = eventdata{i,2};

    % Load data for event
    store = eventdata{i,13}; % Fitting parameters
    amp = eventdata{i,8}; % Polarity amplitude
    pol = eventdata{i,9}; % Polarity direction
    avepol = mean(pol(pol~=0)); % Average Polarity

    % Maximum amplitude of event
    csig = eventdata{i,6}; csig = csig(:,rms(csig)==max(rms(csig)));
    csig = log(max(abs(csig)));

    % Fitting
    test = cell2mat(store(5:8,:))';
    test(:,[1,3]) = 1./test(:,[1,3]);
    test2(:,1) = test(:,1).*test(:,2);
    test2(:,2) = test(:,3).*test(:,4);
    [~,order] = sort(test2(:,2),'descend');
    eventdata{i,16} = test(order(1),3);
    eventdata{i,17} = test(order(1),4);
    eventdata{i,18} = test2(order(1),2);
    fitvalue(i) = test2(order(1),2);

    % if fitvalue(i) < 2
    %     continue
    % end

    % Amplitude data
    at2(i,find(ismember(modlist,eventdata(i,14)) == 1)) = csig;

    at3(i) = csig;

    % Average Polarity Fitting
    if averagepolarity == 1
        if avepol < -0.25
            eventdata{i,14} = modlist{4};
        elseif avepol > 0.25
            eventdata{i,14} = modlist{1};
        elseif avepol >= -0.25 && avepol <= 0.25
            eventdata{i,14} = modlist{3};
        end
    end

    % Removes skipped data
    ind = [ind,i];
    eventdata{i,15} = length(ind);

    % Converts event time to strain value
    straintime(i,1) = mean(deform(abs(deform(:,1) - eventdata{i,2}) ==

```

```

min(abs(deform(:,1) - eventdata{i,2})),2));

end

% Cropping
eventdata = eventdata(ind,:);
straintime = straintime(ind);
aT2 = aT2(ind,:);
fitvalue = fitvalue(ind);
aT3 = aT3(ind);
eventtime = eventtime(ind);

```

7.2.2.4 PLOTTING

```

% Use this to choose specific events
indE = [1:1:size(eventdata,1)];

% Amplitude thresholding
mechsep = 2.*[1:1:size(modlist,2)]-1; ls = []; ls2 = [];
for j = 1:length(indE)
    % Compile event data
    ls(j,1) = eventdata{indE(j),2}; % Event time
    ls(j,2) = find(ismember(modlist,eventdata(indE(j),14)) == 1); % Event mechanism
    ls(j,3) = aT3(indE(j));

    % Sets an amplitude threshold for each mechanism type
    aT =
min(aT2(aT2(eventtime<mean(stress(stress(:,2))==max(stress(:,2)),1)),ls(j,2))~=0,ls(j,2)))
...
    +
ampthresh*(range(aT2(aT2(eventtime<mean(stress(stress(:,2))==max(stress(:,2)),1)),ls(j,2))
~=0,ls(j,2))));

    % Separates mechanism by amplitude
    if ls(j,3) < aT
        ls2(j) = mechsep(ls(j,2));
    else
        ls2(j) = mechsep(ls(j,2))+1;
    end
end
ls(:,2) = ls2;

% Calculate probability densities
test = [];
for i = 1:max(mechsep)+1

    % Strain
    if Tors == 2
        gridx1 = [straintime(indE(1):nEvents:end,1);max(max(deform(:,2)))]];
        x = straintime(ls(:,2) == i,1);
        try
            [f,xi,bw] = ksdensity(x,gridx1,'bandwidth',pdfsmooth*0.001);
        catch
            f = zeros(length(gridx1),1);
        end
    end
end

```

```

% Time
else
    gridx1 = 1s(indE(round(nEvents/2):nEvents:end),1);
    x = 1s(1s(:,2) == i,1);
    try
        smoot = find(abs(deform(:,2)-(pdfsmooth*0.001)) == min(abs(deform(:,2)-
(pdfsmooth*0.001)))));
        [f,xi,bw] = ksdensity(x,gridx1,'bandwidth',deform(smoot(1),1));
    catch
        f = zeros(length(gridx1),1);
    end
end
test(:,i) = f;
end

% Converts density to a percentage
test2 = [];
for i=1:size(test,1)
    for k = 1:max(mechsep)+1
        test2(i,k) = test(i,k)/sum(test(i,:));
    end
end

% Plots percentage data
figure(10); %title(pressure);
left_color = [0 0 0]; right_color = [0 0 0];
set(figure(10),'defaultAxesColorOrder',[left_color; right_color]);
yyaxis left; cla; hold on;
h = area(xi,test2.*100,'linewidth',1.1);

% Colours
h(1).FaceColor = c1;
h(2).FaceColor = brighten(c1,0.5);
h(3).FaceColor = c2;
h(4).FaceColor = brighten(c2,0.8);
h(5).FaceColor = c3;
h(6).FaceColor = brighten(c3,0.9);%

% Plot stuff
xt = get(gca, 'YTick');
set(gca, 'FontSize', 30, 'Ycolor', 'k')
xt = get(gca, 'XTick');
set(gca, 'FontSize', 30)
ylabel('Relative mechanism percentage')
xlabel('Strain (%)')
set(gcf, 'color', 'white')
ylim([0 100])

% Plots mechanical data
yyaxis right; cla; hold on;
hold on
plot(deform(:,Tors),(stress(:,2)),'-','color',[0.5 0.5 0.5],'linewidth',4);
plot(deform(:,Tors),(stress(:,2)),'k-','linewidth',3);

% Adds a box
plot([0 max(deform(:,Tors)) max(deform(:,Tors)) 0 0],...
[0 0 1.1*max(stress(:,2)) 1.1*max(stress(:,2)) 0],'k-','linewidth',2)

```

```

% Plot stuff
ylabel('Differential stress (MPa)')
ylim([0 1.1*max(stress(:,2))])
xt = get(gca, 'YTick');
set(gca, 'FontSize', 30, 'Ycolor', 'k')
xt = get(gca, 'XTick');
set(gca, 'FontSize', 30)
pbaspect([4 2 1])
if Tors == 1
    xlim([0 max(deform(:,Tors))])
else
    xlim([0 max(deform(:,Tors))])
end

badj = [0.7 0.95];
B = badj.*deform(round(mean(find(max(stress(:,2))==stress(:,2))),2));

for i = 1:length(B)
    yyaxis left
    plot([B(i) B(i)], [0 100], 'w-', 'linewidth', 4)
    plot([B(i) B(i)], [0 100], 'k-', 'linewidth', 3)
end

if saving == 1
    set(gcf, 'units', 'normalized', 'outerposition', [0 0 1 1])
    %myaa('publish')
    saveas(gcf, 'mechprobability.png')
end

```

7.2.3 MECHANISM INVERSION

Measurement spheres are iteratively rotated to minimise the fit with idealised models

```
function [output] = focmech(mods,number)

global mechso1
global modFIT
global modnum
modFIT = mods;
modnum = number;

Guess = [0 0 0 0];

options = optimset('MaxFunEvals',1000);

[answer,res,store] = fminsearchbnd(@ellipseMerit,Guess,[0 0 0 -360],[1 1 1 360],options);

global param

output = param;

% Residual calculation
function [res] = ellipseMerit(s)

global modFIT

[store] = ellipseFun(s, modFIT);

test = cell2mat(store(5:8,:))';
test(:,[1,3]) = 1./test(:,[1,3]);
test2(:,1) = test(:,1).*test(:,2);
test2(:,2) = test(:,3).*test(:,4);
test2(:,2) = 1./test2(:,2);

answer = find(test2(:,2)~=0);
answer = answer(test2(answer,2) == min(test2(answer,2)));
res = test2(answer,2);
if isempty(res)
    res = 10000;
end
global param
param = {answer,res,store};

% Model iteration
function [store] = ellipseFun(s, mods)

%store = [];

global modFIT
global models
global modnum
for x = modnum%1:length(models)
```

```

fitC = models{x};

if mean(s(:,1:4)) ~= 0
    XYZold = fitC(:,1:3); XYZold = XYZold'; x0=[0 0 0].'; u=[s(:,1) s(:,2)
s(:,3)].'; deg=s(:,4);
    [XYZnew, R, t] = AxelRot(XYZold, deg, u, x0); fitC(:,1:3) = XYZnew';
end

modS = modFIT;
IDX = knnsearch(fitC(:,1:3),modS(:,1:3));
modC = [fitC(IDX,:), modS(:,4)];
modC(modC(:,4) > 0 & modC(:,5) > 0,6) = 1;
modC(modC(:,4) < 0 & modC(:,5) < 0,6) = 1;
modC(1:size(modS,1),7) = 1;

global mechsol
mechsol = s;

test = []; test2 = [];
test(1) = sum((modC(:,4) - modC(:,5)).^2);
test(2) = sum(modC(:,6))/size(modC,1);
try
    test(3) = sum((modC(1:size(modS,1),4) -
(modC(1:size(modS,1),5)./max(abs(modC(1:size(modS,1),5))))).^2);
    test(4) = sum(modC(1:size(modS,1),7))/size(modS,1);
catch
    test(3) = 10;
    test(4) = 0;
end
global modlist
store{1,x} = modlist{x};
store{2,x} = [];
store{3,x} = [s(:,1) s(:,2) s(:,3) s(:,4)];
store{4,x} = [];
store{5,x} = test(1);
store{6,x} = test(2);
store{7,x} = test(3);
store{8,x} = test(4);
store{9,x} = [];
store{10,x} = [];
store{11,x} = modC;

end

```

7.2.4 MECHANISM ORIENTATIONS AND DIVERGENCE PLOTS

This code plots the orientations of the mechanisms in different forms.

7.2.4.1 VERSION

Version 1.0, 27th January 2019. Thomas King - First Version

7.2.4.2 PARAMETER CUSTOMISATION

Below are the suggested parameters to be modified. I don't recommend changing any of the code outside of these parameters.

```
clear all; close all; warning off all

% Animation and saving
anim = 0; % set to 1 to turn on animation plots for divergence maps
saving = 0; % set to 1 to save plots as they generate

% Time Corrections
timecorr = 132;

% Fracture plot options
sz = 0.4e-3; % Fracture display size

% Divergence map options
gstp = 0.005; % Gridding step

% Mechanism list
modlist = {'fitCLVD', 'fitDCQ', 'fitMM'};

% Mechanism colours
C = brighten(parula(3), .25);
C1 = C(1,:);
C2 = brighten(C(2,:), -.1);
C3 = C(3,:);

% Data windowing
wtype = 0; % Set to 0 for UCS, set to 1 for strain
badj = [0.7 0.95]; % Data windowing as a percent of UCS
wind = 0.005; % Data windowing as a value of strain
winmax = 0.1; % Maximum width of window in strain if using animation
numevents = 50; % minimum number of events per animation window
```

7.2.4.3 COMPILE DATA

```
% load mechanical data
stress_strain

% Load and order data
load eventdatamech_ml_residual.mat
load focalmechmodel.mat
```

```
[~,order] = sort(cell2mat(eventdata(:,2)));
 eventdata = eventdata(order,:);
 etime = cell2mat(eventdata(:,2)) - start - timecorr;
```

7.2.4.4 WINDOWING

```
if anim == 1
    if wtype == 1
        badj = [min(deform(:,2)):wind:max(deform(:,2))];
        B = badj;
    elseif wtype == 0
        B = badj.*deform(round(mean(find(max(stress(:,2))==stress(:,2)))),2);
    end
    for j = 1:length(B)
        B3(j) = mean(deform(abs(deform(:,2) - B(j)) == min(abs(deform(:,2) - B(j))),1));
        B(j) = find(abs(etime - B3(j)) == min(abs(etime - B3(j))));
    end
    B = unique(B);
    B = [1,B,size(eventdata,1)];
    B2 = []; index = 0; strainave = [];
    for i = 1:length(B)
        index = index+1;
        try
            stp = 1;
            B2(index,:) = [B(i-stp),B(i+stp)];
            while diff(B2(index,:)) < numevents
                B2(index,:) = [B(i-stp),B(i+stp)];
                strainave(index) = mean([badj(i-stp),badj(i+stp)]);
                stp = stp + 1;
                if diff([badj(i-stp),badj(i+stp)]) > winmax || i+stp > length(B)
                    break
                end
            end
        catch
            index = index-1;
        end
    end
    ind = find(diff(B2')>100);
    badj = badj(ind); B2 = B2(ind,:); strainave = strainave(ind(ind<length(strainave)));
    B2(1,1) = 1;
    B2(end,end) = size(eventdata,1);
else
    if wtype == 1
        badj = [0:wind:max(deform(:,2))];
        B = badj;
    elseif wtype == 0
        B = badj.*deform(round(mean(find(max(stress(:,2))==stress(:,2)))),2);
    end
    for j = 1:length(B)
        B3(j) = mean(deform(abs(deform(:,2) - B(j)) == min(abs(deform(:,2) - B(j))),1));
        B(j) = find(abs(etime - B3(j)) == min(abs(etime - B3(j))));
    end
    B = [1,B,size(eventdata,1)]; index = 0;
    for i = 1:length(B)-1
        try
            index = index + 1;
```



```

    B2(i,:) = [B(i),B(i+1)];
    strainave(i) = mean([badj(i),badj(i+1)]);
    catch
        index = index -1;
    end
end
ind = find(diff(B2')>100);
B2 = B2(ind,:); strainave = strainave(ind(ind<length(strainave)));
B2(1,1) = 1;
B2(end,end) = size(eventdata,1);
end

```

7.2.4.5 CALCULATE ORIENTATIONS

```

% Orientations for each mechanism
tensile = cell(1,1,1); ind = [];
collapse = tensile;
shear = tensile;
tindex = 0; cindex = 0; sindex = 0;
tlist = ''; clist= '';
tmech = []; smech = []; cmech = [];

for i = 1:size(eventdata,1)

    % Skip unsolved mechanisms
    if isempty(eventdata{i,14}) == 1 || isempty(eventdata{i,2}) == 1
        continue
    end

    % Time correction
    eventdata{i,2} = eventdata{i,2} - start - timecorr;
    eventtime(i) = eventdata{i,2};

    % Fitting
    store = eventdata{i,13};
    test = cell2mat(store(5:8,:))';
    test(:,[1,3]) = 1./test(:,[1,3]);
    test2(:,1) = test(:,1).*test(:,2);
    test2(:,2) = test(:,3).*test(:,4);
    [~,order] = sort(test2(:,2),'descend');

    % Orientation prep
    rot = store{3,order(1)};
    rot = store{3,order(1)};
    rotangle(i) = NaN;
    azangle(i) = NaN;
    Cang = [NaN NaN];

    % Mechanism prep
    loc = eventdata{i,3};
    fitMOD = eval(eventdata{i,14}); % Load mechanism model
    fit = fitMOD(:,1:3);
    XYZold = fit; XYZold = XYZold'; x0=[0 0 0].'; u=[rot(1) rot(2) rot(3)].'; deg=rot(4);
    [XYZnew, R, t] = AxelRot(XYZold, deg, u, x0); fit = XYZnew';

    ind1 = find(fitMOD(:,3) == max(fitMOD(:,3)))';

```

```

ind2 = find(fitMOD(:,3) == min(fitMOD(:,3)))';
ind3 = find(fitMOD(:,2) == max(fitMOD(:,2)))';
ind4 = find(fitMOD(:,2) == min(fitMOD(:,2)))';
ind5 = find(fitMOD(:,1) == max(fitMOD(:,1)))';
ind6 = find(fitMOD(:,1) == min(fitMOD(:,1)))';

if mean(ismember(eventdata{i,14},modlist{3})) == 1
    etype(i) = 3;
    ind1 = []; ind2 = [];
elseif mean(ismember(eventdata{i,14},modlist{2})) == 1
    etype(i) = 2;
    ind5 = []; ind6 = [];
elseif mean(ismember(eventdata{i,14},modlist{1})) == 1
    etype(i) = 1;
    ind5 = []; ind6 = [];
end

% Generate surface for rotated mechanism
p = [];
for pp = 1:6
    try
        p = [p;(fit(eval(['ind',num2str(pp)]),:))];
    catch
        p = [p;(fit(eval(['ind',num2str(pp)]),:))'];
    end
end
x = p(:,1); y = p(:,2); z = p(:,3);
xq = linspace(min(x), max(x),10);
yq = linspace(min(y), max(y),10);
[X,Y] = meshgrid(xq,yq);
Z = griddata(x,y,z, X, Y, 'cubic');
corn = [x,y,zeros(size(z,1),1)];

% Generate surface for non-rotated mechanism
p = [];
for pp = 1:6
    try
        p = [p;fitMOD(eval(['ind',num2str(pp)]),1:3)];
    catch
        p = [p;fitMOD(eval(['ind',num2str(pp)]),1:3)'];
    end
end
x = p(:,1); y = p(:,2); z = p(:,3);
xq = linspace(min(x), max(x),10);
yq = linspace(min(y), max(y),10);
[X1,Y1] = meshgrid(xq,yq);
Z1 = griddata(x,y,z, X1, Y1, 'cubic');
corn2 = [x,y,zeros(size(z,1),1)];

% Calculate angular difference between the two surfaces
[nx1 ny1 nz1] = surfnorm(X,Y,Z);
[nx2 ny2 nz2] = surfnorm(X1,Y1,Z1+10);
beta = acosd(dot([nx2(:),ny2(:),nz2(:)]',[nx1(:),ny1(:),nz1(:)]'));
alpha = atan2d(nx1(:),ny1(:));
alpha = mean(alpha(isnan(alpha)==0));
Cang(1) = alpha;
Cang(2) = 90-mean(beta(isnan(beta)==0));

```

```

% Angular corrections
if Cang(1) < 0
    Cang(1) = 180 + abs(diff([Cang(1) -180]));
end
if ismember(eventdata{i,14},modlist{3}) == 1
    Cang(1) = Cang(1) + 90; % Tensile correction
end
if Cang(1) > 360
    Cang(1) = 0 + abs(diff([Cang(1) 360]));
end

azangle(i) = Cang(1); % Fracture Azimuth
rotangle(i) = 90 - abs(Cang(2)); % Fracture Dip

% Set window for current event
if badj ~= 0

    tind = find(B2(:,1) <= i & B2(:,2) >= i);

    %     tind = find(B < i);
    %     try
    %         tind = tind(end);
    %     catch
    %         tind = 1;
    %     end
else
    tind = find(B2(:,1) <= i & B2(:,2) >= i);
end

% Generate fracture ellipsoids
C = loc; % center of circle
R = 1; % Radius of circle
teta=0:0.01:2*pi ;
X=R*cos(teta);
Y=R*sin(teta) ;
Z = zeros(size(X));
X = X.*4;
Y = Y./2;
fit = [X',Y',Z'];

% Rotations
XYZold = fit; XYZold = XYZold'; x0=[0 0 0].'; u=[1 0 0].'; deg = 90;
[XYZnew, R, t] = AxelRot(XYZold, deg, u, x0); fit = XYZnew';
XYZold = fit; XYZold = XYZold'; x0=[0 0 0].'; u=[0 1 0].'; deg = abs(Cang(2));
[XYZnew, R, t] = AxelRot(XYZold, deg, u, x0); fit = XYZnew';
XYZold = fit; XYZold = XYZold'; x0=[0 0 1].'; u=[0 0 1].'; deg = 180 + azangle(i);
[XYZnew, R, t] = AxelRot(XYZold, deg, u, x0); fit = XYZnew';

% Resizing
X = fit(:,1).*sz+loc(1); Y = fit(:,2).*sz+loc(2); Z = fit(:,3).*sz+loc(3);

% Store data for individual mechanism types
if mean(ismember(eventdata{i,14},modlist{3})) == 1
    for ttt = 1:length(tind)
        tindex = tindex+1;
        tensile{tindex,1,tind(ttt)} = X;
        tensile{tindex,2,tind(ttt)} = Y;
        tensile{tindex,3,tind(ttt)} = Z;
    end
end

```

```

    tensile{tindex,4,tind(ttt)} = C3;
    tensile{tindex,5,tind(ttt)} = loc;
    tensile{tindex,6,tind(ttt)} = Cang(1);
    tensile{tindex,7,tind(ttt)} = abs(Cang(2));
end
elseif mean(ismember(eventdata{i,14},modlist{2})) == 1

    for ttt = 1:length(tind)
        sindex = sindex+1;
        shear{sindex,1,tind(ttt)} = X;
        shear{sindex,2,tind(ttt)} = Y;
        shear{sindex,3,tind(ttt)} = Z;
        shear{sindex,4,tind(ttt)} = C2;
        shear{sindex,5,tind(ttt)} = loc;
        shear{sindex,6,tind(ttt)} = Cang(1);
        shear{sindex,7,tind(ttt)} = abs(Cang(2));
    end
elseif mean(ismember(eventdata{i,14},modlist{1})) == 1
    for ttt = 1:length(tind)
        cindex = cindex+1;
        collapse{cindex,1,tind(ttt)} = X;
        collapse{cindex,2,tind(ttt)} = Y;
        collapse{cindex,3,tind(ttt)} = Z;
        collapse{cindex,4,tind(ttt)} = C1;
        collapse{cindex,5,tind(ttt)} = loc;
        collapse{cindex,6,tind(ttt)} = Cang(1);
        collapse{cindex,7,tind(ttt)} = abs(Cang(2));
    end
end

% Removes skipped data
ind = [ind,i];

% Converts event time to strain value
straintime(i,1) = mean(deform(abs(deform(:,1) - eventdata{i,2}) ==
min(abs(deform(:,1) - eventdata{i,2})),2));

end

eventdata = eventdata(ind,:);
straintime = straintime(ind);
etype = etype(ind);
rotangle = rotangle(ind);
azangle = azangle(ind);

```

7.2.4.6 SEPERATE EVENTS BY AZIMUTH ACCORDING TO PRINCIPAL SHEAR DIRECTION

```

% Compile
infstore = [straintime,abs(rotangle'),etype'];
infstore2 = [straintime,azangle',etype'];

% Remove bad data
ind = find(isnan(infstore(:,2)) == 1 | isnan(infstore2(:,2)) == 1);
infstore(ind,:) = [];

```

```

infstore2(ind,:) = [];

% Shear direction
viewang = mode(round(infstore2(infstore2(:,3) == 2,2),-1)); % - 30

% Seperation and correction
infstore2(:,2) = infstore2(:,2)-viewang;
for i = 1:size(infstore2,1)
    if infstore2(i,2) > 180
        infstore2(i,2) = -180 + abs(diff([infstore2(i,2) 180]));
    elseif infstore2(i,2) < -180
        infstore2(i,2) = 180 - abs(diff([infstore2(i,2) -180]));
    end
end
ind = find(infstore2(:,2) >= -90 & infstore2(:,2) <= 90);
infstore(:,4) = 2; % Perpendicular to shear
infstore(ind,4) = 1; % Parallel to shear

%return

```

7.2.4.7 DIVERGENCE MAPS

```

figure

% Plotting stuff
windows = FindClosestFactorization(min(min([size(shear,3) size(collapse,3)
size(tensile,3)])));
if windows(1) == 1 && windows(2) > 5
    windows = FindClosestFactorization(min(min([size(shear,3) size(collapse,3)
size(tensile,3)]))+1);
end

for k = 1:min(min([size(shear,3) size(collapse,3) size(tensile,3)]))

    % Set current plot
    if anim == 1
        cla; hold on;
        title([num2str(mean([badj(k) badj(k+1)])), '% Strain'])
    else
        subplot(windows(1),windows(2),k);cla; hold on;
    end
    pbaspect([4 10, 1])
    xlim([-0.02 0.02])
    ylim([-0.05 0.05])

    % Compile data for window
    cCo1 = cell2mat(collapse(:,6,k));
    cdip = cell2mat(collapse(:,7,k));
    csip = 90-abs(cdip);
    cCo1 = cCo1 -180;
    cCo1(cCo1 < 0) = 360 - abs(diff([cCo1(cCo1 < 0), zeros(length(cCo1(cCo1 <
0)),1)]));
    cloc = [cell2mat(tensile(:,5,k));
cell2mat(tensile(:,6,k));
cell2mat(tensile(:,7,k));
cell2mat(collapse(:,5,k));cell2mat(shear(:,5,k))];

```

```

cstrike = [cstrike;cCol;cell2mat(shear(:,6,k))];
cdip = [cdip;csip;cell2mat(shear(:,7,k))];

% Removes some more bad data
ind = find(isnan(cstrike)==1);
cloc(ind,:) = [];
cstrike(ind) = [];
cdip(ind) = [];

% Converts angular data into vectors
slocs = cloc;
posarray = []; magarray = []; magindex = 0;
for i = 1:size(cstrike,1)
    s1 = [cstrike(i),cdip(i)];
    lr = [-gstp/2 0 0;gstp/2 0 0];
    fit = lr;
    XYZold = fit; XYZold = XYZold'; x0=[0 0 1].'; u=[0 0 1].'; deg = 90+s1(1,1)-
mode(round(infstore2(infstore2(:,3)) == 2,2),-1));
    [XYZnew, R, t] = AxelRot(XYZold, deg, u, x0); fit = XYZnew';
    XYZold = fit; XYZold = XYZold'; x0=[0 0 0].'; u=[0 1 0].'; deg = s1(1,2);
    [XYZnew, R, t] = AxelRot(XYZold, deg, u, x0); fit = XYZnew';
    lr = fit+slocs(i,:);
    a = lr(lr(:,3)==max(lr(:,3)),:);
    b = slocs(i,:);
    c = lr(lr(:,3)==min(lr(:,3)),:);
    mpoint = (a+b)./2;
    magindex = magindex + 1;
    posarray(magindex,:) = [mpoint(1),mpoint(2),mpoint(3)];
    magarray(magindex,:) = [diff([a(1),c(1)]),diff([a(2),c(2)]),diff([a(3),c(3)])];
end

% Grid 3D vector data into 2D plane

gstp2 = gstp/5;
[X3,Y3,Z3] = meshgrid(-0.02:gstp2:0.02,-0.02:gstp2:0.02,-0.05:gstp2/(5/2):0.05);
xx = posarray(:,1);
yy = posarray(:,2);
zz = posarray(:,3);
vxx = magarray(:,1);
vyy = magarray(:,2);
vxx = zeros(length(magarray),1);
vzz = magarray(:,3);
FVx = griddata(xx,yy,zz,vxx,X3,Y3,Z3,'natural');
FVy = griddata(xx,yy,zz,vyy,X3,Y3,Z3,'natural');
FVz = griddata(xx,yy,zz,vzz,X3,Y3,Z3,'natural');
V3x = FVx;
V3y = FVy;
V3z = FVz;

% Calculate divergence map
div = divergence(V3x,V3y,V3z);

% Re grids the data a bit more
div = div(:);
Y3 = Y3(:); Z3 = Z3(:);
Y4 = Y3(isnan(div)==0);
Z4 = Z3(isnan(div)==0);
div2 = div(isnan(div)==0);

```

```

gstp3 = gstp/50;
[x,y] = meshgrid(-0.02:gstp3:0.02,-0.05:gstp3:0.05);
vq = griddata(Y4,Z4,div2,x(:),y(:),'cubic');

vq(vq>5e-4) = 5e-4;
vq(vq<-5e-4) = -5e-4;
lim = 5e-4;

% Plotting
contourf(-x,y,reshape(vq,size(x,1),size(x,2)),11,'LineStyle','none')
if anim == 1
    mapstore{k,1} = strainave(k);
    mapstore{k,2} = x;
    mapstore{k,3} = y;
    mapstore{k,4} = vq;
end
colormap(jet);

cmin = -lim;
cmax = lim;
caxis([cmin cmax])
colorbar('location','southoutside','Ticks',[cmin,cmax],...
'TickLabels',{'Compaction','Dilation'],'FontSize',30)

% Plot bounding box
plot([-0.02 -0.02 0.02 0.02 -0.02],[-0.05 0.05 0.05 -0.05 -0.05],'k-')

% 1cm scale bar
plot([-0.019 -0.019 -0.009 -0.009],[-0.0479 -0.049 -0.049 -0.0479],'k-','linewidth',3)
plot([-0.019 -0.019 -0.009 -0.009],[-0.048 -0.049 -0.049 -0.048],'w-','linewidth',1.5)

% Plot stuff
set(gca,'xtick',[])
set(gca,'xticklabel',[])
set(gca,'ytick',[])
set(gca,'yticklabel',[])
set(gca,'box','off')
set(gcf,'color','w')

drawnow
display(k)

if anim == 1 && saving == 1
    cd focalmechanimation
    set(gcf,'units','normalized','outerposition',[0 0 1 1])
    %myaa(10)
    saveas(gcf,[num2str(k),'.png'])
    cd ..
end
end

if anim == 0 && saving == 1
    set(gcf,'units','normalized','outerposition',[0 0 1 1])
    %myaa('publish')
    saveas(gcf,'divergencemaps.png')

```

```
end
```

```
%return
```

7.2.4.8 MECHANISM LOCATION PLOTS

```
% Sample cylinder
[X1 Y1 Z1] = cylinder(0.02); % Makes a cylinder with radius 0.02
Z1(2,:) = 0.1; % Sets cylinder height to 0.1
shp = surf2patch(X1,Y1,Z1); % Makes it into a patch
X = shp.vertices(:,1);
Y = shp.vertices(:,2);
Z = shp.vertices(:,3)-0.05; % Puts into the correct place
shp = alphaShape(X,Y,Z,1,'HoleThreshold',10000); % Makes it into a shape

% Plot Tensile events
figure;
for k = 1:min(min([size(shear,3) size(collapse,3) size(tensile,3)]))

    % Plot stuff
    subplot(1,min(min([size(shear,3) size(collapse,3) size(tensile,3)])),k);hold on;
    pbaspect([4 4, 10])
    xlim([-0.02 0.02])
    ylim([-0.02 0.02])
    zlim([-0.05 0.05])
    view([viewang 0])

    % Plot fracture ellipses
    for i = 1:size(tensile(:, :, k), 1)
        if i == 1; cla;
        plot(shp, 'FaceColor', 'black', 'EdgeColor', 'none', 'Facealpha', 0.1)
            set(gcf, 'color', 'w')
            axis off
            %camproj('perspective')
        end
        fill3(tensile{i,1,k},tensile{i,2,k},tensile{i,3,k},tensile{i,4,k}, 'linestyle', '-
', 'edgecolor', [0.25 0.25 0.25]);
        end
    %
    % % 1cm Scale bar
    % plot3([0 0 0 0],[ -0.019 -0.019 -0.009 -0.009],[ -0.0479 -0.049 -0.049 -0.0479], 'k-
', 'linewidth', 3)
    % plot3([0 0 0 0],[ -0.019 -0.019 -0.009 -0.009],[ -0.048 -0.049 -0.049 -0.048], 'w-
', 'linewidth', 1.5)

end

% Plot Shearing events
%figure;
for k = 1:min(min([size(shear,3) size(collapse,3) size(tensile,3)]))

    % Plot stuff
    subplot(1,min(min([size(shear,3) size(collapse,3) size(tensile,3)])),k);hold on;
    pbaspect([4 4, 10])
    xlim([-0.02 0.02])
    ylim([-0.02 0.02])
```



```

zlim([-0.05 0.05])
view([viewang 0])

% Plot fracture ellipses
for i = 1:size(shear(:, :, k), 1)
    %         if i == 1; %cla;
    %         plot(shp, 'FaceColor', 'black', 'EdgeColor', 'none', 'FaceAlpha', 0.1)
    %         set(gcf, 'color', 'w')
    %         axis off
    %         camproj('perspective')
    %         end
    fill3(shear{i, 1, k}, shear{i, 2, k}, shear{i, 3, k}, shear{i, 4, k}, 'linestyle', '-
', 'edgecolor', [0.25 0.25 0.25]);
end
end

% Plot Closing events
%figure(2);
for k = 1:min(min([size(shear, 3) size(collapse, 3) size(tensile, 3)]))

    % Plot stuff
    subplot(1, min(min([size(shear, 3) size(collapse, 3) size(tensile, 3)])), k); hold on;
    pbaspect([4 4, 10])
    xlim([-0.02 0.02])
    ylim([-0.02 0.02])
    zlim([-0.05 0.05])
    view([viewang 0])

    % Plot fracture ellipses
    for i = 1:size(collapse(:, :, k), 1)
        %         if i == 1; %cla;
        %         plot(shp, 'FaceColor', 'black', 'EdgeColor', 'none', 'FaceAlpha', 0.1)
        %         set(gcf, 'color', 'w')
        %         axis off
        %         camproj('perspective')
        %         end

        fill3(collapse{i, 1, k}, collapse{i, 2, k}, collapse{i, 3, k}, collapse{i, 4, k}, 'linestyle', '-
', 'edgecolor', [0.25 0.25 0.25]);
        end
    end

    if saving == 1
        set(gcf, 'units', 'normalized', 'outerposition', [0 0 1 1])
        %myaa('publish')
        saveas(gcf, 'mechmaps.png')
    end
end

```

7.3 PEAK DELAY

7.3.1 PEAK DELAY MEASUREMENT

Automatically picks the peak delay for the chosen frequency ranges

7.3.1.1 VERSION

Version 1.0, 12th February 2019. Thomas King - First Version

7.3.1.2 PARAMETER CUSTOMISATION

Below are the suggested parameters to be modified. I don't recommend changing any of the code outside of these parameters.

```
clear all; close all; warning off all

% sourceloc or eventdatamech (0 or 1)
sources = 0; % Loading data from eventdatamech allows to pick for specific types of
events e.g. T-type
mechtype = 'fitMM';

% Frequencys. Nx3 matrix, [min, max, mean]
freq(:,1) = [50000;100000;200000;400000];
freq(:,2) = 2.*freq(:,1);
freq(:,3) = round(freq(:,1) + (freq(:,2)-freq(:,1))/2,0);

% Pre-compile waveform data
compile = 1;
```

7.3.1.3 COMPILE DATA

```
if compile == 1
    % Load data
    load('recloc.mat');
    load('pktimes_m1.mat')
    load tempi_m1.mat
    load('sourceloc_m1.mat');
    if sources == 1
        load eventdatamech_m1.mat

        % Data clearing
        emptyCells = cellfun(@isempty,eventdata(:,14));
        eventdata(emptyCells,:) = [];

        % Match sourcelocs to eventdata file list
        ind = [];
        for i = 1:size(sourcelocs,1)
            for j = 1:size(eventdata,1)
                test = strcmp(sourcelocs{i,1},eventdata{j,1});
                if test == 1
```

```

        ind = [ind,i];
        break
    end

    end
end
sourcelocs = sourcelocs(ind,:);
pktimes = pktimes(:, :, ind);
tempi = tempi(ind);
end

% Compiles data into matrices
cd sg2; index = 0;
for i = 1:size(sourcelocs,1)
    display(num2str(size(sourcelocs,1)-i+1))

    % Skip mechanisms you don't want
    if sources == 1 && mean(ismember(eventdata{i,14},mechtype)) ~= 1
        continue
    end

    % Load waveform
    [signal,SR] = leggisg2(char(sourcelocs(i,1)));
    if index == 0; Ts = SR; Fs = 1/SR; end

    % Compile
    for j = 1:size(recloc,1)
        if isempty(pktimes{j,2,i}) == 1 || isnan(pktimes{j,2,i}) == 1
            continue
        end
        index = index + 1;
        allsig(:,index) = signal(:,j); % waveform data
        rayparam(index,1) = j; % channel
        rayparam(index,2) = pktimes{j,2,i}; % pick time pk(i,n);%
        rayparam(index,3) = norm(cell2mat(sourcelocs(i,2:4)) - recloc(j,:)); %
distance
        rayparam(index,4) = sourcelocs{i,5}; % Source time
        rayparam(index,5:7) = cell2mat(sourcelocs(i,2:4)); % Source Location
        rayparam(index,8:10) = recloc(j,:); % Receiver location
        rayparam(index,12) = i; %Event
        rayparam(index,13) = pktimes{j,3,i}; % SNR ratios
        rayparam(index,14) = pktimes{j,4,i};
        rayparam(index,15) = pktimes{j,5,i};
        rayparam(index,16) = pktimes{j,6,i};
        rayparam(index,17) = pktimes{j,7,i};

    end
end
cd ..
save peakdelayrays.mat allsig rayparam
else
    load peakdelayrays.mat
end

```

7.3.1.4 MEASURE PEAK DELAY

```

indextt = 0; % Clock
for fr = 1:size(freq,1) % Frequency
    for r = 1:size(allsig,2)
        % Set bandpass filter
        if r == 1
            [fsignal,Hd] = bandpass(allsig(:,r),[freq(fr,1) freq(fr,2)],Fs);
        else
            fsignal = filter(Hd,allsig(:,r));
        end

        % Clock
        indextt = indextt + 1;
        time = round((indextt/(size(freq,1)*size(allsig,2)))*100,1);
        if indextt == 1
            timemem = time;
        end
        if time > timemem
            display([num2str(time), '%'])
            timemem = time;
        end

        % Measurements
        tt = round(rayparam(r,2)/Ts,0); % arrival time
        sigbck = allsig(:,r); % backup
        efsignal = smooth(envelope(fsignal,round(freq(fr,3)/Fs)+1,'rms'),100); % smoothed
        envelope

        try
            delay = find(efsignal(tt:end) == max(efsignal(tt:end))); % peak delay
            lapseerr(r,fr) = abs(efsignal(delay+tt))./max(abs(efsignal(1:tt))); % error
        catch
            lapseerr(r,fr) = NaN;
        end
    end
end

save peakdelay_measurements.mat lapse lapseerr freq

```

7.3.2 PEAK DELAY PLOTTING

Plots peak delay in various forms

7.3.2.1 VERSION

Version 1.0, 12th February 2019. Thomas King - First Version

7.3.2.2 PARAMETER CUSTOMISATION

Below are the suggested parameters to be modified. I don't recommend changing any of the code outside of these parameters.

```
clear all; close all; warning off all

% Spatial maps parameters
modstp = 0.005; % Grid size used in mapping
numwin = 1; % Splits data into a number of time windows
numrays = 1000; % Maximum number of rays to use in maps, smaller = faster
deg = -70; % Rotate data for 2D maps
minrays = 2; % Minimum number of raypaths per grid block
smoothing = 1.1; % Smoothing parameter

% Corrections
timecorr = 132;
```

7.3.2.3 COMPILE

```
% Load data
load peakdelay_measurements.mat
load peakdelayrays.mat
load reoloc.mat

% Time calibration
stress_strain
rayparam(:,4) = rayparam(:,4) - start - timecorr;

nevents = round(size(rayparam,1)/numwin); % Fixed number of events

% Data sorting
[~,order] = sort(rayparam(:,4));
rayparam = rayparam(order,:);
lapse = lapse(order,:);
lapseerr = lapseerr(order,:);

% Data cleaning
tlim = [-8.91 -9.415 -9 -9.15]; % e.g. Mie resonance thresholds
for fr = 1:size(lapse,2)
    %ind = find(log(lapse(:,fr)) > tlim(fr)); % For example, anomalously high delays
    ind = find(lapseerr(:,fr) > 50 | lapseerr(:,fr) < 2 | ...
        log(lapse(:,fr)) > tlim(fr)); % Or too low Peak SNR
```

```

%ind = find(lapseerr(:,fr) > 2 & log(lapse(:,fr)) < tlim(fr) & lapseerr(:,fr)<200);
lapse(ind,fr) = NaN;
ind = 1:1:length(lapse(:,fr));

if fr == 1
    indmem = ind;
else
    ind2 = find(ismember(indmem,ind));
    indmem = indmem(ind2);
end
end
ind = indmem;
rayparam = rayparam(ind,:);
lapse = lapse(ind,:);
lapseerr = lapseerr(ind,:);

% Compile into single cell array
for fr = 1:size(lapse,2)
    clapse = lapse(:,fr);
    cerr = lapseerr(:,fr);
    crayparam = rayparam;
    lapsetimes{fr,1} = clapse;
    lapsetimes{fr,2} = crayparam;
    lapsetimes{fr,4} = cerr;
end

```

7.3.2.4 PEAK DELAY VS. TIME

```

% Time of sample failure
ind = find(diff(deform(:,2)) > 0.02);
failuretime = deform(ind(1),1);
factors = FindClosestFactorization(size(lapse,2));

for fr = 1:size(lapse,2)

    % Load
    cerr = lapsetimes{fr,4};
    crayparam = lapsetimes{fr,2};
    clapse = lapsetimes{fr,1};

    % Normalise around average
    clapse = clapse - mean(clapse(isnan(clapse)==0));

    % Calculate standard error in bins
    err = []; smtlapse = []; smoot = 1500;
    for e = 1:length(clapse)
        try
            chk = clapse(e-round(smoot/2):e+round(smoot/2));
            chk = chk(isnan(chk)==0);
            smtlapse(e) = mean(chk);
            err(e) = std(chk)/sqrt(length(chk));
        catch
            err(e) = NaN;
            smtlapse(e) = NaN;
        end
    end
end

```

```

% Plotting
figure(1); subplot(factors(1),factors(2),fr);
title([num2str(freq(fr,3)), 'KHz'])
yyaxis left; cla
shadedErrorBar(crayparam(:,4),smtlapse,err,'lineprops','k')
ylabel('Peak Delay')
xt = get(gca, 'YTick');
set(gca, 'FontSize', 16, 'Ycolor','k')
xt = get(gca, 'XTick');
set(gca, 'FontSize', 16)
set(gcf, 'color', 'white')
yyaxis right; cla;
hold on
plot(smooth(deform(:,1),100), (stress(:,2)), 'w-', 'linewidth', 4);
f = plot(smooth(deform(:,1),100), (stress(:,2)), 'k-', 'linewidth', 2);
ylabel('D. stress (MPa)', 'FontSize', 24, 'Color', 'k')
xlabel('Experimental time (minutes)', 'FontSize', 24)

xt = get(gca, 'YTick');
set(gca, 'FontSize', 16, 'Ycolor','k')
xt = get(gca, 'XTick');
set(gca, 'FontSize', 16)
set(gcf, 'color', 'white')
xlim([deform(1,1) deform(end,1)])

xticks([0:mean(diff(deform(:,1)))*round((max(deform(:,1)))/mean(diff(deform(:,1))))/5):max
(deform(:,1))])
datetick('x', 'MM:SS', 'keeplimits')
drawnow
end

```

7.3.2.5 AMPLITUDE RATIO COUNTS

```

for fr = 1:size(lapse,2)

% Load
cerr = lapsetimes{fr,4};
crayparam = lapsetimes{fr,2};

% Sets a threshold value
bmax = 25; % If plots come out blank, increase this value
[c,d] = find(cerr>bmax);
for j = 1:length(c)
    cerr(c(j),d(j)) = bmax;
end

% Before failure
figure(2); subplot(factors(1),factors(2),fr); cla
[a,b] = histcounts(cerr(crayparam(:,4) < failuretime), 'BinEdges', [0:bmax/10:bmax]);
[a2,b2] = histcounts(cerr(crayparam(:,4) > failuretime), 'BinEdges', [0:bmax/10:bmax]);
ind = find(a == max(a));
a = a(ind:end); b = b(ind+1:end)-0.25;
ind = find(a2 == max(a2));
a2 = a2(ind:end); b2 = b2(ind+1:end)-0.25;
histogram(cerr(crayparam(:,4) < failuretime), 'BinEdges', [0:bmax/10:bmax], ...

```

```

        'FaceColor',[0.65 0.65 0.65],'FaceAlpha',0.5)
hold on;
title([num2str(freq(fr,3)),' KHz before'],'FontSize',16)
try
    ylim([0 1.1*max(a(b<bmax))])
end
ylabel('Counts','FontSize',16); xlabel('Peak amplitude to noise ratio','FontSize',16)
set(gcf,'color','w')
xt = get(gca, 'YTick');
set(gca, 'FontSize', 16,'Ycolor','k')
xt = get(gca, 'XTick');
set(gca, 'FontSize', 16)

% After failure
figure(3); subplot(factors(1),factors(2),fr); cla
histogram(cerr(crayparam(:,4) > failuretime),'BinEdges',[0:bmax/10:bmax],...
    'FaceColor',[0 0 0],'FaceAlpha',0.5)
hold on
try
    ylim([0 1.1*max(a2(b2<bmax))])
end
ylabel('Counts','FontSize',16); xlabel('Peak amplitude to noise ratio','FontSize',16)
title([num2str(freq(fr,3)),' KHz after'],'FontSize',16)
set(gcf,'color','w')
xt = get(gca, 'YTick');
set(gca, 'FontSize', 16,'Ycolor','k')
xt = get(gca, 'XTick');
set(gca, 'FontSize', 16)
drawnow

end

```

7.3.2.6 PEAK DELAY VS. FREQUENCY

```

mpeak = []; stack = [];
for fr = 1:size(lapse,2)

    % Load
    crayparam = lapsetimes{fr,2};
    clapse = lapsetimes{fr,1};

    % Stack data and take average
    mpeak(fr,:) = [freq(fr,3),mean(clapse(isnan(clapse)==0))];
    stack = vertcat(stack, [repmat(freq(fr,3),length(clapse),1),clapse, crayparam(:,4)]);

end

% Data fitting
p1 = polyfit(stack(stack(:,3)<failuretime,1),(stack(stack(:,3)<failuretime,2)),1);
p2 = polyfit(stack(stack(:,3)>failuretime,1),(stack(stack(:,3)>failuretime,2)),1);

% Plotting
figure(4); cla; title('Frequency')
scatter(stack(:,1),(stack(:,2)),5,[0.5 0.5 0.5],'filled'); hold on
plot(freq(:,3),freq(:,3)*p1(1)+p1(2),'r-'); % before
plot(freq(:,3),freq(:,3)*p2(1)+p2(2),'b-'); % after

```



```

ylabel('Peak Delay','FontSize',16)
xlabel('Frequency (Hz)','FontSize',16)
set(gcf,'color','w')
xt = get(gca, 'YTick');
set(gca, 'FontSize', 16,'Ycolor','k')
xt = get(gca, 'XTick');
set(gca, 'FontSize', 16)
drawnow

```

7.3.2.7 PEAK DELAY VS. HYPOCENTRAL DISTANCE

```

b2 = [];
for fr = 1:size(lapse,2)

    % Load
    crayparam = lapsetimes{fr,2};
    clapse = lapsetimes{fr,1};

    % Data fitting
    y = (clapse);
    x = (crayparam(:,3));
    [~,order] = sort(x);
    x = x(order);
    y = y(order);
    ind = find(isnan(y) == 0 & isinf(y) == 0 & ...
        crayparam(:,3) > 0.02 & crayparam(:,3) < 0.04;% > 0 & err < 100);
    w = ones(length(x),1);
    w(log(y(ind)) > -11 & log(y(ind)) < -9) = 10;

    b2(:,fr) = flipud(wpolyfit(log(x(ind)),log(y(ind)),1,w(ind))');

    % Plotting
    figure(5); subplot(factors(1),factors(2),fr); cla; hold on
    scatter((x).*1000,log(y),5,[0.5 0.5 0.5],'filled')
    plot([min(x):0.001:max(x)].*1000,log([min(x):0.001:max(x)])*b2(2,fr) + b2(1,fr),'k-
', 'Linewidth',2)
    title([num2str(freq(fr,3)), 'KHz'],'FontSize',16)
    ylabel('log(t_p) (ms)','FontSize',16)
    xlabel('R (mm)','FontSize',16)
    set(gcf,'color','w')
    xt = get(gca, 'YTick');
    set(gca, 'FontSize', 16,'Ycolor','k')
    xt = get(gca, 'XTick');
    set(gca, 'FontSize', 16)

    % Hypocentral distance correction
    cpobs = real(log(y) - log(x)*b2(2,fr) + b2(1,fr));
    cpobs(isinf(cpobs)==1) = NaN;
    dtpobs{fr,1} = cpobs;
    drawnow

end

```

7.3.2.8 SPATIAL MAPPING

```

[x,y,z] = meshgrid(-0.04:modstp:0.04,-0.04:modstp:0.04,-0.1:modstp/(5/2):0.1);
model = x(:);
model(:,2) = y(:);
model(:,3) = z(:);
model(:,4) = [1:1:size(model,1)];
modelbck = model; % backup

for n = 1:numwin
    for fr = 1:size(freq,1)
        % Load
        crayparam = lapsetimes{fr,2};

        % Ray tracing
        if fr == 1
            raypath = [];
            if n ~= numwin
                sources = [crayparam(nevents*(n-1)+1:nevents*n,5:7) crayparam(nevents*(n-1)+1:nevents*n,...
                    8:10) [1:1:length(crayparam(nevents*(n-1)+1:nevents*n,5))]']
                crayparam(nevents*(n-1)+1:nevents*n,4)];
            else
                sources = [crayparam(nevents*(n-1)+1:end,5:7) crayparam(nevents*(n-1)+1:end,...
                    8:10) [1:1:length(crayparam(nevents*(n-1)+1:end,5))]']
                crayparam(nevents*(n-1)+1:end,4)];
            end
            % Draw rays
            figure(6); cla; hold on
            for i = 1:round(size(sources,1)/numrays)+1:size(sources,1)

                % Source position
                x3 = sources(i,1);
                y3 = sources(i,2);
                z3 = sources(i,3);

                % Receiver position
                x4 = sources(i,4);
                y4 = sources(i,5);
                z4 = sources(i,6);

                % Event time
                t = sources(i,end);

                % Compiles rays
                raystep = 0:modstp/4:norm([x3 y3 z3] - [x4 y4 z4]);
                try; raypath2 = linspaceNDim([x3 y3 z3],[x4 y4 z4], length(raystep));
                catch; continue; end
                raypath2 = raypath2';
                raypath2(:,4) = sources(i,7);
                raypath2(:,6) = i;
                raypath2(:,10) = t;
                [~,ang] = rangeangle([x3 y3 z3]',[x4 y4 z4]');
                raypath2(:,7) = ang(1);
                % Plot rays
                plot3(raypath2(:,1),raypath2(:,2),raypath2(:,3),'color',[0.5 0.5 0.5])

```

```

raypath = vertcat(raypath,raypath2);

end

% Plot source locations
scatter3(sources(:,1),sources(:,2),sources(:,3),'ko','filled')

% Rotate data
XYZold = raypath(:,1:3); XYZold = XYZold'; x0=[0 0 0].'; u=[0 0 1].';
[XYZnew, R, t] = AxelRot(XYZold, deg, u, x0); raypath(:,1:3) = XYZnew';
XYZold = sources(:,1:3); XYZold = XYZold'; x0=[0 0 0].'; u=[0 0 1].';
[XYZnew, R, t] = AxelRot(XYZold, deg, u, x0); sources2 = XYZnew';

% Ray tracing
for i = 1:size(raypath,1)
    [ind, d] = dsearchn(model(:,1:3),raypath(i,1:3));
    ind = ind(d<modstp);
    try; raypath(i,5) = model(ind,4);
    catch; raypath(i,5) = model(ind(1),4);end
end
[C, IA, IC] = unique(raypath(:,4:6),'rows','stable');
raypath = raypath(IA,:);
raypathbck = raypath;
end

% Reset
raypath = raypathbck;
model = modelbck;

% Set data to current frequency band
dtlapse = dtpobs{fr,1};
raypath(:,4) = dtlapse(raypath(:,4));

% Find average value for each grid step
for i = 1:size(model,1)
    ind = find(raypath(:,5) == i);
    ind2 = find(isnan(raypath(ind,5)) == 0);
    ind = ind(ind2);
    if length(ind) > minrays
        val = raypath(ind,4);
        val = val(isoutlier(val,'quartiles')==0);
        try
            model(i,5) = mean(val);
        catch
            model(i,5) = NaN;
        end
        % model(i,7) = std(val)/sqrt(length(ind)); % standard deviation of block
        model(i,7) = range(val); % or the range
        % model(i,5) = model(i,7); % Debugging
        model(i,8) = length(ind); % number of measurements
    else
        model(i,5) = NaN;
        model(i,7) = NaN;
        model(i,8) = NaN;
    end
end
end

% Plot smoothing
for i = 1:size(model,1)

```

```

        if isnan(model(i,5)) == 1
            model(i,6) = NaN;
            continue
        end
        [Idx,D] = knnsearch(model(i,2:3),model(:,2:3));
        ind = find(D < modstp*smoothing);
        val = model(ind,5);
        val = val(find(isnan(val) == 0));
        model(i,6) = mean(val);
    end

    % Normalise to average
    ind = find(isnan(model(:,6)) == 1);
    mtp = mean(model(isnan(model(:,6)) == 0,6));
    model(ind,:) = [];
    model(:,6) = model(:,6) - mtp;

    % Regrid data onto a finer mesh
    [x,y] = meshgrid(-0.02:0.0001:0.02,-0.05:0.0001:0.05);
    vq = griddata(model(:,2),model(:,3),model(:,6),x(:),y(:));

    % Plotting
    figure(6+n);
    subplot(1,size(freq,1),fr); cla;
    contourf(x,y,reshape(vq,size(x,1),size(x,2)),11,'LineStyle','none')
    newmap = brighten(jet(11),-.2); colormap(newmap);
    hold on
    scatter(sources2(:,2),sources2(:,3),'k.')
    title(['[',num2str(freq(fr,1)/1000),'-',num2str(freq(fr,2)/1000),'
KHz]'],'FontSize',16,'color','k')
    set(gcf,'color','white')
    set(gca,'visible','on')
    ylim([-0.05 0.05])
    xlim([-0.02 0.02])
    pbaspect([4 10 1])
    xt = get(gca, 'YTick');
    set(gca, 'FontSize', 16, 'Ycolor', 'k')
    xt = get(gca, 'XTick');
    set(gca, 'FontSize', 16)
    h = colorbar('southoutside','FontSize',16,'color','k');
    caxis([-0.1 0.1]) % colour limits
    xlabel(h,'\Delta log(t_p)','FontSize',16,'color','k')
    plot([-0.02 -0.02 0.02 0.02 -0.02],[-0.05 0.05 0.05 -0.05 -0.05],'k-')
    set(gca,'xtick',[])
    set(gca,'xticklabel',[])
    set(gca,'ytick',[])
    set(gca,'yticklabel',[])
    set(gca,'box','off')

    % Scale
    plot([-0.019 -0.019 -0.009 -0.009],[-0.048 -0.049 -0.049 -0.048],'k-
','linewidth',1.5)
    text(-0.014,-
0.0485,'1cm','HorizontalAlignment','center','VerticalAlignment','bottom','FontSize',16)
    drawnow
end
end

```

8 REFERENCES

- Abubakirov, I.R., Gusev, A.A., 1990. Estimation of scattering properties of lithosphere of Kamchatka based on Monte-Carlo simulation of record envelope of a near earthquake. *Phys. Earth Planet. Inter.* 64, 52–67. [https://doi.org/10.1016/0031-9201\(90\)90005-i](https://doi.org/10.1016/0031-9201(90)90005-i)
- Amitrano, D., Helmstetter, A., 2006. Brittle creep, damage, and time to failure in rocks. *J. Geophys. Res. Solid Earth* 111.
- Anderson, M., BAIRD, H.C., 1924. *Metallurgy of Aluminium*. N. Y.
- Baird, A.F., Kendall, J.-M., Angus, D.A., 2013. Frequency-dependent seismic anisotropy due to fractures: Fluid flow versus scattering. *GEOPHYSICS* 78, WA111–WA122. <https://doi.org/10.1190/geo2012-0288.1>
- Bandt, C., Pompe, B., 2002. Permutation entropy: a natural complexity measure for time series. *Phys. Rev. Lett.* 88, 174102.
- Baud, P., Meredith, P., 1997. Damage accumulation during triaxial creep of Darley Dale sandstone from pore volumetry and acoustic emission. *Int. J. Rock Mech. Min. Sci.* 34, 24-e1.
- Baud, P., Wong, T., Zhu, W., 2014. Effects of porosity and crack density on the compressive strength of rocks. *Int. J. Rock Mech. Min. Sci.* 67, 202–211.
- Bažant, Z.P., Pfeiffer, P.A., 1986. Shear fracture tests of concrete. *Mater. Struct.* 19, 111. <https://doi.org/10.1007/BF02481755>
- Beeler, N.M., Simpson, R.W., Hickman, S.H., Lockner, D.A., 2000. Pore fluid pressure, apparent friction, and Coulomb failure. *J. Geophys. Res. Solid Earth* 105, 25533–25542.
- Belyadi, H., Fathi, E., Belyadi, F., 2017. Chapter Nine - Fracture Pressure Analysis and Perforation Design, in: Belyadi, H., Fathi, E., Belyadi, F. (Eds.), *Hydraulic Fracturing in Unconventional Reservoirs*. Gulf Professional Publishing, Boston, pp. 121–141. <https://doi.org/10.1016/B978-0-12-849871-2.00009-5>
- Ben-Menahem, A., Gibson, R.L., 1995. Radiation of elastic waves from sources embedded in anisotropic inclusions. *Geophys. J. Int.* 122, 249–265. <https://doi.org/10.1111/j.1365-246X.1995.tb03552.x>
- Benson, P.M., Thompson, B.D., Meredith, P.G., Vinciguerra, S., Young, R.P., 2007. Imaging slow failure in triaxially deformed Etna basalt using 3D acoustic-emission location and X-ray computed tomography. *Geophys. Res. Lett.* 34. <https://doi.org/10.1029/2006gl028721>
- Benson, P.M., Vinciguerra, S., Meredith, P.G., Young, R.P., 2010. Spatio-temporal evolution of volcano seismicity: A laboratory study. *Earth Planet. Sci. Lett.* 297, 315–323.
- Berryman, J.G., Wang, H.F., 1995. The elastic coefficients of double-porosity models for fluid transport in jointed rock. *J. Geophys. Res. Solid Earth* 100, 24611–24627. <https://doi.org/10.1029/95jb02161>
- Bieniawski, Z.T., 1968. Propagation of brittle fracture in rock, in: *The 10th US Symposium on Rock Mechanics (USRMS)*. American Rock Mechanics Association.

- Bieniawski, Z.T., 1967. Stability concept of brittle fracture propagation in rock. *Eng. Geol.* 2, 149–162.
- Birch, F., 1961. The velocity of compressional waves in rocks to 10 kilobars: 2. *J. Geophys. Res.* 66, 2199–2224.
- Birch, F., 1960. The velocity of compressional waves in rocks to 10 kilobars: 1. *J. Geophys. Res.* 65, 1083–1102.
- Birch, F., Bancroft, D., 1938. Elasticity and internal friction in a long column of granite. *Bull. Seismol. Soc. Am.* 28, 243–254.
- Biwa, S., Hiraiwa, S., Matsumoto, E., 2007. Stiffness evaluation of contacting surfaces by bulk and interface waves. *Ultrasonics* 47, 123–129. <https://doi.org/10.1016/j.ultras.2007.08.005>
- Bohse, J., 2000. Acoustic emission characteristics of micro-failure processes in polymer blends and composites. *Compos. Sci. Technol.* 60, 1213–1226. [https://doi.org/10.1016/S0266-3538\(00\)00060-9](https://doi.org/10.1016/S0266-3538(00)00060-9)
- Bonner, B.P., 1974. Shear wave birefringence in dilating granite. *Geophys. Res. Lett.* 1, 217–220. <https://doi.org/10.1029/gl001i005p00217>
- Borleanu, F., De Siena, L., Thomas, C., Popa, M., Radulian, M., 2017. Seismic scattering and absorption mapping from intermediate-depth earthquakes reveals complex tectonic interactions acting in the Vrancea region and surroundings (Romania). *Tectonophysics* 706–707, 129–142. <https://doi.org/10.1016/j.tecto.2017.04.013>
- Brace, W.F., 1960. An extension of the Griffith theory of fracture to rocks. *J. Geophys. Res.* 65, 3477–3480.
- Brace, W.F., Bombolakis, E.G., 1963. A note on brittle crack growth in compression. *J. Geophys. Res.* 68, 3709–3713.
- Bubeck, A., Walker, R.J., Healy, D., Dobbs, M., Holwell, D.A., 2017. Pore geometry as a control on rock strength. *Earth Planet. Sci. Lett.* 457, 38–48.
- Bugini, R., Pavese, A., Borroni, S., Folli, L., 2000. White granites used in Lombard architecture, in: *Proceedings of the 9th International Congress on Deterioration and Conservation of Stone*. Elsevier, pp. 41–48.
- Byerlee, J.D., 1967. Frictional characteristics of granite under high confining pressure. *J. Geophys. Res.* 72, 3639–3648.
- Calvet, M., Sylvander, M., Margerin, L., Villaseñor, A., 2013. Spatial variations of seismic attenuation and heterogeneity in the Pyrenees: Coda Q and peak delay time analysis. *Tectonophysics* 608, 428–439. <https://doi.org/10.1016/j.tecto.2013.08.045>
- Cavallo, A., Bigioggero, B., Colombo, A., Tunesi, A., 2004. The Verbano Cusio Ossola province: a land of quarries in northern Italy (Piedmont). *Miner.* 73, 197.
- Cen, D., Huang, D., Song, Y., Jiang, Q., 2020. Direct Tensile Behavior of Limestone and Sandstone with Bedding Planes at Different Strain Rates. *Rock Mech. Rock Eng.* 1–9.
- Chen, H.K., Zhou, Y.T., Wang, Z., 2014. Study on Damage Characteristics of Unstable Rocks under Excitation Effect, in: *Applied Mechanics and Materials*. Trans Tech Publ, pp. 575–581.

- Colmenares, L.B., Zoback, M.D., 2002. A statistical evaluation of intact rock failure criteria constrained by polyaxial test data for five different rocks. *Int. J. Rock Mech. Min. Sci.* 39, 695–729.
- Colombi, A., Roux, P., Guenneau, S., Gueguen, P., Craster, R.V., 2016. Forests as a natural seismic metamaterial: Rayleigh wave bandgaps induced by local resonances. *Sci. Rep.* 6. <https://doi.org/10.1038/srep19238>
- Comanducci, L., Cobos, M., Antonacci, F., Sarti, A., 2020. Time Difference of Arrival Estimation from Frequency-Sliding Generalized Cross-Correlations Using Convolutional Neural Networks. *ArXiv200200641 Cs Eess*.
- Cox, S.J.D., Scholz, C.H., 1988. Rupture initiation in shear fracture of rocks: an experimental study. *J. Geophys. Res. Solid Earth* 93, 3307–3320.
- Crisci, E., 2019. Hydro-mechanical response of Opalinus Clay shale: dependency on composition and burial depth. EPFL.
- Czochralski, J., 1916. Die Metallographie des Zinns und die Theorie der Formänderung bildsamer Metalle. *Met. Erz* 13, 381–393.
- De Siena, L., Calvet, M., Watson, K.J., Jonkers, A.R.T., Thomas, C., 2016. Seismic scattering and absorption mapping of debris flows, feeding paths, and tectonic units at Mount St. Helens volcano. *Earth Planet. Sci. Lett.* 442, 21–31. <https://doi.org/10.1016/j.epsl.2016.02.026>
- Ding, G., Sun, L., Wan, Z., Li, J., Pei, X., Tang, Y., 2018. Recognition of Damage Modes and Hilbert–Huang Transform Analyses of 3D Braided Composites. *J. Compos. Sci.* 2, 65.
- Ekanem, A.M., Li, X.Y., Chapman, M., Ian, M., Wei, J., 2014. Effect of Fracture Aperture on P-Wave Attenuation: A Seismic Physical Modelling Study. *ISRN Geophys.* 2014, 1–8. <https://doi.org/10.1155/2014/241279>
- Fang, X., Fehler, M., Chen, T., Burns, D., Zhu, Z., 2013. Sensitivity analysis of fracture scattering. *GEOPHYSICS* 78, T1–T10. <https://doi.org/10.1190/geo2011-0521.1>
- Faulkner, D.R., 2006. PATERSON, M. S. & WONG T.-F. 2005. *Experimental Rock Deformation – The Brittle Field*, 2nd ed. x plus 348 pp. Berlin, Heidelberg, New York: Springer-Verlag. Price Euros 89.95 (plus VAT at local rate), SFr 152.50, £69, US dollar 119 (hard covers). ISBN 3 540 24023 3. *Geol. Mag.* 143, 934–935. <https://doi.org/10.1017/s0016756806242973>
- Fazio, M., 2017. *Dynamic Laboratory Simulations of Fluid-Rock Coupling with Application to Volcano Seismicity and Unrest* (PhD Thesis). University of Portsmouth, School of Earth and Environmental Sciences.
- Fazio, M., Alparone, S., Benson, P.M., Cannata, A., Vinciguerra, S., 2019. Genesis and mechanisms controlling tornillo seismo-volcanic events in volcanic areas. *Sci. Rep.* 9, 1–11.
- Förster, F., Scheil, E., 1936. Acoustical study of formation of martensite needles. *Naturwissenschaften* 28, 245–247.
- FOWIER, T., 1986. Experience with acoustic emission monitoring of chemical process industry vessels. *Prog. Acoust. Emiss.* III 150–162.
- Frohlich, C., DeShon, H., Stump, B., Hayward, C., Hornbach, M., Walter, J.I., 2016. A historical review of induced earthquakes in Texas. *Seismol. Res. Lett.* 87, 1022–1038.

- Gehne, S., 2018. A laboratory study of fluid-driven tensile fracturing in anisotropic rocks. University of Portsmouth.
- Graham, C.C., Stanchits, S., Main, I.G., Dresen, G., 2010. Comparison of polarity and moment tensor inversion methods for source analysis of acoustic emission data. *Int. J. Rock Mech. Min. Sci.* 47, 161–169. <https://doi.org/10.1016/j.ijrmms.2009.05.002>
- Green, M., Watson, A.L., 1989. Evaluating buildings in seismic zones. *Assoc. Preserv. Technol. Bull.* 20, 13–17.
- Griffith, A.A., 1920. The phenomena of rupture and flow in solids: *Philosophical Transaction of Royal Society of London*, v. 221.
- GRIGGS, D., HANDIN, J., 1960. Chapter 13: Observations on Fracture and a Hypothesis of Earthquakes. *Geol. Soc. Am. Mem.* 347–364. <https://doi.org/10.1130/mem79-p347>
- Griggs, D.T., 1936. Deformation of Rocks under High Confining Pressures: I. Experiments at Room Temperature. *J. Geol.* 44, 541–577. <https://doi.org/10.1086/624455>
- Grosse, C.U., Ohtsu, M., 2008. Acoustic emission testing. Springer Science & Business Media.
- Guoping, Z., Yanchun, W., Rongliang, S., 2004. An improved method for first arrival pickup using energy ratio. *Geophys. Prospect. Pet.* 43, 345–347.
- Hackston, A., Rutter, E., 2016. The Mohr–Coulomb criterion for intact rock strength and friction—a re-evaluation and consideration of failure under polyaxial stresses. *Solid Earth* 7, 493–508.
- Hadley, K., 1976. Comparison of calculated and observed crack densities and seismic velocities in westerly granite. *J. Geophys. Res.* 81, 3484–3494. <https://doi.org/10.1029/jb081i020p03484>
- Haffner, P., Waibel, A., 1992. Multi-state time delay networks for continuous speech recognition, in: *Advances in Neural Information Processing Systems*. pp. 135–142.
- Haimson, B., Chang, C., 2000. A new true triaxial cell for testing mechanical properties of rock, and its use to determine rock strength and deformability of Westerly granite. *Int. J. Rock Mech. Min. Sci.* 37, 285–296.
- Hallbauer, D.K., Wagner, H., Cook, N.G.W., 1973. Some observations concerning the microscopic and mechanical behaviour of quartzite specimens in stiff, triaxial compression tests, in: *International Journal of Rock Mechanics and Mining Sciences & Geomechanics Abstracts*. Elsevier, pp. 713–726.
- Hamdi, S.E., Le Duff, A., Simon, L., Plantier, G., Sourice, A., Feuilloy, M., 2013. Acoustic emission pattern recognition approach based on Hilbert–Huang transform for structural health monitoring in polymer-composite materials. *Appl. Acoust.* 74, 746–757.
- Hanks, T.C., 1992. Small earthquakes, tectonic forces. *Science* 256, 1430–1432.
- Harnett, C.E., Benson, P.M., Rowley, P., Fazio, M., 2018. Fracture and damage localization in volcanic edifice rocks from El Hierro, Stromboli and Tenerife. *Sci. Rep.* 8. <https://doi.org/10.1038/s41598-018-20442-w>
- He, W., Chen, K., Hayatdavoudi, A., Sawant, K., Lomas, M., 2019. Effects of clay content, cement and mineral composition characteristics on sandstone rock strength and deformability behaviors. *J. Pet. Sci. Eng.* 176, 962–969.

- Heap, M.J., Baud, P., Meredith, P.G., Bell, A.F., Main, I.G., 2009. Time-dependent brittle creep in Darley Dale sandstone. *J. Geophys. Res. Solid Earth* 114.
- Hoek, E., Bieniawski, Z.T., 1965. Brittle fracture propagation in rock under compression. *Int. J. Fract. Mech.* 1, 137–155.
- Høgsberg, J., Krenk, S., 2015. Balanced calibration of resonant piezoelectric RL shunts with quasi-static background flexibility correction. *J. Sound Vib.* 341, 16–30. <https://doi.org/10.1016/j.jsv.2014.12.006>
- Huang, N.E., Shen, Z., Long, S.R., Wu, M.C., Shih, H.H., Zheng, Q., Yen, N.-C., Tung, C.C., Liu, H.H., 1998. The empirical mode decomposition and the Hilbert spectrum for nonlinear and non-stationary time series analysis. *Proc. R. Soc. Lond. Ser. Math. Phys. Eng. Sci.* 454, 903–995.
- Imperator, W., Mai, P.M., 2015. The role of topography and lateral velocity heterogeneities on near-source scattering and ground-motion variability. *Geophys. J. Int.* 202, 2163–2181.
- Jaeger, J.C., Cook, N.G.W., Zimmerman, R.W., 2007. *Fundamentals of rock mechanics*, 4th edn Blackwell. Maiden MA.
- JCMS-IIIB5706, 2003. Monitoring method for active cracks in concrete by acoustic emission. Federation of Construction Materials Industries Japan.
- Jia, B., Sun, A., Pan, Y., Chen, H., Liu, F., 2019. Accurate Method for Picking Up the First Arrival Time of Microseismic Signals Based on Entropy Theory [WWW Document]. *Adv. Civ. Eng.* <https://doi.org/10.1155/2019/6074781>
- Jian, D., Xibing, L., Desheng, G., 2004. Probability Distribution of Rock Mechanics Parameters by Using Maximum Entropy Method [J]. *Chin. J. Rock Mech. Eng.* 13.
- Kaiser, J., 1950. Results and conclusions from measurements of sound in metallic materials under tensile stress. *Tech. Hochschule*.
- Kanamori, H., Cipar, J.J., 1974. Focal process of the great Chilean earthquake May 22, 1960. *Phys. Earth Planet. Inter.* 9, 128–136.
- Katcoff, C.Z., Graham-Brady, L.L., 2014. Modeling dynamic brittle behavior of materials with circular flaws or pores. *Int. J. Solids Struct.* 51, 754–766.
- King, T., Benson, P., De Siena, L., Vinciguerra, S., 2017. Investigating the Apparent Seismic Diffusivity of Near-Receiver Geology at Mount St. Helens Volcano, USA. *Geosciences* 7, 130. <https://doi.org/10.3390/geosciences7040130>
- Kovári, K., Tisa, A., 1975. Multiple Failure State and Strain Controlled Triaxial tests. *Rock Mech.* 7, 17–33. <https://doi.org/10.1007/BF01239232>
- Lei, X., Kusunose, K., Rao, M.V.M.S., Nishizawa, O., Satoh, T., 2000. Quasi-static fault growth and cracking in homogeneous brittle rock under triaxial compression using acoustic emission monitoring. *J. Geophys. Res. Solid Earth* 105, 6127–6139. <https://doi.org/10.1029/1999JB900385>
- Lei, X., Nishizawa, O., Kusunose, K., Satoh, T., 1992. Fractal structure of the hypocenter distributions and focal mechanism solutions of acoustic emission in two granites of different grain sizes. *J. Phys. Earth* 40, 617–634.
- L'Hermite, R., 1960. Volume change of concrete. In: *Proc 4th int symp on chemistry of cement*, V-3. NBS monograph 43, NBS, Washington, DC, p. 659–94.

- Li, H.B., Zhao, J., Li, T.J., 1999. Triaxial compression tests on a granite at different strain rates and confining pressures. *Int. J. Rock Mech. Min. Sci.* 36, 1057–1063.
- Liu, A., Lin, W., Jiang, J., 2020. Investigation of the Long-Term Strength Properties of a Discontinuity by Shear Relaxation Tests. *Rock Mech. Rock Eng.* 53, 831–840.
- Lockner, D.A., Byerlee, J.D., Kuksenko, V., Ponomarev, A., Sidorin, A., 1992. Observations of quasistatic fault growth from acoustic emissions, in: *International Geophysics*. Elsevier, pp. 3–31.
- Lockner, D.A., Byerlee, J.D., Kuksenko, V., Ponomarev, A., Sidorin, A., 1991. Quasi-static fault growth and shear fracture energy in granite. *Nature* 350, 39–42. <https://doi.org/10.1038/350039a0>
- Lockner, D.A., Walsh, J.B., Byerlee, J.D., 1977. Changes in seismic velocity and attenuation during deformation of granite. *J. Geophys. Res.* 82, 5374–5378. <https://doi.org/10.1029/jb082i033p05374>
- Luo, X., Haya, H., Inaba, T., Shiotani, T., Nakanishi, Y., 2004. Damage evaluation of railway structures by using train-induced AE. *Constr. Build. Mater.*, 3rd Kumamoto International Workshop on Fracture, Acoustic Emission and NDE in Concrete (KIFA-3) 18, 215–223. <https://doi.org/10.1016/j.conbuildmat.2003.10.011>
- Luo, X., Haya, H., Inaba, T., Shiotani, T., Nakanishi, Y., 2002. Experimental study on evaluation of breakage in foundations using train-induced acoustic emission, in: *Proc. Structural Engineering World Congress*. pp. T9-1.
- Lyakhovskiy, V., Zhu, W., Shalev, E., 2015. Visco-poroelastic damage model for brittle-ductile failure of porous rocks. *J. Geophys. Res. Solid Earth* 120, 2179–2199.
- McBeck, J., Kandula, N., Aiken, J.M., Cordonnier, B., Renard, F., 2019. Isolating the factors that govern fracture development in rocks throughout dynamic in situ X-ray tomography experiments. *Geophys. Res. Lett.*
- McClintock, F.A., 1962. Friction on Griffith cracks in rocks under pressure, in: *Proc. 4th US Nat. Congr. Appl. Mech.* pp. 1015–1022.
- Mehranpour, M.H., Kulatilake, P.H., 2016. Comparison of six major intact rock failure criteria using a particle flow approach under true-triaxial stress condition. *Geomech. Geophys. Geo-Energy Geo-Resour.* 2, 203–229.
- Menéndez, B., Zhu, W., Wong, T.-F., 1996. Micromechanics of brittle faulting and cataclastic flow in Berea sandstone. *J. Struct. Geol.* 18, 1–16.
- Mikumo, T., Ando, M., 1976. A SEARCH INTO THE FAULTING MECHANISM OF THE 1891 GREAT NORI EARTHQUAKE. *J. Phys. Earth* 24, 63–87.
- Mogi, K., 1962. Magnitude-frequency relation for elastic shocks accompanying fractures of various materials and some related problems in earthquakes. *Bull Earthq Res Inst* 40, 831–853.
- Mohr, O., 1900. Welche Umstände bedingen die Elastizitätsgrenze und den Bruch eines Materials. *Z. Ver. Dtsch. Ingenieure* 46, 1572–1577.
- Murrell, S.A.F., 1964. The theory of the propagation of elliptical Griffith cracks under various conditions of plane strain or plane stress: Part I. *Br. J. Appl. Phys.* 15, 1195.
- Murrell, S.A.F., Digby, P.J., 1972. The thermodynamics of brittle fracture initiation under triaxial stress conditions. *Int. J. Fract. Mech.* 8, 167–173.

- Murrell, S.A.F., Ismail, I.A.H., 1976. The effect of decomposition of hydrous minerals on the mechanical properties of rocks at high pressures and temperatures. *Tectonophysics* 31, 207–258. [https://doi.org/10.1016/0040-1951\(76\)90120-7](https://doi.org/10.1016/0040-1951(76)90120-7)
- Napolitano, F., De Siena, L., Gervasi, A., Guerra, I., Scarpa, R., La Rocca, M., 2019. Scattering and absorption imaging of a highly fractured fluid-filled seismogenetic volume in a region of slow deformation. *Geosci. Front.* <https://doi.org/10.1016/j.gsf.2019.09.014>
- Negi, P., Chakraborty, T., 2019. Acquisition of Acoustic Emission Signals from Rocks Using Directly Bonded PZT Patches. *Indian Geotech. J.* <https://doi.org/10.1007/s40098-019-00398-y>
- Nur, A., 1971. Effects of stress on velocity anisotropy in rocks with cracks. *J. Geophys. Res.* 76, 2022–2034. <https://doi.org/10.1029/jb076i008p02022>
- Ohtsu, M., Uchida, M., Okamoto, T., Yuyama, S., 2002. Damage Assessment of Reinforced Concrete Beams Qualified by Acoustic Emission. *Struct. J.* 99, 411–417. <https://doi.org/10.14359/12109>
- Oldham, R.D., 1899. Report of the great earthquake of 12th June, 1897. Office of the Geological survey.
- Paterson, M.S., 1990. Rock deformation experimentation. *Brittle-Ductile Transit. Rocks* 187–194. <https://doi.org/10.1029/gm056p0187>
- PATERSON, M.S., 1958. EXPERIMENTAL DEFORMATION AND FAULTING IN WOMBEYAN MARBLE. *Geol. Soc. Am. Bull.* 69, 465. [https://doi.org/10.1130/0016-7606\(1958\)69\[465:edafiw\]2.0.co;2](https://doi.org/10.1130/0016-7606(1958)69[465:edafiw]2.0.co;2)
- Peddinti, V., Chen, G., Manohar, V., Ko, T., Povey, D., Khudanpur, S., 2015. Jhu aspire system: Robust lvsr with tdnns, ivector adaptation and rnn-lms, in: 2015 IEEE Workshop on Automatic Speech Recognition and Understanding (ASRU). IEEE, pp. 539–546.
- Pickett, G.R., 1963. Acoustic character logs and their applications in formation evaluation. *J. Pet. Technol.* 15, 659–667.
- Pomponi, E., Vinogradov, A., 2013. A real-time approach to acoustic emission clustering. *Mech. Syst. Signal Process.* 40, 791–804.
- Portevin, A., Le Chatelier, F., 1923. Sur un phénomène observé lors de l’essai de traction d’alliages en cours de transformation. *Comptes Rendus Académie Sci. Paris* 176, 507–510.
- Pramoda Raj, 13:36:48 UTC. Stress and strain ellipsoid.
- Pyrak, L.J., 1988. Seismic visibility of fractures. California Univ., Berkeley, CA (USA).
- Pyrak-Nolte, L.J., Myer, L.R., Cook, N.G.W., 1990. Transmission of seismic waves across single natural fractures. *J. Geophys. Res.* 95, 8617. <https://doi.org/10.1029/jb095ib06p08617>
- Pyrak-Nolte, L.J., Nolte, D.D., 1992. Frequency dependence of fracture stiffness. *Geophys. Res. Lett.* 19, 325–328. <https://doi.org/10.1029/91gl03179>
- Ramírez-Rojas, A., Flores-Márquez, E., Sarlis, N., Varotsos, P., 2018. The complexity measures associated with the fluctuations of the entropy in natural time before the deadly México M8. 2 earthquake on 7 September 2017. *Entropy* 20, 477.

- Ramsey, J.M., Chester, F.M., 2004. Hybrid fracture and the transition from extension fracture to shear fracture. *Nature* 428, 63–66. <https://doi.org/10.1038/nature02333>
- Rao, Y., Wang, Y., 2009. Fracture effects in seismic attenuation images reconstructed by waveform tomography. *GEOPHYSICS* 74, R25–R34. <https://doi.org/10.1190/1.3129264>
- Reid, H.F., 1910. The mechanics of the earthquake. Calif. Earthq. April 18 1906 Rep. State Earthq. Investig. Comm.
- Renard, F., McBeck, J., Kandula, N., Cordonnier, B., Meakin, P., Ben-Zion, Y., 2019. Volumetric and shear processes in crystalline rock approaching faulting. *Proc. Natl. Acad. Sci.* 116, 16234–16239.
- Rice, J.R., 1972. Some remarks on elastic crack-tip stress fields. *Int. J. Solids Struct.* 8, 751–758.
- Ripperger, J., Mai, P.M., Ampuero, J.-P., 2008. Variability of Near-Field Ground Motion from Dynamic Earthquake Rupture Simulations. *Bull. Seismol. Soc. Am.* 98, 1207–1228. <https://doi.org/10.1785/0120070076>
- Ródenas, J., García, M., Alcaraz, R., Rieta, J., 2015. Wavelet entropy automatically detects episodes of atrial fibrillation from single-lead electrocardiograms. *Entropy* 17, 6179–6199.
- Ruesch, H., 1959. Physical problems in the testing of concrete. *Zem. Kalk-Gips* 12, 1–9.
- Sadri, A., Ying, W., 2019. Monitoring Blast Furnaces and Other Process Vessels by Acoustic Emission (AE) Monitoring Technique. Presented at the AISTech2019 Proceedings of the Iron and Steel Technology Conference, AIST. <https://doi.org/10.33313/377/039>
- Saito, T., 2002. Envelope broadening of spherically outgoing waves in three-dimensional random media having power law spectra. *J. Geophys. Res.* 107. <https://doi.org/10.1029/2001jb000264>
- Sato, H., 1989. Broadening of seismogram envelopes in the randomly inhomogeneous lithosphere based on the parabolic approximation: southeastern Honshu, Japan. *J. Geophys. Res.* 94, 17735. <https://doi.org/10.1029/jb094ib12p17735>
- Sato, H., Fehler, M.C., 1998. *Seismic Wave Propagation and Scattering in the Heterogeneous Earth*. Springer New York. <https://doi.org/10.1007/978-1-4612-2202-6>
- Schock, R.N., Heard, H.C., Stephens, D.R., 1973. Stress-strain behavior of a granodiorite and two graywackes on compression to 20 kilobars. *J. Geophys. Res.* 78, 5922–5941. <https://doi.org/10.1029/jb078i026p05922>
- Schoenberg, M., 1980. Elastic wave behavior across linear slip interfaces. *J. Acoust. Soc. Am.* 68, 1516–1521. <https://doi.org/10.1121/1.385077>
- Schofield, B.H., Barreiss, B., Kyrala, A., 1958. Acoustic emission under applied stress WADS. Technical Report 58-194, Lessells and Associates Inc., Boston, Mass.
- Scholey, J.J., Wilcox, P.D., Wisnom, M.R., Friswell, M.I., 2010. Quantitative experimental measurements of matrix cracking and delamination using acoustic emission. *Compos. Part Appl. Sci. Manuf.* 41, 612–623. <https://doi.org/10.1016/j.compositesa.2010.01.008>

- Scholz, C.H., 1968. The frequency-magnitude relation of microfracturing in rock and its relation to earthquakes. *Bull. Seismol. Soc. Am.* 58, 399–415.
- Scholz, C.H., Boitnott, G., Nemat-Nasser, S., 1986. The Bridgman Ring Paradox Revisited. *Frict. Faulting* 587–599. https://doi.org/10.1007/978-3-0348-6601-9_10
- Schubnel, A., Brunet, F., Hilairet, N., Gasc, J., Wang, Y., Green, H.W., 2013. Deep-focus earthquake analogs recorded at high pressure and temperature in the laboratory. *Science* 341, 1377–1380.
- Schubnel, A., Nishizawa, O., Masuda, K., Lei, X.J., Xue, Z., Guégen, Y., 2003. Velocity Measurements and Crack Density Determination During Wet Triaxial Experiments on Oshima and Toki Granites. *Pure Appl. Geophys.* 160, 869–887. <https://doi.org/10.1007/pl00012570>
- Scrubby, C.B., Wadley, H.N.G., 1983. An assessment of acoustic emission for nuclear pressure vessel monitoring. *Prog. Nucl. Energy* 11, 275–297. [https://doi.org/10.1016/0149-1970\(83\)90014-8](https://doi.org/10.1016/0149-1970(83)90014-8)
- Sharma, R., Pachori, R., Acharya, U., 2015. Application of entropy measures on intrinsic mode functions for the automated identification of focal electroencephalogram signals. *Entropy* 17, 669–691.
- Shih, P.-J.R., Frehner, M., 2016. Laboratory evidence for Krauklis-wave resonance in fractures and implications for seismic coda wave analysis. *Geophysics* 81, T285–T293.
- Shiotani, T., 2008. Parameter analysis, in: *Acoustic Emission Testing*. Springer, pp. 41–51.
- Shiotani, T., 1994. Evaluation of progressive failure using AE sources and improved b-value on slope model tests. *Prog. Acoust. Emiss. VII JSNDI* 529–534.
- Sibson, R.H., 1985. A note on fault reactivation. *J. Struct. Geol.* 7, 751–754.
- Siracusano, G., Lamonaca, F., Tomasello, R., Garescì, F., La Corte, A., Carnì, D.L., Carpentieri, M., Grimaldi, D., Finocchio, G., 2016. A framework for the damage evaluation of acoustic emission signals through Hilbert–Huang transform. *Mech. Syst. Signal Process.* 75, 109–122.
- Skempton, A.W., 1961. Horizontal stresses in an overconsolidated Eocene clay, in: *Proc. 5th Int. Conf. Soil Mech.* pp. 351–357.
- Snyder, D., Garcia-Romero, D., Povey, D., 2015. Time delay deep neural network-based universal background models for speaker recognition, in: *2015 IEEE Workshop on Automatic Speech Recognition and Understanding (ASRU)*. IEEE, pp. 92–97.
- Spanner, J.C., 1981. *Advances in acoustic emission*. Dunhart USA 1.
- Stanchits, S., Vinciguerra, S., Dresen, G., 2006. Ultrasonic Velocities, Acoustic Emission Characteristics and Crack Damage of Basalt and Granite. *Pure Appl. Geophys.* 163, 975–994. <https://doi.org/10.1007/s00024-006-0059-5>
- Takahashi, T., Sato, H., Nishimura, T., Obara, K., 2009. Tomographic inversion of the peak delay times to reveal random velocity fluctuations in the lithosphere: method and application to northeastern Japan. *Geophys. J. Int.* 178, 1437–1455. <https://doi.org/10.1111/j.1365-246x.2009.04227.x>
- Takahashi, T., Sato, H., Nishimura, T., Obara, K., 2007. Strong inhomogeneity beneath Quaternary volcanoes revealed from the peak delay analysis of S-wave seismograms

- of microearthquakes in northeastern Japan. *Geophys. J. Int.* 168, 90–99. <https://doi.org/10.1111/j.1365-246x.2006.03197.x>
- Takemura, S., Furumura, T., Maeda, T., 2015. Scattering of high-frequency seismic waves caused by irregular surface topography and small-scale velocity inhomogeneity. *Geophys. J. Int.* 201, 459–474. <https://doi.org/10.1093/gji/ggv038>
- Terzaghi, K., 1936. A fundamental fallacy in earth pressure computations. Harvard University.
- Tobias, A., 1976. Acoustic-emission source location in two dimensions by an array of three sensors. *Non-Destr. Test.* 9, 9–12. [https://doi.org/10.1016/0029-1021\(76\)90027-X](https://doi.org/10.1016/0029-1021(76)90027-X)
- Treeby, B.E., Cox, B.T., 2010. k-Wave: MATLAB toolbox for the simulation and reconstruction of photoacoustic wave fields. *J. Biomed. Opt.* 15, 021314. <https://doi.org/10.1117/1.3360308>
- Tripathi, J.N., Sato, H., Yamamoto, M., 2010. Envelope broadening characteristics of crustal earthquakes in northeastern Honshu, Japan. *Geophys. J. Int.* 182, 988–1000. <https://doi.org/10.1111/j.1365-246x.2010.04657.x>
- Tullis, T.E., Tullis, J., 1986. Experimental rock deformation techniques. *Miner. Rock Deform. Lab. Stud.* 297–324. <https://doi.org/10.1029/gm036p0297>
- Ulusay, R., 2014. The ISRM suggested methods for rock characterization, testing and monitoring: 2007-2014. Springer.
- Unakafova, V., Keller, K., 2013. Efficiently measuring complexity on the basis of real-world data. *Entropy* 15, 4392–4415.
- van der Baan, M., Eaton, D.W., Preisig, G., 2016. Stick-split mechanism for anthropogenic fluid-induced tensile rock failure. *Geology* 44, 503–506. <https://doi.org/10.1130/G37826.1>
- Vavryčuk, V., 2005. Focal mechanisms in anisotropic media. *Geophys. J. Int.* 161, 334–346.
- Vavryčuk, V., 2002. Non-double-couple earthquakes of 1997 January in West Bohemia, Czech Republic: evidence of tensile faulting. *Geophys. J. Int.* 149, 364–373.
- Vavryčuk, V., 2001. Inversion for parameters of tensile earthquakes. *J. Geophys. Res. Solid Earth* 106, 16339–16355.
- Vlastos, S., Liu, E., Main, I.G., Narteau, C., 2007. Numerical simulation of wave propagation in 2-D fractured media: scattering attenuation at different stages of the growth of a fracture population. *Geophys. J. Int.* 171, 865–880. <https://doi.org/10.1111/j.1365-246x.2007.03582.x>
- Von Kármán, T., 1911. Über den Mechanismus des Widerstandes, den ein bewegter Körper in einer Flüssigkeit erfährt. *Nachrichten Von Ges. Wiss. Zu Gött. Math.-Phys. Kl.* 1911, 509–517.
- Walsh, J.B., Brace, W.F., 1966. Cracks and pores in rocks, in: 1st ISRM Congress. International Society for Rock Mechanics and Rock Engineering.
- Wong, T., 1982. Shear fracture energy of Westerly granite from post-failure behavior. *J. Geophys. Res. Solid Earth* 87, 990–1000. <https://doi.org/10.1029/jb087ib02p00990>
- Wong, T.-F., 1982. Micromechanics of faulting in Westerly granite, in: International Journal of Rock Mechanics and Mining Sciences & Geomechanics Abstracts. Elsevier, pp. 49–64.

- Yang, Z., Yu, Z., Xie, C., Huang, Y., 2014. Application of Hilbert–Huang Transform to acoustic emission signal for burn feature extraction in surface grinding process. *Measurement* 47, 14–21.
- Zang, A., Wagner, C.F., Dresen, G., 1996. Acoustic emission, microstructure, and damage model of dry and wet sandstone stressed to failure. *J. Geophys. Res. Solid Earth* 101, 17507–17521.
- Zhang, J., 2018. Investigation of Relation between Fracture Scale and Acoustic Emission Time-Frequency Parameters in Rocks [WWW Document]. *Shock Vib.* <https://doi.org/10.1155/2018/3057628>
- Zhu, T., Carcione, J.M., 2014. Theory and modelling of constant-Q P-and S-waves using fractional spatial derivatives. *Geophys. J. Int.* 196, 1787–1795.
- Zhu, W., Wong, T., 1997. The transition from brittle faulting to cataclastic flow: Permeability evolution. *J. Geophys. Res. Solid Earth* 102, 3027–3041.
- Zieger, T., Sens-Schönfelder, C., Ritter, J.R.R., Lühr, B.-G., Dahm, T., 2016. P-wave scattering and the distribution of heterogeneity around Etna volcano. *Ann. Geophys.* 59, 0432. <https://doi.org/10.4401/ag-7085>
- Zoukaneri, I., Porsani, M.J., 2015. A combined Wigner-Ville and maximum entropy method for high-resolution time-frequency analysis of seismic data. *Geophysics* 80, O1–O11.